A Micron-Scale Laser-Based Beam Profile Monitor for the International Linear Collider

Lawrence Charles Deacon

Department of Physics

Royal Holloway, University of London

A thesis submitted to the University of London for the

Degree of Doctor of Philosophy

April 14, 2009

DECLARATION

I confirm that the work presented in this thesis is my own. Where information has been derived from other sources, I confirm that this has been indicated in the document.

Lawrence Charles Deacon

Abstract

A micron-scale laser-wire system was constructed and tested at the Accelerator Test Facility (ATF) extraction line at the High Energy Accelerator Research Organisation (KEK) in Japan. The system was evaluated through collision tests, electron beam tests, laser beam measurements and simulations. Beam halo measurements were carried out in order to compare the beam halo to a theory of its production through gas scattering and towards evaluating it as a source of background for diagnostic instruments at ATF2 and the International Linear Collider (ILC). Simulations were carried out to test the signal extraction of the system at the future ATF2 and of a similar system in the proposed ILC beam delivery system, with implications for sharing the signal extraction region with the polarimeter.

There are many people I wish to express my gratitude to, and I would like to acknowledge them here.

First and foremost I thank Grahame Blair for his supervision, direction, inspiration, insight and advise.

I thank Stewart Boogert for being an excellent mentor and for his constant dedication and enthusiasm, both to the laser-wire project and to the invaluable training he gave me.

I would like to thank those people with whom I worked on the laser-wire: Pavel Karataev, David Howell, Alexander Aryshev, Laura Corner, Nicolas Delerue, Myriam Newman, Alessio Bosco, Gary Boorman and Laurence Nevay.

Finally, I would like to thank Junji Urakawa, Nobuhiro Terunuma and everyone at ATF, John Carter, Ilya Agapov, Steve Malton, Marc Ross, Michael Price, Simon George, Diego Bellini, Laura Corner, James Nichols, Mike Green, Pedro Teixeira-Dias, Ken Peach, Glen Cowan, Tegid Jones, Rantej Kler, Ruby Sehra, Deborah Bowden, Roy Mohanan, Lixiu Lin, Maximilian Micheler, Christina Potter, Sudan Paramesvaran, Claire Quarman, Michele Gianelli, Adam Wren, Paul Jackson, Daniel Hayden, John Saunders, Brian Cowan, my parents and all my friends, family and colleagues for their help and support during my PhD work.

Contents

1 Thesis Overview **17**

1.1 Chapter 2 - Theory . . . 17

1.2 Chapter 3 - ATF Extraction Line Laser-Wire . . . 18

1.3 Chapter 4 - Upgraded Laser-Wire System . . . 18

1.4 Chapter 5 - Halo Measurement . . . 18

1.5 Chapter 6 - Simulations for the ATF and ILC Laser-Wires . . . 18

1.6 What I did . . . 19

2 Theory **21**

2.1 Beam Dynamics and Emittance Measurement . . . 21

2.1.1 Reference Trajectory . . . 21

2.1.2 Magnetic Rigidity . . . 22

2.1.3 Focusing . . . 22

2.1.4 Hill's Equation . . . 23

2.1.5 Liouville's Theorem . . . 25

2.1.6 Matrix description . . . 26

2.1.7 Twiss Parameters and the Beam Envelope . . . 27

2.1.8 Transformation of the Phase Ellipse . . . 29

2.1.9 Emittance Measurement . . . 29

2.2 Dispersion . . . 33

2.3 Compton Scattering . . . 35

2.3.1 Wave Optics and Gaussian Beams . . . 36

2.3.2 Sources of M^2 . . . 41

2.3.3 Laser-wire Compton Rates and Laser Propagation 41
2.3.4 Simulation of Compton Scattering 43
2.4 Optical Diffraction Radiation 45
2.5 Synchrotron Radiation 46
2.5.1 Synchrotron Radiation Power 46
2.5.2 Synchrotron Radiation Spectrum 47

3 ATF Extraction Line Laser-Wire 48
3.1 The Accelerator Test Facility 48
3.2 Setup 51
3.2.1 Extraction Line Optics 51
3.2.2 ATF Beam Position Monitors 55
3.3 Laser-Wire System 56
3.3.1 Principle of Operation 57
3.3.2 Laser System 59
3.3.3 Layout of Optical Components 62
3.3.4 Detectors 62
3.3.5 Monitoring of Laser Power Output 66
3.3.6 Temperature Control and Monitoring 67
3.3.7 Beam Position and Focus Control 67
3.3.8 Scanning Geometry 69
3.3.9 Knife Edge and Vacuum Manipulator 71
3.3.10 Data Acquisition System 72
3.4 Simulation of laser-wire Signal 73
3.5 Collision Measurements 73
3.5.1 Laser Scan 73
3.5.2 Waist Scan 73
3.5.3 Quad Scan 74
3.5.4 Results and Analysis 74

4 Upgraded Laser-Wire System 79
4.1 ATF Extraction Line Laser-Wire Custom f/2 lens 79

4.1.1 Lens Description . . . 79
4.1.2 Chamber Mover System . . . 81
4.1.3 Dual mirror scanning system . . . 82
4.2 Types of Measurements Performed on Custom Lens System . . . 82
4.3 Laser Beam and Lens Measurements and Simulations . . . 82
4.3.1 Simulation of Lens M^2 . . . 82
4.3.2 Profiling of Laser System . . . 84
4.3.3 Ellipticity . . . 89
4.3.4 Effect of General Astigmatism on the Principle Beam Radii, w_u and w_v 90
4.3.5 Laser Beam Position Stability . . . 91
4.3.6 Input Laser Beam Size . . . 92
4.3.7 IP Profile Measurements . . . 92
4.3.8 Optical Simulation of Laser-Wire System . . . 93
4.3.9 Photo-diode Laser Power Meter Installation . . . 97
4.4 Electron Beam Measurements . . . 98
4.4.1 Beam Tests of Knife Edge for the f/2 Lens System . . . 98
4.4.2 BPM Calibration . . . 102
4.4.3 Dispersion Measurement . . . 102
4.5 Collision Measurements . . . 106
4.5.1 Smallest σ_c Laser Scan . . . 108
4.5.2 Profiling the Laser Beam Using the Electron Beam . . . 111
4.5.3 Vertical Scans Statistics Study . . . 112
4.5.4 Single Quad Scan . . . 112
4.5.5 Emittance Measurement Using Wire Scanner . . . 113
4.5.6 Skew Quad Scan . . . 117
4.5.7 Emittance Measurement Using Laser-Wire . . . 120
4.6 Conclusions . . . 124

5 Halo Measurement **129**

5.1 Linearity of Hamamatsu R877 Photomultiplier Tube . . . 130
5.1.1 Linearity Tests . . . 130
5.2 Halo Measurement . . . 132

5.2.1 Comparison with a Theory of Non Gaussian Beam Distributions Due to Gas Scattering . . . 134
5.2.2 Data Analysis . . . 135
5.3 Conclusions . . . 137

6 Simulations for the ATF and ILC Laser-Wires 138
6.1 BDSIM . . . 138
6.2 Simulation of ATF Laser-Wire Using BDSIM . . . 139
6.2.1 Signal Extraction at ATF . . . 139
6.2.2 ATF Detector Conversion Efficiency . . . 141
6.2.3 Signal Extraction at ATF2 . . . 141
6.3 Simulations for ILC BDS laser-wires . . . 144
6.4 Initial Beam Conditions . . . 145
6.4.1 Detecting Laser-Wire Photons . . . 146
6.5 Detecting Laser-Wire Compton Scattered Electrons . . . 148
6.6 Laser-Wire Background in Polarimeter Detector . . . 149
6.7 Dealing With SR Backgrounds . . . 151
6.7.1 Laser-Wire γ_C Detection . . . 151
6.7.2 Simulation . . . 153
6.8 Linac-related Backgrounds . . . 156
6.9 Conclusions . . . 157

7 Conclusions 159
7.1 Future Work . . . 159
7.2 Summary and Main Conclusions . . . 160

List of Figures

2.1 A diagram showing the relationship between the shape and orientation of the phase ellipse and the Twiss parameters. 28

2.2 The transformation of a phase ellipse in drift space. 28

2.3 Feynman diagrams for Compton scattering. Time goes from left to right. Left diagram: s channel. Right diagram: t channel. 36

3.1 ATF. Bunches start at the gun (bottom, "E-GUN"), are accelerated by the linear accelerator (right) before going into the damping ring, which is the racetrack structure in the middle. After being damped they go into the extraction line (left) where the laser-wire is located. The location is shown more precisely in Fig. 3.2. 49

3.2 Location of the laser-wire and detector in the ATF extraction line. 50

3.3 MAD simulation output showing the square root of the beta functions and the horizontal dispersion function with laser-wire optics. $k_{QD4X} = -1.516659$ m^{-1}, $k_{QF4X} = 1.574676$ m^{-1}. 52

3.4 MAD simulation output showing the horizontal and vertical beam sizes along the extraction line. $k_{QD4X} = -1.516659$ m^{-1}, $k_{QF4X} = 1.574676$ m^{-1}. 53

3.5 MAD simulation output showing the horizontal and vertical beam sizes around the laser-wire interaction point. This is a blow up of Fig. 3.4 around the laser-wire IP, which is 20.990 m along the extraction line. $k_{QD4X} = -1.516659$ m^{-1}, $k_{QF4X} = 1.574676$ m^{-1}. 54

3.6 A schematic diagram of the laser-wire system. 57

3.7 A diagram of the overlap of the laser and electron beams. On the left, the electron beam is shown travelling into the page and the laser beam travels from left to right. σ_y here is the vertical electron beam size. Δy is the displacement in y from the maximum overlap position. The dotted lines are the edges of a Gaussian laser beam converging to a waist of size σ_0 and with Rayleigh range z_r (Eq. 2.86). 58
3.8 A picture of the laser-wire interaction chamber with scanner and final focus lens. The axes are defined with the direction of travel of the incoming laser as x, the direction of travel of the electron beam is z and the vertical as y. 60
3.9 Laser beam path from the laser upstairs *(top)* to the alignment table *(bottom)*. . 63
3.10 Pre-IP optical bread board. 64
3.11 Post-IP optical bread board. 64
3.12 ATF laser-wire detectors. The vertical structure in the foreground is the Cerenkov detector periscope. Its photomultiplier tube is out of shot at the bottom of the periscope, completely surrounded by lead shielding. In the background, the front face of the lead glass calorimeter can be seen, with shielding around the sides. The calorimeter and shielding are placed on top of a metal support structure. . 65
3.13 Graphical user interface of the laser-wire DAQ 68
3.14 Geometry of the final scanning mirror. n_1 and n_2 are the incident and reflected laser beam vectors respectively. n_2 is incident upon the final focusing lens. The s vector is the normal to the mirror plane. The rotation angles θ and ϕ are shown. θ is the angle changed for vertical scanning and ϕ is set to $\pi/4$. 69
3.15 *Left:* knife edge (bottom of image) and vacuum manipulator. *Right:* vacuum chamber with knife edge and manipulator installed at the top. The picture foreground shows the post IP optics bread board with the f=100 mm re-collimating lens and the avalanche photo-diode. 72
3.16 A 6 μm size vertical (y) scan fitted to a Gaussian. Each point is the average of 5 pulses. The signal is normalised to the electron beam current which was measured using a wall current monitor. The fit, red dashed line, is a constant + Gaussian. 75
3.17 Convolution of laser and electron beam vs. final focus lens position 75

3.18 Laser and electron bunch relative peak signal vs. phase. 76
3.19 Same data as in Fig. 3.16 but measured using the calorimeter 76
3.20 Cerenkov and calorimeter signals vs. beam charge. The intercept is far from zero due to pedestal in the wall current monitor. 77
3.21 Convolution of laser and electron beam size vs. quadrupole current 78

4.1 Photograph of the custom lens. 79
4.2 Diagram of the custom lens. The blue lines are rays traced through the system. 80
4.3 New chamber with movers 81
4.4 Results of Zemax simulation of the M^2 after propagating through the custom lens of a laser beam with input $M^2 = 1$ for different input beam sizes. The resulting M^2 is called *lens* M^2 in the text. 83
4.5 Results of Zemax simulation of the W_0 of the custom lens for different input beam sizes. "POP" stands for "physical optics propagation". Experimental data are also shown. The input laser has $M^2 = 1$. 83
4.6 Photograph of the "downstairs" optical table. The spacing between the holes is 1.25 cm. 85
4.7 A profile measurement using a continuous wave (CW) laser with the layout the same as for the measurements taken during the shift. Red = u-axis, blue = v-axis. 86
4.8 A profile measurement using a continuous wave (CW) laser. In this case, no splitter was used. 87
4.9 An image of the CW laser profile with the camera stage at -50 mm. The vertical axis is intensity. 87
4.10 An image of the pulsed laser profile with the camera stage at -50 mm. Vertical axis is intensity. 88
4.11 A profile measurement of the pulsed laser. In this case, no splitter was used. . . 88
4.12 Ellipticity of the pulsed laser as a function of propagation distance z. 89
4.13 Orientation of the pulsed laser as a function of propagation distance z. 90
4.14 A knife edge image taken using the BeamMapC near the focus using the CW laser. 93
4.15 An IP profile measurement in the vertical axis of the CW laser after the custom final focus lens. 94

4.16 An IP profile measurement in the vertical axis of the CW laser after the custom final focus lens. The M^2 fit parameter is fixed at 2.3. 94
4.17 A vertical knife edge scan with the target perpendicular to the electron beam at 0 μm horizontal chamber position. 99
4.18 A vertical knife edge ODR/OTR scan using an APD as a detector with the knife edge 45° to the electron beam. 100
4.19 A knife edge angular ODR/OTR scan using an APD as a detector with the z-shift at 9250 μm (full signal). Here, 0° means 45° to the electron beam. 101
4.20 *Left:* CW laser light at exit window with knife edge before the focus in z. The top part of the beam is obscured. *Centre:* CW laser light at exit window with knife edge at the focus in z. The laser beam is small enough to pass under the knife edge. *Right:* CW laser light at exit window with knife edge after the focus in z. The bottom part of the beam is obscured. 101
4.21 ATF extraction line measured and simulated dispersion. The upstream quadrupole focusing strengths where $k_{QD4X} = -1.516659$ [1/m], $k_{QF4X} = 1.574676$ [1/m], and $s = 0$ corresponds to the beginning of the extraction line. The error bars are too small to be visible. 103
4.22 ATF extraction line measured dispersion function $D_x(s)$, where $s = 0$ corresponds to the beginning of the extraction line. The vertical dashed line indicates the location of the LWIP. The error bars are too small to be visible. 104
4.23 ATF extraction line measured dispersion function $D_y(s)$, where $s = 0$ corresponds to the beginning of the extraction line. The vertical dashed line indicates the location of the LWIP. The error bars are too small to be visible. 104
4.24 ATF extraction line measured dispersion function $D_y(s)$, where $s = 0$ corresponds to the beginning of the extraction line. The vertical dashed line indicates the location of the LWIP. 105
4.25 ATF extraction line measured dispersion, $D_y(s)$ with $I_{QS1X} = -5$ A, where $s = 0$ corresponds to the beginning of the extraction line. The vertical dashed line indicates the location of the LWIP. The error bars are too small to be seen. . . 107

4.26 ATF extraction line measured dispersion, $D_x(s)$ with $I_{QS1X} = -5$ A, where $s = 0$ corresponds to the beginning of the extraction line. The vertical dashed line indicates the LWIP. The error bars are too small to be seen. 107
4.27 The smallest σ_c laser scan measured using the laser wire system. Gaussian + constant fit function is shown. The scan was performed on 29th May 2008 after skew quadrupole tuning. 109
4.28 The smallest σ_c laser scan measured using the laser wire system. Overlap integral fit function is shown. The scan was performed on 29th May 2008 after tuning the skew quadrupoles. 110
4.29 Waist scan. 29/05/2008. The laser focus position is x in electron beam coordinates. The fit function is the laser propagation function, Eq. 2.86. 111
4.30 A single shot scan near the laser focus at the default quad settings 112
4.31 A 10 shot scan near the laser focus at the default quad settings 113
4.32 QD4X quad scan. QF4X current was kept constant at 73.58 A. The black dots are data. The red lines are Gaussian + constant fits. 114
4.33 QD4X quad scan. QF4X current was kept constant at 73.58 A. 115
4.34 Emittance measurement with skew quadrupoles off. 116
4.35 Emittance measurement with skew quadrupoles on. 117
4.36 QS1X skew quad scan 23/05/08, part 1. QD4X set to 74.06 A. The black dots are data. The red lines are Gaussian + constant fits. 118
4.37 QS1X skew quad scan 23/05/08, part 2. QD4X set to 74.06 A. The black dots are data. The red lines are Gaussian + constant fits. 119
4.38 QS1X skew quad scan 23/05/08. QD4X set to 74.06 A. 120
4.39 QS2X skew quad scan 23/05/08. QD4X set to 74.06 A. The black dots are data. The red lines are Gaussian + constant fits. 121
4.40 QS2X skew quad scan 23/05/08. QD4X set to 74.06 A. Markers as Fig. 4.33 . . 122
4.41 QS1X skew quad scan 29/05/08. QD4X set to 74.06 A. The black dots are data. The red lines are Gaussian + constant fits. 123
4.42 QS1X skew quad scan 29/05/08. QD4X set to 74.06 A. The reason for the outlier at -2 A is unknown. 124

4.43 29/05/08: QD4X scan. The black dots are data. The red lines are Gaussian + constant fits. 125
4.44 29/05/08: QD4X/QF4X laser-wire scan with emittance fit. Plotted is the QD4X k value versus σ_e^2. The fit function is Eq. 4.18, with S_{11} and S_{12} as Eqs. 4.20 and 4.21. 126
4.45 QD4X k value versus σ_e^2, as measured by the laser-wire. The fit function is Eq. 4.19 126

5.1 Gated signal of LED in scope trace. Amplitude = 300 mV, FWHM = 40 ns and area = -19.4538 nsV. 131
5.2 LED output vs. PMT output. $\chi^2/\mathrm{NDF} = 38.3/5 = 7.66$ for the straight line fit. 132
5.3 Measured beam distribution with fits to a Gaussian, Eq. 5.2 (halo fit) and Eq. 5.3. (approximate halo fit) 133
5.4 The Gaussian fit in Fig. 5.3 133
5.5 Fig. 5.3 plotted without the logarithmic scale. 133

6.1 A picture of quadrupole QD6 showing the pole tips and the laser-wire signal. . 139
6.2 A quadrupole geometry 139
6.3 Electron and positron angles from normal to the detector surface after photon scattering in the lead converter. 140
6.4 Electron and positron positions after γ conversions in the lead converter. 140
6.5 Electron and positron energies after lead converter. 141
6.6 A screen shot from BDSIM with quadrupoles in red, a dipole in blue and sextupoles in white. The green line is the trajectory of a photon. 142
6.7 Simulation of the ATF2 extraction line using BDSIM. 143
6.8 The first kilometre of the BDS layout showing functional subsystems, starting from the linac exit; X - horizontal position of elements, Z - distance measured from the e^+/e^- interaction point. 146
6.9 BDSIM screen shot of the first $\sim$600 m of the BDS layout, showing the locations of the fourth (final) laser-wire interaction point, the beginning of the polarimeter chicane a laser-wire γ_C converter and detector and the polarimeter detector. . . 146

6.10 Visualisation of a laser-wire event. The Compton scattered photon (green) and electron (red) enter the image from the right (viewpoint reversed w.r.t. Figs. 6.8 and 6.9). The photon hits a lead converter and an electron and a positron (blue) appear by pair production. Further downstream, showering occurs in the vacuum chamber walls, beam pipe and magnets. 147

6.11 Shape of the energy spectrum with a 250 GeV e^- beam (the vertical axis is arbitrary). Left: e_C^-. Right: γ_C. 148

6.12 Statistical fluctuations in γ_C conversion vs. lead thickness. The error bars are larger where fewer data were collected. 148

6.13 Positions with respect to the e^- beam reference trajectory of the ILC laser-wire e_C^- at proposed laser-wire electron detector for a 250 GeV e^- beam. The vertical dotted line shows the innermost edge of the detector. 149

6.14 Shape of the distribution of γ_{SR} along the horizontal axis at the entrance to the second set of dipoles. $E_c = 4.1$MeV. 152

6.15 Left: shape of the distribution of laser-wire photons along the horizontal axis at the entrance to the second set of dipoles. x=0 is the neutral beam centre. Right: shape of the energy spectrum downstream of the converter of pair produced electrons and positrons from γ_{SR} from a 250 GeV e^- beam. $E_c = 4.1$MeV. . . 152

6.16 Trajectory of a negatively charged particle in a dipole field. ρ is the radius of curvature, B is the magnetic field and d is the detector transverse size. 153

6.17 Shape of the energy spectrum of the generated SR for $k = 4.5$. k is defined in Tab. 6.8. 154

6.18 Shape of the energy spectrum downstream of the 3.5 mm converter of pair-produced electrons and positrons from γ_C from a 250 GeV e^- beam. 155

List of Tables

3.1 Integrated magnet focusing strength k settings for normal ATF and laser wire optics. The quadrupoles can be seen in Figs. 3.1 (extraction line) and 3.2. . . . 51

3.2 Input parameters for the MAD simulation. 51

3.3 Beam parameters for different settings of the two quadrupoles upstream of the laser-wire interaction point according to the MAD simulation. The second table is a continuation of the first. In the upper half of each table, two quadrupoles are changed and in the lower half of each table, only one quadrupole is changed. The quadrupole settings are the same values used in the quad scans in Sec. 4.5. The emittance settings are as follows: $\varepsilon_x = 2$ nm and $\varepsilon_y = 20$ pm. 55

3.4 Types of BPM installed. 56

3.5 Fit parameters from the fit of Eq. 3.17 to the Cerenkov and Calorimeter data in Figs. 3.16 and 3.19. A and k have the same (arbitrary) units. 74

3.6 Detector linearity fit for calorimeter and aerogel Cerenkov detectors. 77

4.1 Custom laser-wire lens design parameters. Surface types are Even Asphere (A) and Standard (S). "d" is the distance from the previous surface. "Radius" is the radius of curvature of the surface. Semi-diameter is the semi-diameter of the aperture. 80

4.2 Custom laser-wire lens design parameters. k is the conic constant and the α_i are the higher order terms in Eq. 4.1 80

4.3 Results of fit of Eq. 4.2 to the lens simulation data, Fig. 4.4 84

4.4 M^2 measurements on the CW and pulsed lasers (Figs. 4.8 4.11 and 4.7). The errors are statistical errors. 87

4.5 Results of the orientation fit. The fit function is Eq. 4.5 and the data points and fit function are plotted in Fig. 4.13. 91
4.6 Input laser beam sizes (W_{in}), ellipticities, (η_{in}), and rotation angles (ϕ_{in}). 92
4.7 Input/output parameters to the laser propagation model and measured values.. Mod. means the value is either an input to or an output from the model. Meas. means measured value. Coll. meas. means collision measurement, see Sec. 4.5 98
4.8 Beam line elements between QD4X and LWIP. 100
4.9 29/05/08. Calibration equations for BPM 1 (downstream) and BPM 2 (upstream) in x (horizontal) and y (vertical) axes. 102
4.10 Straight line ($p_0 + p_1 s$) dispersion fits between the LWBPMs. 105
4.11 σ_C calculated from Fig. 4.27 using Gaussian + constant and Gaussian + line fits and 4σ second moment calculation. 109
4.12 Limits applied to the input parameters of the overlap integral fit. x_0 is the mean position in the distribution. W_{in} is the input beam size ($W = 2\sigma$). f is the focal length of the lens. σ_{sm} is the calculated second moment. Δx is the displacement of the electron beam along the laser propagation axis. 111
4.13 Results of laser propagation fits to Fig. 4.29. 112
4.14 A summary of emittance measurements performed using the custom lens system. σ_C was calculated using Gaussian + constant fits. Vertical electron beam size due to dispersion, $\sigma_D = 3.03 \pm 0.66$ μm and $\sigma_{\text{lw}} = 2.1 \pm 0.2$ μm are subtracted in quadrature from the σ_cs in the analysis. The error in ε is the statistical error and does not take into account systematic error in the dispersion measurement and measurement of σ_{lw}. Also shown is the estimated minimum beam size, and the minimum beam size measured by the laser-wire, again with σ_{lw} and σ_D subtracted in quadrature. Note that the dispersion was only measured on 29/05/2008. There is likely to be variation in dispersion between shifts due to the fact that the beam orbit in the extraction line has to be retuned each time. Therefore, the only reliable emittance measurement quoted here is from 29/05/2008. The full systematic error for this measurement is included. The quoted σ_e [μm] (lw) on the 29/05/2008 is after skew quadrupole tuning, with the estimated σ_{lw} (2.1 ± 0.2 μm) subtracted in quadrature. 127

5.1 Quantities for ATF damping ring needed to calculate N_d and Θ. 135
5.2 Calculated values for beam-gas scattering. 135
5.3 Results of Gaussian fit to the electron beam core (Fig. 5.3) 136
5.4 The result of the fit of Eq. 5.2 to the data, Fig. 5.3 137

6.1 The effect of the IPBPM location on transmitted laser-wire signal. The N are the number of particles per bunch and the E are the sum of the particle energies per bunch. 144
6.2 Electron beam parameters at LWIP 4. 146
6.3 Simulated laser-wire γ_C parameters at various locations (see Fig. 6.8). s is the distance from LWIP 4. σ and σ' are the RMS position and RMS angle from the reference trajectory. σ_x and σ_y are each dominated by the $\sim 1/\gamma$ angular distribution of the Compton process, which explains why they have the same numerical values. 147
6.4 Bunch by bunch statistical uncertainty of photon detection. $\bar{N}$ is the number of electron positron *pairs* above the Cerenkov threshold (9 MeV) detected after conversion as a fraction of the original 1000 photons and ΔN is the corresponding bunch by bunch statistical fluctuation. Ten bunches were simulated; $\bar{N}$ average number and ΔN is the RMS. 149
6.5 Bunch by bunch statistical uncertainty of e_C^- detection. $\bar{N}$ is the mean number of e_C^- detected out of the 1000 initial Compton events and ΔN is the corresponding bunch by bunch statistical fluctuation. Clearance is the distance from the edge of the detector to the main 250 GeV beam line. The $\pm$ are the statistical uncertainties of the simulation. 150
6.6 Hits from the laser-wire and polarimeter in the polarimeter detector as a fraction of Compton events for both laser-wire and polarimeter with no MPS collimator in the chicane. "Hits" are defined as electrons or positrons with energy greater than 9.25 MeV entering the detector plane. "H" means hits and the subscript denotes the origin of the hits. $e_{C,pol}^-$ means Compton scattered electrons from the polarimeter. 150

6.7 Hits from laser-wire in the polarimeter detector as a fraction of laser-wire Compton events with the MPS collimator present in the chicane. See Tab. 6.6 for definitions. 150

6.8 Fraction of photons above a certain photon energy. The photon energy cut is given in units (k) of the critical energy, E_c [1]. 153

6.9 Simulation results for hits due to SR in γ_C detector. H_d is the number of detector hits due to SR with the Cerenkov detector placed just after the next dipole, where "hits" is defined as the number of electrons and positrons above the Cerenkov threshold energy (9.25 MeV) hitting the detector plane. σ_{H_d} is the statistical uncertainty in the simulation. 156

Chapter 1

Thesis Overview

The topic of this thesis is research and development towards a laser wire capable of measuring 1 μm beam sizes for the International Linear Collider (ILC). Part of the work involves developing and testing such a system at the Accelerator Test Facility (ATF) extraction line at the High Energy Accelerator Research Organisation (KEK) in Japan, where beam halo studies were carried in order to further an understanding of the background in the laser-wire detector. Also, simulations were carried out for the laser-wires in the ATF2 [2, 3] extraction line and the ILC beam delivery system.

1.1 Chapter 2 - Theory

Laser and accelerator physics relevant to the experimental and simulation work that was carried out are explained. Hill's equation and its solution are presented, leading on to a definition of *emittance*. Through Liouville's theorem, it is shown that emittance is a conserved quantity. The matrix description of the solutions to Hill's equation is introduced, leading to definition of the *Twiss parameters*. This matrix description is then used to explain how emittance measurements are carried out.

Compton scattering is explained. Laser propagation theory is explained along with the rate of Compton scattering, and its application to the measurement of the electron beam sizes using a laser-wire.

Synchrotron radiation (SR) power and spectrum equations are presented.

1.2 Chapter 3 - ATF Extraction Line Laser-Wire

ATF and the initial (commercial lens) ATF extraction line laser wire set-up are described and the principle of operation of the laser wire system is explained. The data acquisition system is described. The position of the laser beam as a function of mirror tilt is formulated. A simulation of the extraction line laser-wire and its results are presented. The process of searching for collisions between the laser and electron beam is described. The various collision measurements are described and collision data are presented.

1.3 Chapter 4 - Upgraded Laser-Wire System

An upgrade of the system with the installation of chamber movers, a multi-axis knife edge manipulator and a custom lens are presented. Laser system profiling methods and results are presented. Emittance and dispersion measurements are presented along with collision data, and conclusions are drawn.

1.4 Chapter 5 - Halo Measurement

The phenomenon of halo is introduced as a possible source of background for beam diagnostic systems. Tests of the detector linearity are described and results are presented. A method of measuring beam halo is described and experimental results are presented and compared to a theory of halo generation due to beam-gas scattering.

1.5 Chapter 6 - Simulations for the ATF and ILC Laser-Wires

A beam line simulation toolkit, BDSIM, is described along with changes made to the source code during the course of creating simulations of the ATF extraction line and the International Linear Collider (ILC). Simulations of the laser-wire signal extraction at ATF2 [2, 3] are described and the results are presented. A simulation of the ILC beam delivery system laser-wire is presented, along with results for signal and background levels for the laser-wire and polarimeter detectors due to the laser-wire and SR. Calculations of linac-related backgrounds are presented. Conclusions are drawn regarding the location of the laser-wire in the ILC beam delivery system.

1.6 What I did

Special ATF optics were developed by Pavel Karataev to produce a 1 μm electron beam spot size in the extraction line. I simulated these optics using MAD, with different upstream quadrupole settings that were used in our quad scans. I also plotted the dispersion function along the extraction line.

I put a lead-glass calorimeter behind the Cerenkov detector to compare the two types of detector.

I wrote much of the data acquisition and control software, for the following components in particular:

- The mirror mover actuators.
- The chamber mover system.
- The knife edge actuators.
- The temperature monitoring system.
- The laser power meter.
- The wire scanner stage.
- The DAQ graphical user interface.
- Implementation of automatic scanning.

I calculated the critical energy of the Cerenkov detector and simulated the laser-wire Compton photon pair production in the lead converter in the front of the detector.

I helped calculate the change in position of the laser as a function of mirror tilt.

I ran mechanical tests on the chamber mover system.

I was involved in most of the data taking. This included coming up with a shift plan and honing a strategy for collision search. I was responsible for getting the control system up and running, and testing and bug fixing before and during the shift. I assisted in the laser alignment procedures. I tuned the electron beam orbit in the ATF extraction line to reduce the background in the detector at the start of the shifts.

During shifts I operated the laser-wire and performed basic data analysis as we went along. I fixed any technical faults as they appeared. I often reported on the shifts at ATF meetings.

I carried out the analysis of the initial collision data, before the upgrade to the custom final focus lens. I also carried out the analysis of the custom lens system collision data, analysed the beam position monitor (BPM) data to measure the dispersion along the extraction line, the emittance measurement using the laser-wire, laser profile M^2 data, general astigmatism measurement, interaction point profile data, and input beam size data. I used these data in a computer model of the laser propagation of the system, which was built using an existing object oriented framework, in order to estimate the final focus laser beam size. I performed cross checks using continuous wave (CW) laser data. The final data for the laser measurements was collected by colleagues, but I performed preliminary measurements.

I fit the quad scan data to measure the emittance using the laser-wire. I compared these results to a wire scanner emittance measurement performed a month previously.

I fit the laser waist scan data and compared it to the laser propagation predicted by the laser propagation data and simulation.

From the results of all these studies I identified a programme of future work towards achieving a 1 μm electron beam size measurement.

I devised and carried out an experiment for measuring beam halo in the ATF extraction line and compared the results to a theory of halo production due to beam-gas scattering.

I simulated the ATF2 laser-wire system including all beam line components to determine the best signal extraction location and detector type. The simulations showed that relocation of a BPM was required in order to improve the extracted signal.

I simulated the ILC beam delivery system polarimeter chicane using BDSIM, a beam line simulation tool kit. This included a detailed representation of the polarimeter chicane, including the proposed machine protection system collimator. I simulated the synchrotron radiation into the laser-wire detector and showed that this background would swamp the signal. I then demonstrated that the existing dipole could be used as a high pass filter to remove this background. I also showed that the laser-wire Compton scattering events would produce an unacceptable background in the polarimeter detector. These studies lead to the conclusion that the laser-wire would require its own separate chicane.

Chapter 2

Theory

This chapter outlines the required accelerator, laser and particle physics theory. Some additional theory is presented in later chapters.

2.1 Beam Dynamics and Emittance Measurement

The purpose of the laser-wire is to carry out beam profile and emittance measurements at future $e^{\pm}$ accelerators such as the International Linear Collider (ILC). In this section, I outline basic beam dynamics, what emittance is and two methods for measuring it. The sources for this section are [4, 5].

We can describe the propagation of a large number of particles through magnetic fields such as dipole fields, which guide the beam, and quadrupole fields, which focus it. The motion of a single particle can be described by a set of linear equations, assuming that the magnetic fields are either independent of or linearly dependent on distance from the reference trajectory.

2.1.1 Reference Trajectory

The reference trajectory is defined as the trajectory of the ideal particle. The ideal particle is a conceptual particle that adheres to the perfect plan for the accelerator system [6]. In other words, it has exactly the right energy and arrives at exactly the right times at the accelerating structures to move exactly according to the plan for the accelerator. Its trajectory passes exactly through the centres of quadrupoles and high n-pole magnets and is deflected by bending magnets by exactly the right amount. Its transverse momentum at any point is zero. The reference trajectory traces

out a curve as it passes through bending magnets. We can define a coordinate system where s is the displacement along the reference trajectory, and the origin of the transverse position coordinates x and y follow the reference trajectory and are orthogonal to s.

2.1.2 Magnetic Rigidity

In accelerator physics we typically deal with the motion of charged particles in magnetic fields. The equation of motion of a particle with charge e in a magnetic field $\mathbf{B}$ with velocity $\mathbf{v}$ is

$$e\mathbf{v} \times \mathbf{B} = \frac{d\mathbf{p}}{dt} \tag{2.1}$$

where $\frac{d\mathbf{p}}{dt}$ is the rate of change of the relativistic momentum vector of the particle. We see from resolution of momenta that

$$\frac{d|\mathbf{p}|}{dt} = |\mathbf{p}|\frac{d\theta}{dt} = \frac{|\mathbf{p}|}{\rho}\frac{ds}{dt}, \tag{2.2}$$

where ρ is the radius of curvature of the (circular) trajectory of the particles. If the field and the plane of motion are normal then the magnitude of the corresponding force can be written:

$$e|\mathbf{v} \times \mathbf{B}| = e|\mathbf{B}|\frac{ds}{dt}. \tag{2.3}$$

By equating the right hand sides of Eq. 2.2 and 2.3 we find the expression

$$B\rho = \frac{p}{e}, \tag{2.4}$$

where $B\rho$ is called the "magnetic rigidity".

2.1.3 Focusing

Focusing in modern particle accelerators is done using alternating-gradient focusing with quadrupole magnets. There are three types of quadrupole magnets: those that focus in the horizontal axis and defocus in the vertical axis ("focusing" or "F" quadrupoles), those that do the opposite ("defocusing" or "D" quadrupoles) and skew quadrupoles, which are rotated at 45 degrees and couple the vertical and horizontal axis. Skew quadrupoles are of the same type as quadrupoles but just have a different orientation.

The strength of a quadrupole is equal to its field gradient normalised with respect to the magnetic rigidity,

$$k = \frac{1}{B\rho}\frac{dB_y}{dx}, \tag{2.5}$$

and so the angular deflection given to a particle passing through a short quadrupole of length l and strength k is

$$\Delta x' = \theta = \frac{lB}{B\rho} = \frac{l(dB_y/dx)x}{B\rho} = lkx \tag{2.6}$$

as, for a short quadrupole, $\theta \sim \frac{lB}{B\rho}$.

A principle called alternating-gradient focusing can be used to achieve a net focusing effect. Quadrupoles are placed in a lattice which alternates between focusing and defocusing .The positions and strengths of the magnets are chosen in such a way that a particle is closer to the reference trajectory at the defocusing magnets and further away from the reference trajectory at the focusing magnets. Because the field strength of a quadrupole is proportional to transverse displacement, the force acting on the particle at the focusing quadrupole is greater than the force acting on the particle at the defocusing quadrupole and a net focusing effect is achieved. If the quadrupoles are arranged in a periodic lattice then the equation of motion is also periodic. This equation is known as *Hill's equation* and is discussed in the next section.

2.1.4 Hill's Equation

The vertical angular deflection given to a particle passing through a short quadrupole of strength k and length ds at vertical displacement y is, from Eq. 2.6,

$$dy' = -kyds. \tag{2.7}$$

We have a restoring force acting on the particle to bring it towards zero displacement that is proportional to the displacement, so the equation of motion is similar to a mass on a spring. We can deduce from this a differential equation for the motion, which is similar to simple harmonic motion, as

$$y'' + k(s)y = 0 \tag{2.8}$$

where s is the displacement along the reference trajectory. This equation is called Hill's equation. The arrangement of magnetic fields in the accelerator is a periodic lattice, and so *k(s)* in Eq. 2.8 is a periodic function of s. For the horizontal plane, the sign of k is reversed and we include an extra term for the focusing due to the curvature of the orbit which can be significant in small rings:

$$x'' + \left[\frac{1}{\rho(s)} - k(s)\right] x = 0. \tag{2.9}$$

The solution to Hill's equation is found using *Floquet's theorem*, resulting in

$$x = \sqrt{(\beta(s)A)}\cos\left[\phi(s) + \phi_0\right]. \tag{2.10}$$

Where A is some constant, and is an invariant of the motion of a single particle. This solution is similar to that of the equation of simple harmonic motion varies with distance s instead of time t and has an extra term, $\beta(s)$. Another difference is that the phase $\phi(s)$ does not vary linearly with s. The functions $\beta(s)$ and $\phi(s)$ must have the same periodicity as that of the ring or a periodic lattice that comprises the ring or linear accelerator. By differentiating Eq. 2.10 we find that

$$x' = -\phi'(s)\sqrt{A\beta(s)}\sin\left[\phi(s) + \phi_0\right] + \left(\frac{\beta'(s)}{2}\right)\sqrt{\frac{A}{\beta(s)}}\cos\left[\phi(s) + \phi_0\right]. \tag{2.11}$$

For a collection of particles distributed in x and x' we can define a quantity ε called the *emittance*:

$$\varepsilon = \langle x\rangle\langle x'\rangle, \tag{2.12}$$

where the angle brackets denote the second moment. This can be thought of as an area in phase space.

The distribution of particles in an accelerator usually forms a Gaussian distributed ellipse in phase space. If we replace A with ε in Eqs. 2.10 and 2.11 so that

$$x = \sqrt{(\beta(s)\varepsilon)}\cos\left[\phi(s) + \phi_0\right] \tag{2.13}$$

and

$$x' = -\phi'(s)\sqrt{\varepsilon\beta(s)}\sin\left[\phi(s)+\phi_0\right] + \left(\frac{\beta'(s)}{2}\right)\sqrt{\frac{\varepsilon}{\beta(s)}}\cos\left[\phi(s)+\phi_0\right], \tag{2.14}$$

plotting x' against x using Eqs. 2.13 and 2.14 draws an ellipse with semi-axis $\sqrt{\beta\varepsilon}$ in x and $\sqrt{\varepsilon/\beta}$ in x'. This ellipse is called the *phase ellipse*. It has an area equal to $\pi\varepsilon$ and typically has the same shape as the particle distribution.

Liouville's theorem states that emittance is a conserved quantity under the influence of conservative forces.

2.1.5 Liouville's Theorem

Liouville's theorem states that the the area in phase space of a beam is conserved. We can plot beam particles' transverse positions and momenta, x and x', on a *phase space* diagram, conventionally with x' in the vertical axis and x in the horizontal axis. The distribution of particles will form some shape, usually an ellipse, around which a contour line can be drawn. The line is typically drawn at one standard deviation from the mean particle position/momentum. According to Liouville the area of this contour is conserved no matter what magnetic fields the beam may pass through. The "phase ellipse" can change its shape and orientation along the beam line but its area remains unchanged. Exceptions to these are operations which are velocity dependent such as emission of synchrotron radiation. Indeed, damping rings exploit this aspect of synchrotron radiation to "cool" charged particle beams, or reduce their emittance. Acceleration reduces the emittance because the acceleration causes and increase in the forward direction velocity vector, but not the transverse. However, there is a quantity called the *normalised emittance* that is conserved through acceleration, which is defined as [7]

$$\varepsilon^* \equiv \varepsilon\left(\gamma\frac{v}{c}\right) \tag{2.15}$$

In general, the lower the emittance of a beam, the smaller the size it can be focused to. However, at very small focus sizes other factors may come into play which limit the final focus size. For example, if the bunch length σ_z is comparable to β_x or β_y, the transverse particle distribution varies over a bunch length. This is known as the *hour glass effect* or *bunch length effect* [7].

2.1.6 Matrix description

Hill's equation is a linear differential equation and so the transformation of its solutions from one point to another can be represented by a *transfer matrix*. Therefore the solution at point s_2 can be traced from the solution at point s_1 like Eq. 2.16.

$$\begin{bmatrix} x(s_2-s_1) \\ x'(s_2-s_1) \end{bmatrix} = \begin{bmatrix} C(s_2-s_1) & S(s_2-s_1) \\ C(s_2-s_1)' & S(s_2-s_1)' \end{bmatrix} \begin{bmatrix} x(s_1) \\ x'(s_1) \end{bmatrix} = M_{21} \begin{bmatrix} x(s_1) \\ x'(s_1) \end{bmatrix} \tag{2.16}$$

Each lattice element (drift spaces, dipoles, quadrupoles, etc.) has its own transfer matrix. To trace a particle from one point to another we simply multiply together the transportation matrices in the correct order.

By defining $w = \sqrt{\beta}$, $\phi' = 1/\beta$ and substituting the solutions to Hill's equation, Eqs. 2.10 and 2.11 into Eq. 2.16, for two initial conditions $\phi = 0$ and $\phi = \frac{\pi}{2}$, we get four simultaneous equations. These equations can be solved for C, S, C' and S' in terms of w, w' and ϕ to find the transfer matrix:

$$\begin{bmatrix} \frac{w_2}{w_1}\cos\phi - w_2 w_1' \sin\phi & w_1 w_2 \sin\phi \\ -\frac{1+w_1 w_1' w_2 w_2'}{w_1 w_2}\sin\phi - \left(\frac{w_1'}{w_2} - \frac{w_2'}{w_1}\right)\cos\phi & \frac{w_1}{w_2}\cos\phi + w_1 w_2' \sin\phi, \end{bmatrix} \tag{2.17}$$

where $\phi = \phi_2 - \phi_1$. This is the most general form of the transfer matrix. However, accelerators are usually composed of periodic structures or "cells", and if the structure forms a ring around which particles circulate then the ring itself forms a periodic structure. If M is between points in successive cells in a periodic structure where the solutions to Hill's equation are equal then $w_2 = w_1$, $w_2' = w_1'$ and ϕ becomes μ, the phase advance per cell. Then,

$$M = \begin{bmatrix} \cos\mu - ww'\sin\mu & w^2\sin\mu \\ -\frac{1+w^2w'^2}{w^2}\sin\mu & \cos\mu + ww'\sin\mu \end{bmatrix} = \begin{bmatrix} C_p(s_2) & S_p(s_2) \\ C_p'(s_2) & S_p'(s_2) \end{bmatrix}. \tag{2.18}$$

This can be simplified further by defining the *Twiss parameters*:

$$\alpha = -ww' = -\beta'/2 \tag{2.19}$$

$$\beta = w^2 \tag{2.20}$$

$$\gamma = \frac{1+(ww')^2}{w^2} = \frac{1+\alpha^2}{\beta} \tag{2.21}$$

From Eq. 2.18 we can define C, S, C' and S' in terms of the Twiss parameters:

$$C = \cos\mu + \alpha\sin\mu \tag{2.22}$$

$$S = \beta\sin\mu \tag{2.23}$$

$$C' = -\gamma\sin\mu \tag{2.24}$$

$$S' = \cos\mu - \alpha\sin\mu \tag{2.25}$$

2.1.7 Twiss Parameters and the Beam Envelope

At any time each particle is at a six dimensional point in phase space $(x, x', y, y', \tau, \delta)$. The particle beam envelope occupies a region in phase space in x and a region in phase space in y. The beam's motion through an accelerator is described by the change in size, shape and orientation of this envelope. From the solution to Hill's equation, Eq. 2.11, the envelope is in the form of an ellipse (the *phase ellipse*) with equation

$$\gamma x^2 + 2\alpha x x' + \beta x'^2 = \varepsilon, \tag{2.26}$$

where x and x' are not the coordinates of an individual particle but of points of the phase ellipse. Here, α, β and γ are the Twiss parameters, Eqs. 2.19, 2.20, 2.21, and ε is the emittance. Fig. 2.1 shows how the dimensions and orientation of the phase ellipse are related to the Twiss parameters.

The Twiss parameters were defined for a *periodic* beam line.

In a drift space, a clockwise tilted ellipse in phase space corresponds to a diverging beam. An anti-clockwise rotated ellipse corresponds to a converging beam (Fig. 2.2).

In reality the orthogonal betatron motions can be coupled through rotational misalignment of quadrupoles and solenoid fields. This coupling can be corrected using skew quadrupoles and

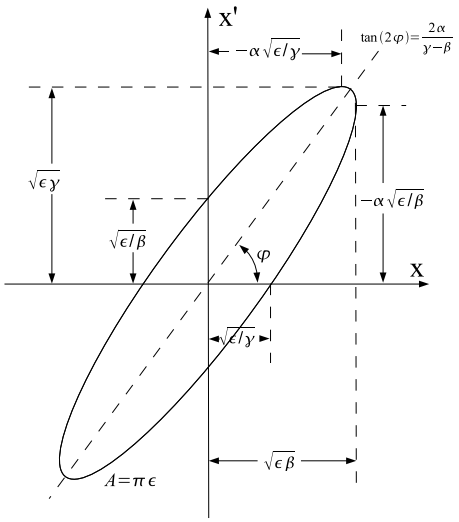

Figure 2.1: A diagram showing the relationship between the shape and orientation of the phase ellipse and the Twiss parameters.

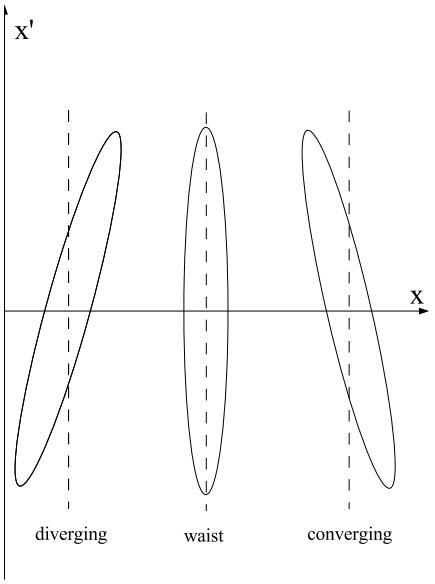

Figure 2.2: The transformation of a phase ellipse in drift space.

solenoid fields. For details see [7, 4].

The Twiss parameters were defined in Sec. 2.1.7 for a *periodic* beam line. However, the phase ellipse is merely a description of the distribution of particles in phase space. The Twiss parameters are the parameters of the phase ellipse's shape and orientation. During transportation along a beam line the phase ellipse continually changes its shape and orientation according to the transfer matrix (Sec. 2.1.8). The transfer matrix can be formulated for any beam line or section of beam line, and is not necessarily periodic.

2.1.8 Transformation of the Phase Ellipse

Any particle trajectory transforms from the starting point $s = 0$ to another point $s \neq 0$ like

$$\begin{bmatrix} x \\ x' \end{bmatrix} = \begin{bmatrix} C(s) & S(s) \\ C'(s) & S'(s) \end{bmatrix} \begin{bmatrix} x_0 \\ x'_0 \end{bmatrix}. \tag{2.27}$$

Solving 2.27 for x and x_0 we find

$$x = C(s)x_0 + S(s)x'_0, x' = C'(s) + S'(s). \tag{2.28}$$

Substituting Eqs. 2.27 into the equation of the phase ellipse, Eq. 2.26, we get

$$\begin{bmatrix} \beta \\ \alpha \\ \gamma \end{bmatrix} = \begin{bmatrix} C^2 & -2SC & S^2 \\ -CC' & (S'C + SC') & -SS' \\ C'^2 & -2S'C' & S'^2 \end{bmatrix} \begin{bmatrix} \beta_0 \\ \alpha_0 \\ \gamma_0. \end{bmatrix} \tag{2.29}$$

An ellipse is defined by three parameters: the area, orientation and ellipticity. The area is defined by ε. This leaves α, β and γ to define the orientation and ellipticity. Only two parameters are required to define the orientation and ellipticity, therefore we expect these three parameters to be correlated. From geometric properties of an ellipse we find this correlation to be Eq. 2.21.

2.1.9 Emittance Measurement

The relationship between the emittance, Twiss parameters and phase ellipse is given by Eq. 2.26.

Due to Liouville's theorem, Sec. 2.1.5, ε stays the same but α, β, γ can change along the beam line. The beam profile can be measured but the transverse momentum distribution is difficult to measure directly. Therefore, in order to obtain an emittance measurement a minimum of three

beam profile measurements must be made at different locations so that different parts of the transforming phase ellipse are probed. The measurements are fit to equations involving beam transformation matrices (which can be determined from the positions and characteristics of the quadrupoles).

As we have already established, the beam envelope forms an ellipse in phase space. The equation for a n-dimensional ellipse can be written in the form

$$\mathbf{u}^{\mathrm{T}}\sigma^{-1}\mathbf{u} = 1 \tag{2.30}$$

where $\mathbf{u}$ is a n-dimensional vector defined by

$$\mathbf{u} = \begin{pmatrix} x \\ x' \\ y \\ y' \\ \tau \\ \delta \\ \dots \\ \dots \end{pmatrix}, \tag{2.31}$$

where x, x', y, y' are the transverse phase space coordinates, τ, δ are longitudinal phase space coordinates and σ is a symmetric matrix yet to be determined (in this case σ is the *beam matrix*).

The volume of a n-dimensional ellipse is given by

$$V_n = \frac{\pi^{n/2}}{\Gamma(1+n/2)}\sqrt{\det\sigma} \tag{2.32}$$

where Γ is the gamma function.

In the two dimensional $\mathbf{u} = \begin{pmatrix} x \\ x' \end{pmatrix}$ case,

$$V_2 = \pi\sqrt{\det\sigma}. \tag{2.33}$$

We have already shown that the area of the phase ellipse is equal to π times the emittance ε, therefore

$$\varepsilon^2 = \det\sigma. \tag{2.34}$$

Using the determinant method of calculating the inverse of a 2×2 matrix,

$$\sigma^{-1} = \frac{1}{\det\sigma}\begin{pmatrix} \sigma_{22} & -\sigma_{12} \\ -\sigma_{12} & \sigma_{11} \end{pmatrix} \tag{2.35}$$

Substituting Eq. 2.34 into Eq. 2.35,

$$\sigma^{-\mathbf{1}} = \frac{1}{\varepsilon^2}\begin{pmatrix} \sigma_{22} & -\sigma_{12} \\ -\sigma_{12} & \sigma_{11} \end{pmatrix} \tag{2.36}$$

Therefore, from Eqs. 2.36 and 2.30, we get

$$\sigma_{22}x^2 - 2\sigma_{12}x'x + \sigma_{11}x'^2 = \varepsilon^2. \tag{2.37}$$

The beam matrix σ is therefore defined as

$$\sigma = \begin{bmatrix} \sigma_{11} & \sigma_{12} \\ \sigma_{12} & \sigma_{22} \end{bmatrix} = \varepsilon \begin{bmatrix} \beta & -\alpha \\ -\alpha & \gamma \end{bmatrix} \tag{2.38}$$

in the two dimensional case, consistent with Eq. 2.26. The physical interpretation of σ is that it is a matrix that can be used to describe an n-dimensional phase ellipse.

Let $\mathcal{M}$ be the matrix which transforms the vector $\mathbf{u}$ from point P_0 to point P_1. This is general, and can be applied to the n-dimensional case. We have

$$\mathbf{u_0} = \mathcal{M}\mathbf{u_1} \tag{2.39}$$

and

$$\mathbf{u}_0 = \mathcal{M}^{-1}\mathbf{u}_1. \tag{2.40}$$

Using Eqs. 2.40 and 2.30 we find

$$(\mathcal{M}^{-1}\mathbf{u}_1)^{\mathrm{T}}\sigma_0^{-1}(\mathcal{M}^{-1}\mathbf{u}_1) = 1, \tag{2.41}$$

which after some manipulation becomes

$$\mathbf{u}_1^{\mathrm{T}}(\mathcal{M}^{\mathrm{T}})^{-1}\sigma_0^{-1}\mathcal{M}^{-1}\mathbf{u}_1 = 1. \tag{2.42}$$

Using the identity $(\mathcal{M}^{\mathrm{T}})^{-1}\sigma_0^{-1}\mathcal{M}^{-1} = [\mathcal{M}\sigma_0\mathcal{M}^{\mathrm{T}}]^{-1}$, we can write the above equation as

$$\mathbf{u}_1^{\mathrm{T}}[\mathcal{M}\sigma_0\mathcal{M}^{\mathrm{T}}]^{-1}\mathbf{u}_1 = 1. \tag{2.43}$$

By comparing Eqs. 2.43 and 2.30, we find that the beam matrix transforms like

$$\sigma_1 = \mathcal{M}\sigma_0\mathcal{M}^{\mathrm{T}}. \tag{2.44}$$

From Eqs. 2.29 and 2.38 we have

$$\begin{bmatrix}\sigma_{1,11}\\ \sigma_{2,11}\\ \sigma_{3,11}\end{bmatrix} = \mathcal{M}_\sigma \begin{bmatrix}\sigma_{0,11}\\ \sigma_{0,12}\\ \sigma_{0,22}\end{bmatrix} \tag{2.45}$$

where

$$\mathcal{M}_\sigma = \begin{bmatrix}C_1^2 & 2C_1S_1 & S_1^2\\ C_2^2 & 2C_2S_2 & S_2^2\\ C_3^2 & 2C_3S_3 & S_3^2\end{bmatrix}. \tag{2.46}$$

$\sigma_{i,kj1}$ are the elements of the beam matrix at locations P_i and C_i, S_i are elements of the transformation matrix from point P_0 to P_i, which is known from the beam line elements between P_0 and P_i. This can be solved for the beam matrix elements at P_0;

$$\begin{bmatrix}\sigma_{0,11}\\ \sigma_{0,12}\\ \sigma_{0,22}\end{bmatrix} = \mathcal{M}_\sigma^{-1} \begin{bmatrix}\sigma_{1,11}\\ \sigma_{2,11}\\ \sigma_{3,11}\end{bmatrix}. \tag{2.47}$$

Therefore the elements of σ can be determined, and using Eq. 2.34 the emittance can be calculated.

The emittance is important for the design and operation of accelerators in order to achieve a high luminosity. Emittance measurements at the ILC will be made using many laser-wire

systems.

Measuring particle distributions of small electron bunches is challenging. In order to carry out an emittance measurement, a scheme has been devised where beam size measurements will carried out at 4 or 5 locations along the two transverse axes and a third angle and fit to a matrix equation (2.46) in order to achieve the desired resolution. The third angle takes transverse beam tilt into account. The minimum number of wire scanners needed to perform an emittance measurement without changing the optics is 6 (1 in each plane, at three locations), suitably placed in betatron phase. An emittance measurement is performed by measuring beam sizes with these wires and using these data to reconstruct the beam matrix (see [8] for details).

The electron beam size measurements are subject to uncertainties from various sources. Uncertainties from the machine itself come in the form of beam jitter and residual dispersion, and there is an error associated with laser-wire scans. When an effect contributes to a measurement error, we define E_{effect} as its contribution to the total relative error. The uncertainties add in quadrature as [8]

$$\left(\frac{\delta\sigma_e}{\sigma_e}\right)^2 = E_{\text{scan}}^2 + E_{\text{jitter}}^2 + E_{\eta}^2, \tag{2.48}$$

where "jitter" is the bunch position jitter and E_η is an error due to residual dispersion. Therefore care must be taken to minimise both machine related and laser-wire related sources of error.

2.2 Dispersion

Apart from emittance, the other contribution to electron beam size comes in the form of *dispersion*. Dispersion is defined as the increase in horizontal or vertical size a beam will experience due to its energy spread, and typically varies along a beam line. Dispersion is introduced by dipole fields and derives from the fact that the trajectories of particles of different momenta are deflected by different amounts in the same dipole field (Eq. 2.1). Thus, a spread of particle momenta within a beam passing through a dipole field creates a spread of particle positions.

We can deduce how the dispersion and β function contribute to the total beam size by using the six-dimensional beam matrix and the 6-dimensional transportation matrix of a dipole (uniform wedge bend). The six dimensional beam matrix contains the following elements [7]: $\sigma_{11} = x_{\text{max}}^2$, $\sigma_{22} = x_{\text{max}}'^2$, $\sigma_{33} = y_{\text{max}}^2$, $\sigma_{44} = y_{\text{max}}'^2$, $\sigma_{55} = l_{\text{max}}^2$ and $\sigma_{66} = (dP/p_0)_{\text{max}}^2$. The trans-

formation of the six dimensional beam matrix is given by Eq. 2.44:

$$\Sigma_2 = \mathcal{M}\Sigma_0\mathcal{M}^{\mathrm{T}} = \begin{bmatrix} \mathcal{M}_{11} & 0 & \mathcal{M}_{13} \\ 0 & \mathcal{M}_{22} & 0 \\ \mathcal{M}_{31} & 0 & \mathcal{M}_{33} \end{bmatrix} \begin{bmatrix} \Sigma_{11} & 0 & 0 \\ 0 & \Sigma_{22} & 0 \\ 0 & 0 & \Sigma_{33} \end{bmatrix} \begin{bmatrix} \mathcal{M}_{11}^{\mathrm{T}} & 0 & \mathcal{M}_{31}^{\mathrm{T}} \\ 0 & \mathcal{M}_{22}^{\mathrm{T}} & 0 \\ \mathcal{M}_{13}^{\mathrm{T}} & 0 & \mathcal{M}_{33}^{\mathrm{T}} \end{bmatrix}, \tag{2.49}$$

where each of the $\mathcal{M}_{ij}$, Σ_{ij} elements in the above matrices is a 2×2 matrix:

$$\Sigma_{11} = \begin{bmatrix} \sigma_{11} & \sigma_{12} \\ \sigma_{12} & \sigma_{22} \end{bmatrix} \tag{2.50}$$

$$\Sigma_{22} = \begin{bmatrix} \sigma_{33} & \sigma_{34} \\ \sigma_{34} & \sigma_{44} \end{bmatrix} \tag{2.51}$$

$$\Sigma_{33} = \begin{bmatrix} \sigma_{55} & \sigma_{56} \\ \sigma_{56} & \sigma_{66} \end{bmatrix} \tag{2.52}$$

We are interested is the horizontal beam width at position 2, which is the $\sigma_{2,11}$. By carrying out the above matrix multiplication, we find that

$$\Sigma_{2,11} = \mathcal{M}_{11}\Sigma_{11}\mathcal{M}_{11}^{\mathrm{T}} + \mathcal{M}_{13}\Sigma_{13}\mathcal{M}_{13}^{\mathrm{T}}. \tag{2.53}$$

where

$$\mathcal{M}_{11} = \begin{bmatrix} C & S/h \\ -hS & C \end{bmatrix} \tag{2.54}$$

and

$$\mathcal{M}_{13} = \begin{bmatrix} S & \frac{1-C}{h} \\ 0 & 0. \end{bmatrix}. \tag{2.55}$$

In Eqs. 2.54 and 2.55, $C = \cos\alpha$, $S = \sin\alpha$ and $h = \frac{1}{\rho_0}$, where α is the bending angle of the dipole and ρ_0 is the radius of curvature of the dipole.

From Eq. 2.53 one can conclude that there are two contributions to the beam size: from the

beta function and from the dispersion function, and that these add in quadrature to the total beam size σ_e:

$$\sigma(s)_e = \sqrt{\beta(s)\varepsilon + D(s)^2 \left(\frac{\Delta p}{p}\right)^2}, \tag{2.56}$$

where σ is the beam size, $\beta(s)$ is the beta function, ε is the emittance, p is the momentum and $D(s)$ is the dispersion function.

In order to solve the shape of the dispersion function [5] the dispersion may be thought of as a driving term in Hill's equation (Eq. 2.8):

$$\frac{d^2x}{ds^2} + k(s)x = -\frac{1}{\rho(s)}\frac{\Delta p}{p} \tag{2.57}$$

where $\rho(s)$ is the local curvature in a dipole bending magnet.

In practice the dispersion function in the ATF extraction line was solved using the MAD [9, 10, 11] accelerator simulation code.

2.3 Compton Scattering

In high luminosity machines such as the ILC, the currently available methods of beam profile measurement such as wire scanners can not be used because the beam would destroy the wire. Also, wire scanners are invasive; they disrupt the beam and therefore cannot be used concurrently with machine luminosity running. This might decrease the integrated luminosity. Another method, to use Compton scattered light, is the subject of this thesis. The Feynman diagrams for this process are shown in Fig. 2.3.

See [12] for the original paper on Compton scattering. The main results for Compton scattering at ultra-relativistic energies are as follows [13]:

$$\langle n_\gamma \rangle = \frac{\sigma_C}{ch\nu_0}\rho_L D N_e \tag{2.58}$$

where $\langle n_\gamma \rangle$ is the average number of Compton scattered photons per bunch, σ_C is the Compton scattering cross section, c is the speed of light, h is Planck's constant, ν_0 is the frequency of the incoming photons, N_e is the number of electrons per bunch and ρ_L is the power density of the laser beam. The laser power is assumed to be uniformly distributed over a distance along the

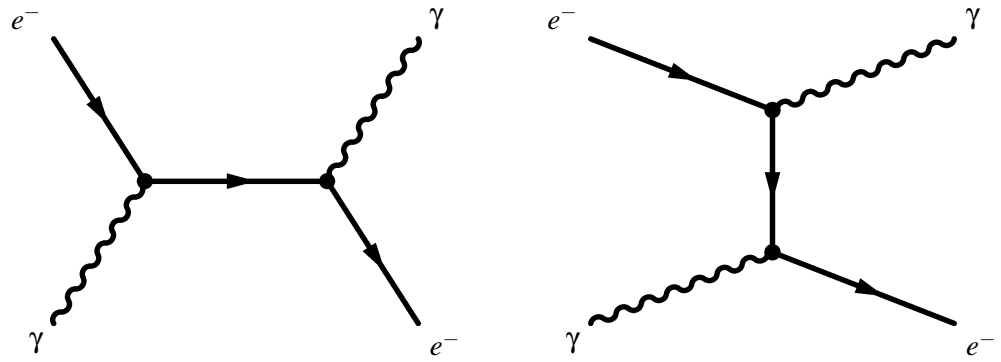

Figure 2.3: Feynman diagrams for Compton scattering. Time goes from left to right. Left diagram: *s* channel. Right diagram: *t* channel.

laser's trajectory, D, that overlaps with the electron beam. The Compton cross section is related to the Thomson scattering cross section, $\sigma_T \equiv 6.65 \times 10^{-25}\text{cm}^2$, by equation 2.59.

$$\frac{\sigma_C}{\sigma_T} = \frac{3}{4}\left\{\frac{1+\varepsilon_1}{\varepsilon_1^3}\left[\frac{2\varepsilon_1(1+\varepsilon_1)}{1+2\varepsilon_1} - \ln(1+2\varepsilon_1)\right] + \frac{1}{2\varepsilon_1}\ln(1+2\varepsilon_1) - \frac{1+3\varepsilon_1}{(1+2\varepsilon_1)^2}\right\} \tag{2.59}$$

where $\varepsilon_1 \equiv \frac{\gamma h\nu_0}{m_e c^2}$ is the normalised energy of the laser photons in the electron rest frame, and gamma here is the relativistic factor.

The energy spectrum of the outgoing photons is given by

$$\frac{d\sigma/\sigma_T}{d\omega} = \frac{3}{8\varepsilon_1}F(\varepsilon_1,\omega) \tag{2.60}$$

where $\omega \equiv h\nu_\gamma/E$ is the energy of the scattered photon normalised to the electron energy, and F is given by

$$F(\varepsilon_1,\omega) = \frac{1}{1-\omega} + 1 - \omega + \left[\frac{\omega}{\varepsilon_1(1-\omega)}\right]^2 - \frac{2\omega}{\varepsilon_1(1-\omega)}. \tag{2.61}$$

The maximum photon energy is given by $h\nu_{\max} = 2E\varepsilon_1/(1+2\varepsilon_1)$. The critical angle is given by $\alpha_c = \frac{\sqrt{1+2\varepsilon_1}}{\gamma}$.

2.3.1 Wave Optics and Gaussian Beams

The scalar wave equation that governs electromagnetic fields in free space is

$$[\nabla^2 + k^2]\tilde{E}(x,y,z) = 0, \tag{2.62}$$

where $\tilde{E}(x,y,z)$ is the phasor amplitude of a distribution that is sinusoidal in time.

We take the direction of propagation of our beam to be the z direction, so the primary spatial dependence is e^{-ikz}, which has a spatial period of one wavelength, λ.

For a reasonably well collimated beam the transverse variations in the profile are slow compared with the plane-wave variation in the z direction. Therefore we can write

$$\tilde{E}(x,y,z) \equiv \tilde{u}(x,y,z)e^{-ikz}. \tag{2.63}$$

Substituting this into 2.62 yields

$$\frac{\partial^2\tilde{u}}{\partial x^2} + \frac{\partial^2\tilde{u}}{\partial y^2} + \frac{\partial^2\tilde{u}}{\partial z^2} - 2ik\frac{\partial\tilde{u}}{\partial z} = 0. \tag{2.64}$$

Now that the e^{-ikz} dependence is factored out, the remaining z dependence of $\tilde{u}(x,y,z)$ is slow compared to the transverse variations due to the finite width of the beam, and is caused by diffraction effects. Therefore the *paraxial approximation* can be applied where $\frac{\partial^2\tilde{u}}{\partial z^2}$ can be neglected and Eq. 2.64 is then known as the *paraxial wave equation*. It can be more generally expressed as

$$\nabla_t^2\tilde{u}(\mathbf{s},z) - 2ik\frac{\partial\tilde{u}(\mathbf{s},z)}{\partial z} = 0, \tag{2.65}$$

Where ∇_t^2 is the Laplacian operator operating on the transverse coordinates $\mathbf{s} \equiv (x,y)$ or $\mathbf{s} \equiv (r,\theta)$ in the transverse plane.

A uniform spherical wave diverging from a point source $\mathbf{r_0}$ can be expressed as

$$\tilde{E}(\mathbf{r};\mathbf{r_0}) = \frac{\exp[-ik\rho(\mathbf{r}\mathbf{r_0})]}{\rho(\mathbf{r},\mathbf{r_0})} \tag{2.66}$$

where $\tilde{E}(\mathbf{r};\mathbf{r_0})$ means the field at point $\mathbf{r}$ due to the point source at $\mathbf{r_0}$ and the distance from the source point $\mathbf{s_0}$, z_0 to the observation point $\mathbf{s}$, z is

$$\rho(\mathbf{r},\mathbf{r_0}) = \sqrt{(x-x_0)^2 = (y-y_0)^2 + (z-z_0)^2}. \tag{2.67}$$

If the source point is not too far from the z axis , and we want to write the field distribution for values of x and y not to far from the z axis somewhere farther along the z axis we can use the *Fresnel approximation* by expanding $\rho(\mathbf{r},\mathbf{r_0})$ in a power series in the form

$$\rho(\mathbf{r},\mathbf{r_0}) = z - z_0 + \frac{(x-x0)^2+(y-y_0)^2}{2(z-z_0)} + ..., \tag{2.68}$$

and drop all the terms higher than quadratic in this expression. In the denominator of Eq. 2.66 we can replace the denominator with simply $z-z_0$. Eq. 2.66 is then converted to

$$\tilde{E}(x,y,z) = \frac{1}{z-z_0}\exp\left[-ik(z-z_0) - ik\frac{(x-x_0)^2+(y-y_0)^2}{2(z-z_0)}\right] \tag{2.69}$$

$$\tag{2.70}$$

or

$$\tilde{u}(x,y,z) = \frac{1}{z-z_0}\exp\left[-ik\frac{(x-x_0)^2+(y-y_0)^2}{2(z-z_0)}\right] \tag{2.71}$$

$$= \frac{1}{R_z}\exp\left[-ik\frac{(x-x_0)^2+(y-y_0)^2}{2R_z}\right] \tag{2.72}$$

$$= \frac{1}{R_z}\exp\left[-i\phi(x,y,z)\right] \tag{2.73}$$

where R_z gives the radius of curvature of the spherical wave at plane z and

$$\phi(x,y,z) \equiv k\frac{(x-x_0)^2+(y-y_0)^2}{2R_z} = \frac{\pi}{\lambda}\frac{(x-x_0)^2+(y-y_0)^2}{R_z} \tag{2.74}$$

The paraxial wave, Eq. 2.71 does not represent a physical wave because the amplitude does not fall off with transverse extent, and instead extends out to infinity. The beams we are interested in have finite transverse extent. This amplitude distribution can be included by replacing the real radius of curvature, R_z, by a complex radius of curvature, $\tilde{q}_z = \tilde{q}_0 + z - z_0$, in Eq. 2.71, yielding

$$\tilde{u}(x,y,z) = \frac{1}{z-z_0+\tilde{q}_0}\exp\left[-ik\frac{x^2+y^2}{2(z-z_0+\tilde{q}_0)}\right] = \frac{1}{\tilde{q}_z}\exp\left[-ik\frac{x^2+y^2}{2\tilde{q}_z)}\right]. \tag{2.75}$$

If we separate the inverse of the complex radius of curvature into real and imaginary parts, such

that

$$\frac{1}{\tilde{q}_z} \equiv \frac{1}{\tilde{q}_{rz}} - i\frac{1}{\tilde{q}_{iz}} \tag{2.76}$$

then we can express the spherical wave in the form

$$\tilde{u}(x,y,z) = \frac{1}{\tilde{q}_z}\exp\left[-ik\frac{x^2+y^2}{2q_{rz}} - k\frac{x^2+y^2}{2q_{iz}}\right]. \tag{2.77}$$

This beam has a purely real transverse variation giving a Gaussian transverse amplitude profile.

In standard notation, Eq. 2.77 is written

$$\tilde{u}(x,y,z) = \frac{1}{\tilde{q}_z}\exp\left[-ik\frac{x^2+y^2}{2R_z} - \frac{x^2+y^2}{W_z^2}\right] \tag{2.78}$$

where R_z is the radius of curvature and W_z is the Gaussian spot size, which is equivalent to twice the second moment of the Gaussian distribution (2σ). Therefore

$$\frac{1}{\tilde{q}_z} \equiv \frac{1}{R_z} - i\frac{\lambda}{\pi W_z^2} \tag{2.79}$$

and the fundamental propagation law for Gaussian beams is

$$\tilde{q}_z = \tilde{q_0} + z - z_0. \tag{2.80}$$

Single mode Gaussian beams are the most desirable type of laser beam for many applications, including the laser-wire. They are well characterised, smooth and easily predicted, and provide high spatial density. They are also simple to deconvolve from the laser-wire signal; the equation for the case with infinite Rayleigh range is shown in Eq. 2.100. As we shall see, in practice other modes are often present, and these are detrimental to the quality of the laser beam and the performance of the laser-wire system in terms of the minimum spot size that can be achieved and, consequently, the minimum transverse electron beam size that can be measured.

We define

$$z_R = \frac{\pi W_0^2}{\lambda}, \tag{2.81}$$

where W_0 is the beam size at the waist. Then the initial value $< tildeq$ in Eq. 2.80 is

$$\tilde{q}_0 = iz_R. \tag{2.82}$$

From this we can define three propagation formulas, which relate all the important parameters of Gaussian laser beams to the waist spot size W_0 and the ratio z/z_R:

$$W = W_0\sqrt{1+\left(\frac{(z-z_0)\lambda}{\pi W_0^2}\right)^2}, \tag{2.83}$$

$$R_z = z + \frac{z_R^2}{z}, \tag{2.84}$$

$$\phi_z = \tan^{-1}\left(\frac{z}{z_R}\right). \tag{2.85}$$

In practice Gaussian laser beams are not pure 1st order but contain additional modes. These extra modes increase W_0. We can account for this by introducing a quality factor called M^2 [14]. In the diffraction limited case, $M^2 = 1$. Lasers with $M^2 > 1$ are said to be "M^2 times diffraction limited". Using this concept one only has to replace λ with $M^2\lambda$ in all equations to account for the quality of the laser beam. This leads to a more general version of Eq. 2.83:

$$W = W_0\sqrt{1+\left(\frac{(z-z_0)M^2\lambda}{\pi W_0^2}\right)^2}. \tag{2.86}$$

W increases by a factor of $\sqrt{2}$ between W_0 and z_R, which is called the *Rayleigh range*.

The divergence angle of the beam tends to a constant far from focus. W is defined as the distance from the centre of the transverse beam profile where the amplitude falls to $1/e$ times the maximum amplitude. We shall use the $1/e$ or 86% criterion to define the far field divergence angle:

$$\theta_{1/e} = \lim_{z\to\infty}\frac{W_z}{z} = \frac{\lambda}{\pi W_0} \tag{2.87}$$

and

$$W_z \approx \frac{W_0}{z_R} = \frac{\lambda z}{\pi W_0} \tag{2.88}$$

for $z >> z_R$, therefore

$$W_0 \times W_z \approx \frac{\lambda z}{\pi}. \tag{2.89}$$

Therefore if W_{in} is the spot size at a focusing lens (the input spot size) then

$$W_0 \times W_{\text{in}} \approx \frac{\lambda f}{\pi} \tag{2.90}$$

where f is the focal length of the lens. The f-number of a focusing lens is defined as

$$f^{\#} \equiv \frac{f}{\pi W_{\text{in}}}. \tag{2.91}$$

It appears from this simple relation that to minimise the focus spot size we need to make W_{in} as large as possible, filling the lens aperture. However, over filling the lens can introduce spherical aberrations. Simulation and measurements of the custom laser-wire lens (Sec. 4.3.1) show that it suffers from second order spherical aberrations (the first order aberrations were corrected), and the best focus spot size with this lens can be achieved by limiting W_{in}.

2.3.2 Sources of M^2

Possible sources of M^2 include the following:

1. Thermal lensing.
2. Thermally induced birefringence.
3. Uneven pump light.
4. Optical defects including dust.
5. Damage to the linear amplifier surfaces.
6. Stability.
7. Spatial filtering.

2.3.3 Laser-wire Compton Rates and Laser Propagation

In the laser-wire the laser propagation axis is at right angles with the electron beam propagation axis, coming in from the right hand side when facing in the direction of electron beam propaga-

tion. This section discusses the overlap between the laser and electron beam, so for convenience in this section we switch from laser to accelerator coordinates. The longitudinal laser coordinate z is now called x and the transverse laser coordinate x is now called z. The name of the vertical axis y remains unchanged.

For electron beam energy E_b and laser photon energy $k = \frac{hc}{\lambda}$, with $\omega = \frac{kE_b}{m_e^2}$, the Compton cross section is given by Eq. 2.59 [8]. The rate of Compton scattering will be proportional to the overlap between the electron beam and the laser beam, as calculated by a three dimensional *overlap integral* of the functions describing the spatial distributions of the quanta in the beams.

$$N(\delta_x, \delta_y) = N_0 \varepsilon(\delta_x, \delta_y) \tag{2.92}$$

where N is the number of Compton photons produced, ε is the overlap integral, which for the TM_{00} mode is Eq. 2.96, and

$$N_0 = \frac{P_l N_e \lambda f(\omega) \sigma_T}{hc^2}, \tag{2.93}$$

where P_l is the instantaneous laser beam power at the laser-wire IP, N_e is the number of electrons in the bunch, $f(\omega)$ is equal to the ratio of Compton and Thomson scattering cross sections, $\frac{\sigma_C}{\sigma_T}$ in Eq. 2.59.

A longitudinal (z) quantity called the Rayleigh range, x_R, is defined as the distance from the waist along the laser propagation direction at which the transverse beam width, σ, becomes $\sqrt{2}$ times the waist size, σ_l. and in the M^2 model of laser propagation can be defined as

$$x_R = M^2 \frac{4\pi\sigma_l^2}{\lambda} \tag{2.94}$$

where M^2 is the laser "quality factor" (Sec. 2.3.1) and σ_0 is the diffraction limited beam size at the laser waist, $\lambda f^{\#}$. If only the TM_{00} mode is present then the quality factor is 1. The presence of other modes increases the quality factor. The waist size is also limited by the $f^{\#}$ of the lens which is defined in Eq. 2.91, and the wavelength of the light, λ:

$$\sigma_{\mathrm{lw}} = M^2 \sigma_0 = M^2 \lambda f^{\#} \tag{2.95}$$

Therefore the smallest possible beam size is achieved when $M^2 = 1$ and $f^{\#} = 1$.

Using the TM_{00} laser mode, the transverse overlap integral is

$$\varepsilon(\delta_x,\delta_y)=\int\frac{dxdyI_lI_e}{(2\pi)^{3/2}\sigma_{ex}\sigma_{ey}\sigma_l\sqrt{f_R(x-\delta_x)}}, \tag{2.96}$$

where

$$f_R(x)=1+\left(\frac{x}{x_R}\right)^2, \tag{2.97}$$

where x_R is the Rayleigh range. Integrating Eq. 2.96 over y gives

$$\varepsilon(\delta_x,\delta_y)=\frac{I_lI_e}{2\pi\sigma_{ex}}\int\frac{dx}{\sigma_s(x,\delta_x)}\exp\left[-\frac{x^2}{2\sigma_{ex}^2}-\frac{\delta_y^2}{2\sigma_s^2(x,\delta_x)}\right]. \tag{2.98}$$

where

$$\sigma_s(x,\delta_x)=\sqrt{\sigma_{ey}^2+\sigma_l^2f_R(x-\delta_x)}. \tag{2.99}$$

With infinite Rayleigh range, $f_R(x-\delta_x)\sim 1$ and the vertical width of the Compton scattering profile reduces to the sum in quadrature of the vertical widths of the electron beam and the laser beam, that is

$$\sigma_{sy}^2=\sigma_{ey}^2+\sigma_{ly}^2. \tag{2.100}$$

If the Rayleigh range is small, however, or comparable to the horizontal size of the electron beam, then the more general form Eq. 2.99 is needed.

2.3.4 Simulation of Compton Scattering

Compton scattering was simulated in order to test the performance of the laser-wire under various machine conditions (Chapter 6). The Compton scattered photons themselves were generated in the way described in [15]. The Monte Carlo uses a Lorentz transformation to obtain the energy of the photon in the electron rest frame:

$$k^*=\gamma k_i(1-\beta\cos\psi) \tag{2.101}$$

If k^* is is small compared to the electron mass and the Compton scattering is well approxi-

mated by the elastic Thomson scattering process. The scattered photon energy is $k^{*\prime} \sim k^*$. The angular distribution of Thomson scattering is $1+\cos^2\theta$.

The Monte Carlo simulation process is as follows:

1. We start with an incoming electron and a laser photon with a given direction.
2. Lorentz-transformation of the photon into the electron rest frame.
3. Rotation of photon to $+z$ direction.
4. Generation of Compton scattering angles using the Thomson cross section an approximation.
5. Rejection of a few % of events to correct for the ration Compton/Thomson cross section.
6. Rotate the scattered photon (using the inverse matrix of step **3**.
7. Lorentz transform the photon back into the lab frame. The scattered electron coordinates are obtained from energy-momentum conservation.

The process is set up such that every incoming electron produces is scattered. In steps **4** and **5** a set of random numbers r_i are generated. The ϕ scattering angle is generated using $r_1\phi$.

The maximum value of n random numbers has the probability distribution $f(x) = x^{n-1}$ [16]. This is used to generate θ following a $1+\cos^2\theta$ distribution by choosing a flat

$$\cos\theta = 2 \cdot r_2 - 1 \tag{2.102}$$

distribution in 75% of cases and

$$\cos\theta = \pm \max(r_3, r_4, r_5) \tag{2.103}$$

in the remaining 25%.

The ratio of scattered to unscattered photon energy, x, is

$$x = \frac{k'}{k} = \left[1 + \frac{k}{m_e} \cdot (1-\cos\theta)\right]^{-1}. \tag{2.104}$$

at $x = 1$, the Thomson and Compton cross sections are equal. The exact Compton spectrum is obtained using the rejection technique.

For 532 nm wavelength photons and a 3 GeV electron beam (ATF laser-wire), $k^* = 1.14 \cdot 10^{-2} m_e$ which is small compared to the electron mass and so the differential cross section can be approximated using the Thomson cross section. For a 532 nm photon and a 250 GeV electron (ILC laser-wire), $k* = 2.24 m_e$, which is not small compared to the electron mass. Therefore, the generation of Compton scattering angles in the electron rest frame in step **4** of the Monte Carlo simulation process outlined above is not well approximated by the elastic Thomson process. Therefore the accuracy of ILC laser-wire simulations in Sec. 6.3 could be improved by using the full Compton differential cross section in step **4** of the Monte Carlo simulation process.

2.4 Optical Diffraction Radiation

Optical transition radiation (OTR) appears when a charged particle moves between two media with different electromagnetic properties. Optical diffraction radiation (ODR) appears when a charged particle goes through an aperture or moves in the vicinity of a foil [17]. The foil needs to be a conductor. This can be used as a non invasive beam size diagnostic tool. An ODR beam size measurement system was developed at KEK [18, 19] and the target from this system was used in the laser-wire system. The knife edge consists of a silicon wafer coated in gold. Silicon was used because it has a very smooth surface. Gold is a good conductor so increases ODR/OTR production. Furthermore, it is easier to evaporate than other metals so the surface could be well controlled. A thin knife edge was cut along a crystal plane at the end of the wafer.

Derivation of the theory of ODR and OTR has been well studied (see [18, 19] for further sources).

ODR was used in the laser-wire system as a tool for finding the spatial and temporal overlap between the laser beam and electron beam (Secs. 3.3.9, 4.4.1). Under conditions similar to that in the ATF extraction line:

1. The radiation emitted is in the optical wavelength scale.
2. The signal to noise ratio is high.
3. The signal is angularly dependent.
4. Photon yield is inversely proportional to the distance between the electron beam and the knife edge.

2.5 Synchrotron Radiation

2.5.1 Synchrotron Radiation Power

During acceleration, charged particles radiate due to a rearrangement of their electric fields. This field perturbation travels away as synchrotron radiation (SR). In storage rings a large amount of SR is produced as the particles pass through the bending magnets which keep the beam in orbit. The main reason to build a linear, rather than circular, electron positron collider is because of the large amounts of energy lost due to SR in circular electron machines beyond a certain energy. The instantaneous synchrotron radiation power is [20]

$$P_\gamma[\text{GeV s}^{-1}] = \frac{cC_\gamma}{2\pi}\frac{E^4}{\rho^2}, \tag{2.105}$$

where $C_\gamma = \frac{4\pi}{3}\frac{r_c}{(mc^2)^3} = 8.8575 \times 10^{-5}$ m/GeV^3 is the *radiation constant*, E is the energy, ρ is the bending radius of the particle's trajectory in the magnetic field, r_c is the classical particle radius, m is the mass of the particle, and c is the speed of light. The power loss through SR due to parallel acceleration is a negligible fraction of this.

In a circular electron accelerator with an isometric lattice, the energy loss per particle of relativistic electrons per revolution is

$$\Delta E = C_\gamma \frac{E^4}{\rho}. \tag{2.106}$$

The world's largest circular electron accelerator, the Large Electron Positron Collider (LEP), had $E = 105$ GeV, $\rho = 3100$ m [21] so the particle energy lost per turn was 3.5 GeV or 3%. This limited the energy reach of LEP because of limitations in the available accelerating power required to keep the beam in orbit. A simple calculation shows that in order for there to be the same fractional energy loss per turn at 250 GeV (the ILC energy), the average bending radius of the dipoles would have to be 46 km. The total radius of LEP was 4 km, which is ~ 1.3 times the dipole bending radius. Assuming that the total radius of the ring scales with the bending radius, the total radius would need to be $1.3 \times 46 \sim 60$ km, or about 15 times the radius of LEP. Hence, in this regime it becomes preferable to accelerate the particles linearly. However, SR is a source of background in linear colliders and could swamp the laser-wire Compton scattered photons. The difference in the spectra of the SR and the radiation of interest being measured can

be exploited to solve this problem (Sec. 6.7).

2.5.2 Synchrotron Radiation Spectrum

The critical photon energy is [4]

$$\varepsilon_c = \hbar\omega_c = \frac{3}{2}\hbar c\frac{\gamma^3}{\rho} = \frac{\hbar C_c E^3}{\rho}, \tag{2.107}$$

where $\hbar$ is Planck's constant / 2π, ρ is the bending radius of the particle trajectory in the magnetic field, γ is the relativistic factor and $C_c = \frac{3c}{2(mc^2)^3}$ which is 3.37×10^{18} ms^{-1}GeV^{-3} for electrons. In keV, this is

$$\varepsilon_c[\text{keV}] = 2.218\frac{E^3[\text{GeV}^3]}{\rho[\text{m}]} = 0.0665E^2[\text{GeV}^2]B[\text{kG}] \tag{2.108}$$

Synchrotron radiation is emitted over a wide range of frequencies, however the spectrum falls off rapidly above the critical energy. This is the significance of the critical energy; it is a convenient mathematical scaling parameter. An approximate expression for $\omega/\omega_c >> 1$ is

$$\frac{dP}{d\omega} \sim \frac{9\sqrt{3}}{8\sqrt{2\pi}}\sqrt{\frac{\omega}{\omega_c}}e^{-\omega/\omega_c}\frac{P_\gamma}{\omega_c} \sim 0.77736\sqrt{\frac{\omega}{\omega_c}}e^{-\omega/\omega_c}\frac{P_\gamma}{\omega_c}, \tag{2.109}$$

where P is the synchrotron radiation power.

Chapter 3

ATF Extraction Line Laser-Wire

A laser-wire system was installed in the extraction line at the Accelerator Test Facility (ATF) at KEK, Japan. This chapter describes the experimental set-up and presents the results obtained.

3.1 The Accelerator Test Facility

The ATF is a damping ring test facility for the ILC (Fig. 3.1). It consists of a 1.28 GeV electron linac driven by a multi-bunch electron gun, a damping ring and an extraction line. It has produced the lowest emittance beam achieved to date. The normalised vertical emittance in the damping ring beam has been measured [22] as $\varepsilon_y^* < 2.8 \times 10^{-8}$ rad m, which is equivalent to a unnormalised or geometric emittance of $\varepsilon_y < 11$ rad pm. In the extraction line the emittance is ~ 3 times higher. A vertical beam size $\sigma_y = 5$ pm has been achieved [23]. The beam optics used for the extraction line laser-wire experiment are designed to produce a vertical beam size of $\sigma_y = 1$ μm at the laser-wire interaction point. The new test facility, ATF2 [2, 3], which is an upgrade to the existing ATF extraction line, is intended to achieve a 37 nm vertical beam at the final focus.

The bunch frequency at the ATF is 1.56 Hz and the bunch length is 17 ps.

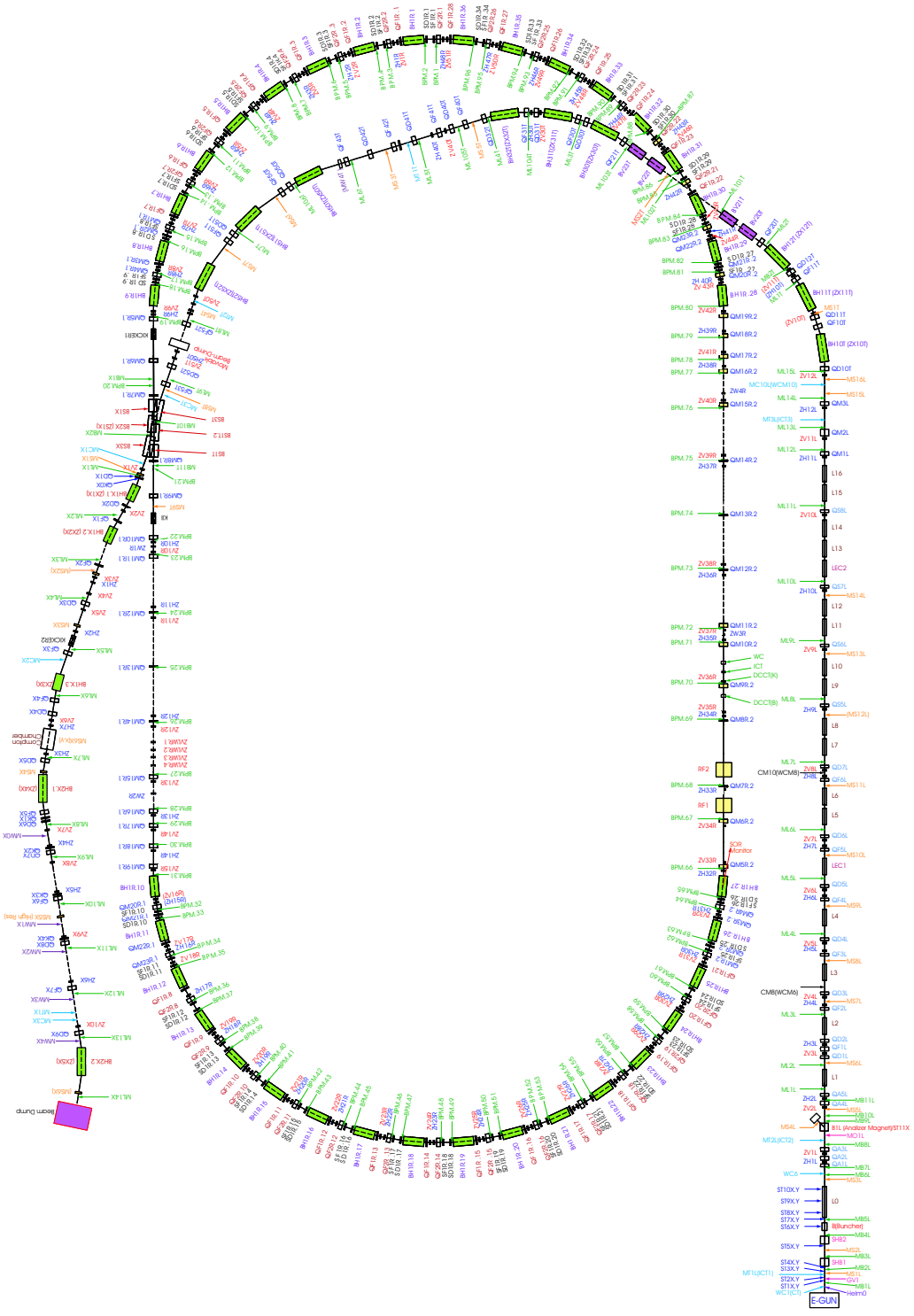

Figure 3.1: ATF. Bunches start at the gun (bottom, "E-GUN"), are accelerated by the linear accelerator (right) before going into the damping ring, which is the racetrack structure in the middle. After being damped they go into the extraction line (left) where the laser-wire is located. The location is shown more precisely in Fig. 3.2.

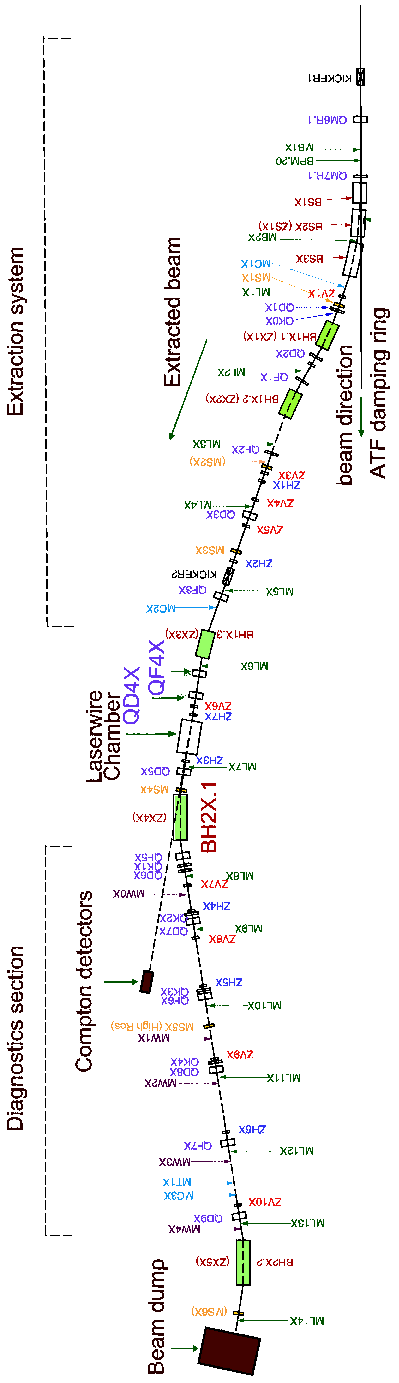

Figure 3.2: Location of the laser-wire and detector in the ATF extraction line.

3.2 Setup

3.2.1 Extraction Line Optics

Normal ATF extraction line optics are designed to achieve a minimum beam size at the end of the extraction line. The optics were modified [24] to produce a 1 μm by 20 μm beam size at the laser-wire IP. Details are shown in Tab. 3.1.

Magnet	k [1/m], Normal Optics	k[1/m], Laser-Wire Optics
QM6R	−0.7121	−0.7117
QM7R	0.3981	0.4082
QD1X	−0.04808	−0.4342
QD2X	−0.4573	−0.5164
QF1X	0.3952	0.6222
QF2X	0.1707	5.265E−5
QD3X	−0.4682	0.5884
QF3X	1.0481	1.755
QF4X	1.4875	1.773
QD4X	−0.7022	−2.321
QD5X	−0.3021	−3.179E−5
QF5X	0.1299	0.4649
QK1X	0	0
QD6X	0.2291	3.953E−5
QK2X	0	0
QD7X	−0.2273	−0.6955
QK3X	0	0
QF6X	0.28	0.3239
QK4X	0	0
QD8X	−0.37	−0.8810
QF7X	0.5	0.6069
QD9X	−0.37	−1.142

Table 3.1: Integrated magnet focusing strength k settings for normal ATF and laser wire optics. The quadrupoles can be seen in Figs. 3.1 (extraction line) and 3.2.

A MAD simulation was carried out with the laser-wire optics settings. The beta functions, dispersions and beam sizes are plotted as a function of distance, s, from the beginning of the extraction line, in Figs. 3.3–3.5. The emittances, energy and energy spread used in the simulation are show in Tab. 3.2.

ε_y [pm]	ε_x [nm]	E [GeV]	$\frac{\Delta E}{E}$
20	2	1.3	$8 \cdot 10^{-4}$

Table 3.2: Input parameters for the MAD simulation.

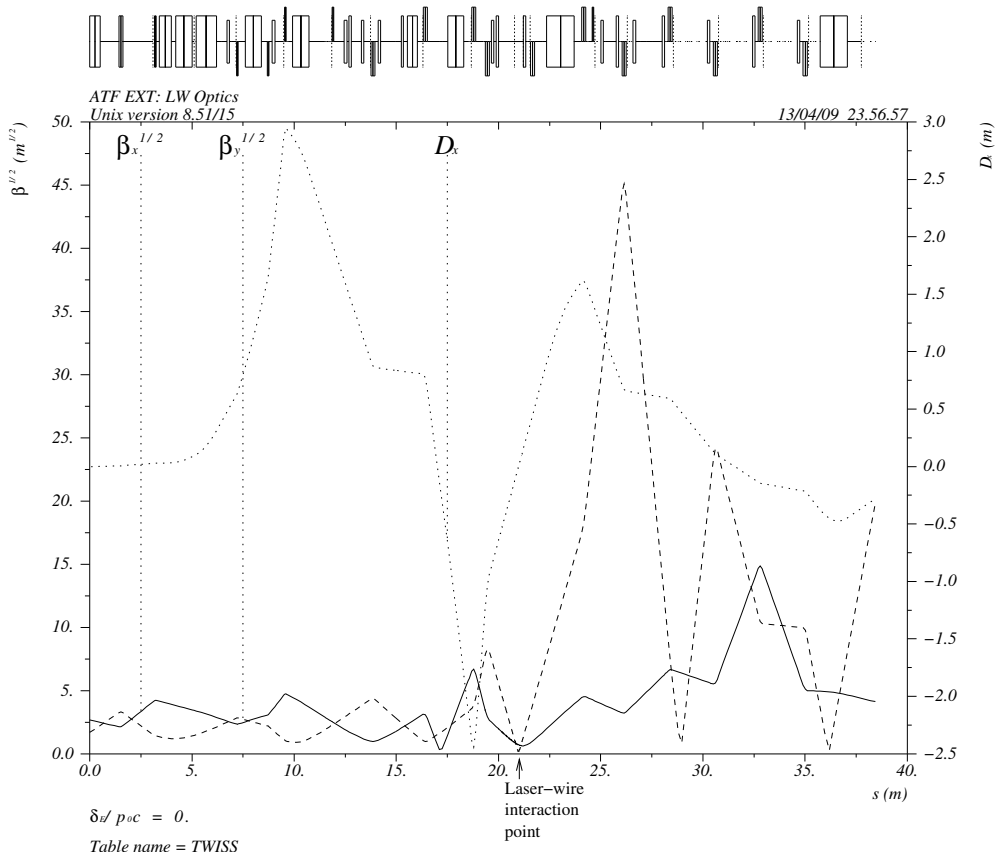

Figure 3.3: MAD simulation output showing the square root of the beta functions and the horizontal dispersion function with laser-wire optics. $k_{QD4X} = -1.516659\,\mathrm{m}^{-1}$, $k_{QF4X} = 1.574676\,\mathrm{m}^{-1}$.

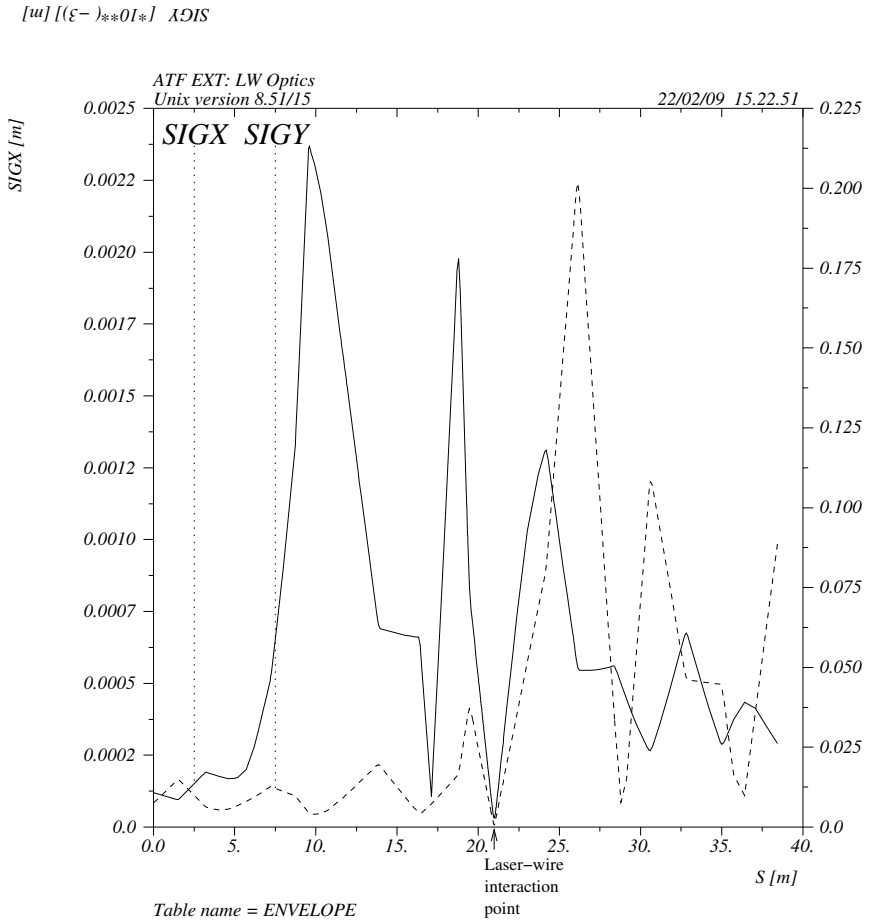

Figure 3.4: MAD simulation output showing the horizontal and vertical beam sizes along the extraction line. $k_{QD4X} = -1.516659\,\mathrm{m}^{-1}$, $k_{QF4X} = 1.574676\,\mathrm{m}^{-1}$.

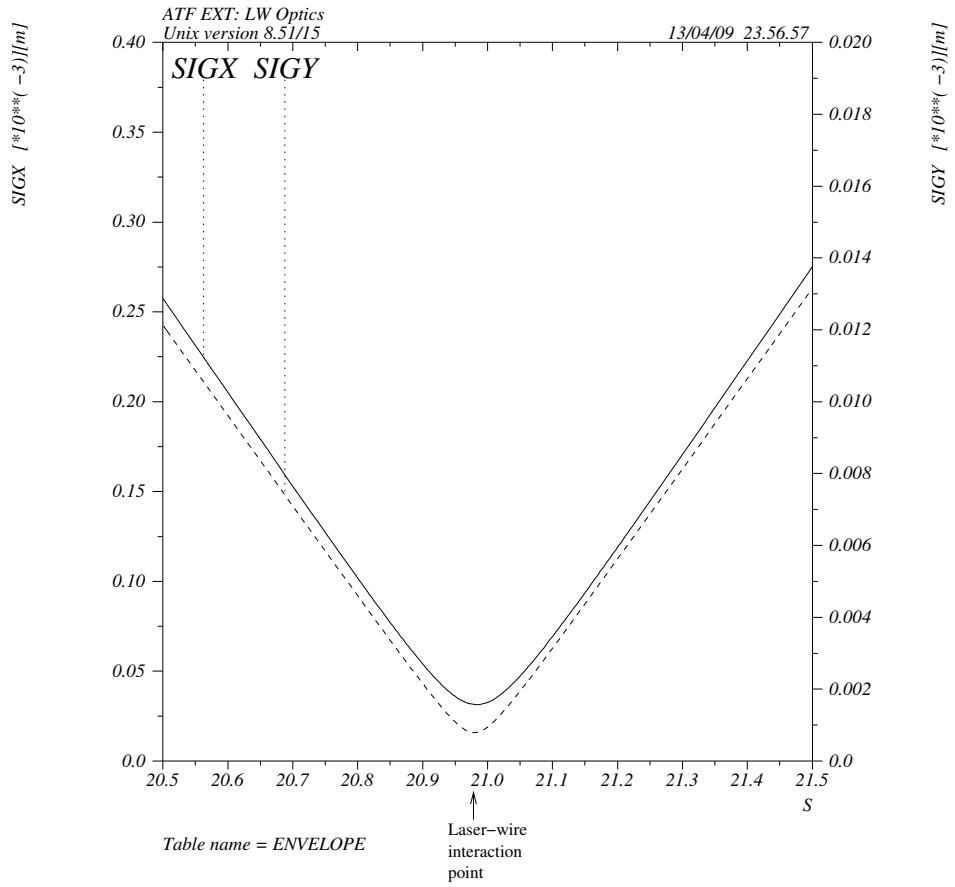

Figure 3.5: MAD simulation output showing the horizontal and vertical beam sizes around the laser-wire interaction point. This is a blow up of Fig. 3.4 around the laser-wire IP, which is 20.990 m along the extraction line. $k_{QD4X} = -1.516659\,\mathrm{m}^{-1}$, $k_{QF4X} = 1.574676\,\mathrm{m}^{-1}$.

The various parameters at the laser-wire IP with laser-wire electron beam optics, according to the simulation, are shown in Tab. 3.3. The beam sizes at the laser-wire interaction point (LWIP) can be fine tuned by adjusting two upstream quadrupoles, QD4X and QF4X. The beam parameters at the LWIP for different magnet settings are also shown in the table. Two quadrupole scanning methods were used in laser-wire tests: a double quad scan and a single quad scan. The double quad scan is designed to keep the horizontal waist at the same position as the vertical waist.

I_{QD4X} [A]	I_{QF4X} [A]	k_{QD4X} [m^{-1}]	k_{QF4X} [m^{-1}]	β_x [m]	β_y [m]	D_x [m]	σ_x [μm]	σ_y [μm]
70.06	72.74	−1.516659	1.574676	0.321	1.919	0.049	47.8	4.288
72.06	73.02	−1.559955	1.580737	0.430	0.229	0.027	36.547	2.139
74.06	72.74	−1.516659	1.574676	0.485	0.035	0.007	31.606	0.835
76.06	73.58	−1.646547	1.592860	0.544	0.340	−0.013	34.468	2.607
78.06	73.86	−1.689843	1.598921	0.607	1.145	−0.031	42.652	4.786
70.06	73.58	−1.516659	1.592860	0.321	1.026	0.207	167.6	4.529
72.06	73.58	−1.559955	1.592860	0.311	0.261	0.134	110.151	2.283
74.06	73.58	−1.516659	1.592860	0.385	0.033	0.061	56.063	0.815
76.06	73.58	−1.646547	1.592860	0.544	0.340	−0.013	34.468	2.607
78.06	73.58	−1.689843	1.592860	0.789	1.176	−0.086	79.560	4.849

Table 3.3: Beam parameters for different settings of the two quadrupoles upstream of the laser-wire interaction point according to the MAD simulation. The second table is a continuation of the first. In the upper half of each table, two quadrupoles are changed and in the lower half of each table, only one quadrupole is changed. The quadrupole settings are the same values used in the quad scans in Sec. 4.5. The emittance settings are as follows: $\varepsilon_x = 2$ nm and $\varepsilon_y = 20$ pm.

3.2.2 ATF Beam Position Monitors

The type of beam position monitors (BPMs) installed in the ATF extraction line are stripline BPMs [7]. The ATF BPMs typically have a resolution of 10 μm. There are three types of BPM

in the ATF extraction line [25]:

1. Short electrode, narrow pipe. Electrode length = 40 mm.
2. Short electrode, wide pipe. Electrode length = 40 mm.
3. Long electrode (high resolution), wide pipe. Electrode length = 120 mm.

The BPMs are named according to their position along the extraction line, ML1X to ML14X. Tab. 3.4 shows the types of BPMs installed. Their positions are shown in Fig. 3.2. Either side of the laser-wire IP are the upstream and downstream laser-wire BPMs (LWBPM1, LWBPM2). The ATF BPMs come in pairs, upstream and downstream of a quadrupole, to find the beam position in the centre of the quadrupole. The laser-wire BPMs, upstream and downstream of the laser-wire interaction point, are quoted.

Name	Type
ML1X	1
ML2X	2
ML3X	2
ML4X	2
ML5X	2
ML6X	2
LWBPM1	2
LWBPM2	2
ML7X	1
ML8X	3
ML9X	3
ML10X	3
ML11X	3
ML12X	3
ML13X	1
ML14X	1

Table 3.4: Types of BPM installed.

3.3 Laser-Wire System

The ATF extraction line laser-wire was installed in a location on the extraction line where the beam optics could be modified to produce an electron beam profile with a vertical width from $\sim 50\mu$m down to the ILC-like 1μm, with a horizontal width of 20μm. The electron beam optics that were used to achieve this spot size are described in Sec. 3.2.1.

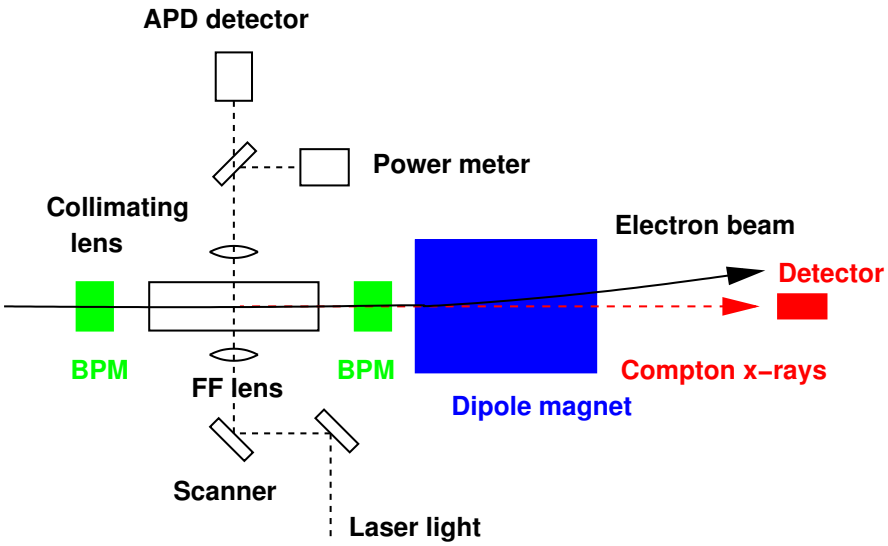

Figure 3.6: A schematic diagram of the laser-wire system.

3.3.1 Principle of Operation

laser-wires will be used to measure transverse beam sizes at future linear colliders [26] because they can achieve micron-scale precision, can withstand the power intensities of the electron beams and are non invasive so they can run continuously with machine operation. laser-wires will be needed throughout the linear collider including damping rings, ring to main linac (RTML), possibly the linac itself and the beam delivery system (BDS). R&D for such laser-wire systems is ongoing [27, 28, 29].

The principle of operation is to scan a finely focused laser beam across an electron beam. A diagram of the overlap of the two beams is shown in Fig. 3.7 [30]. The photons in the laser beam scatter from the electrons in the electron beam through the process $e^-\gamma \rightarrow e^-_C\gamma_C$ (Compton scattering). The maximum number of Compton scattered particles, at total beam overlap, for a electron bunch population of $2\cdot10^{10}$ and a pulsed laser with peak power of 10 MW and wavelength of 532 nm is $N_{det} = 4.72\cdot10^4$ [μm] $\times\eta_{det}/\sigma_c$ [8]. Here η_{det} is the detection efficiency and σ_c is the convolution of the laser and electron transverse beam sizes, which in the approximation of infinite Rayleigh range (Sec. 2.3.1) is given by $\sigma_c = \sqrt{\sigma_e^2+\sigma_l^2}$ where σ_e is the RMS electron beam size and σ_l is the RMS laser beam size. The scattering rate is proportional to the spatial overlap of the particle distributions; therefore, through knowledge of σ_l at the laser-wire interaction point, and the scattering rate as a function of relative transverse displacement, which has an RMS of σ_m, σ_e can be inferred. By making these measurements between several

different quadrupole magnets the horizontal and vertical emittance can be measured [8, 31].

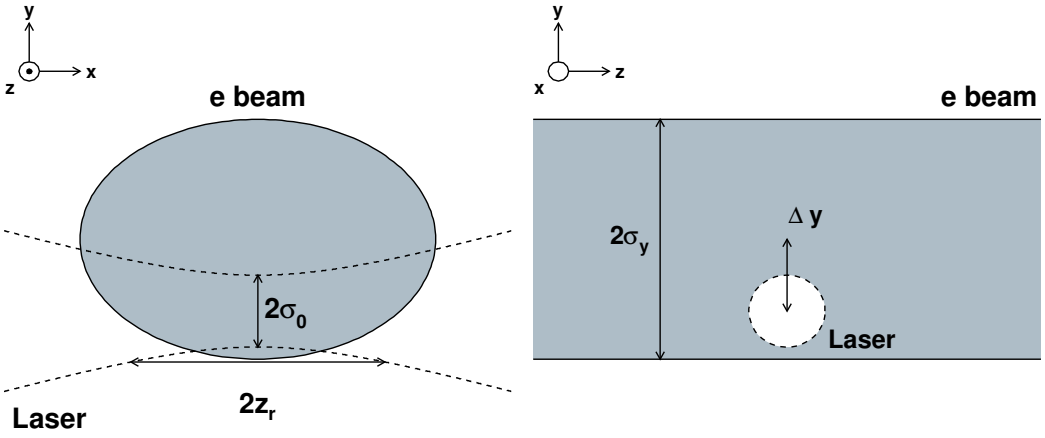

Figure 3.7: A diagram of the overlap of the laser and electron beams. On the left, the electron beam is shown travelling into the page and the laser beam travels from left to right. σ_y here is the vertical electron beam size. Δy is the displacement in y from the maximum overlap position. The dotted lines are the edges of a Gaussian laser beam converging to a waist of size σ_0 and with Rayleigh range z_r (Eq. 2.86).

A schematic diagram of a laser-wire system is shown in Fig 3.6. High energy green (532 nm) laser pulses, synchronised with the ATF electron beam pulses, are transported to the extraction line with a series of mirrors, then collimated and aligned to the accelerator. The laser light is then steered onto the final focus lens using two mirrors ("scanner" in Fig. 3.6). The angle of the laser beam on the final focus lens is controlled by tilting the final mirror. This changes the position of the laser beam relative to the electron beam. The laser beam is focused by the final focus lens onto the electron beam and the laser photons are Compton scattered with electrons in the electron beam.

Post-IP, a collimating lens recollects the laser light. A beam splitter then reflects a small fraction of the light onto a power meter. An avalanche photo-diode (APD), which is used in the collision finding process (Sec. 3.3.9) is placed behind the beam splitter. A ceramic beam dump on a translation stage in front of the APD acts as a shutter to protect the APD from high energy laser pulses.

In order to measure the scattering rate, γ_C and/or e_C^- are separated from the main beam using a downstream dipole magnet and detected using a Cerenkov detector. Most of the e_c^- are swept aside by the dipole and do not hit the detector. The FF lens is the final focus lens of the laser-wire, which will focus the laser beam down to ~ 1 μm at the laser-wire interaction point. Upstream

and downstream of the collision chamber are 10 μm resolution stripline beam position monitors (BPMs). Post-laser-wire interaction point, a collimating lens re-collimates the laser beam, which then hits a partially transmitting mirror. Most of the laser light hits a power meter for laser power normalisation. A small fraction of the light hits an avalanche photo-diode (APD). The APD is used in the initial alignment procedure to find the collision point between the electron beam and laser beam [32, 27, 33].

By plotting the change in the rate of Compton scattering as a function of the vertical separation between the two beams, δ_y, a convoluted beam profile is obtained. If the laser beam width is known this can be subtracted from the convoluted profile as described in Sec. 2.3.3 to obtain an electron beam measurement.

The laser-wire system was tested using two different final focus lenses (FF lens on Fig. 3.6). Firstly, a system was installed using a f/10 commercial final focus lens and results were obtained using this system. Secondly, a custom f/2 lens was installed and further results were obtained. The commercial lens system and features common to both systems are discussed in this chapter. The custom lens system is discussed in Chap. 4.

The main components of the laser-wire system are the laser itself, timing synchronisation control, beam position control, detectors and data acquisition, which are described in the following sections. The system is used to measure the profile of an electron beam by scanning a laser beam across it. Ordinary wire scanners cannot be used at the ILC because the luminosity of the beam is too high and a wire thin enough to measure the transverse beam profile would melt instantly. Also, wire scanners are invasive; they disturb the beam. A non-invasive method is preferable so that the ILC can keep running while emittance measurements are taken, maximising the integrated luminosity.

The ultimate aim is to measure the emittance of a small (micron scale), very high energy (500 GeV) beam (see Chapter 2). This will be done by measuring the beam profile along 3 axes at 5 positions and fitting the results to equations which depend on the electron beam optics.

3.3.2 Laser System

There are various laser technologies available including Nd:YAG, Nd:YLF and Ti:Sapphire. When background conditions are unknown a high power laser is better because it produces a stronger Compton signal. Nd:YAG was chosen because it is a glass matrix with a lasing medium

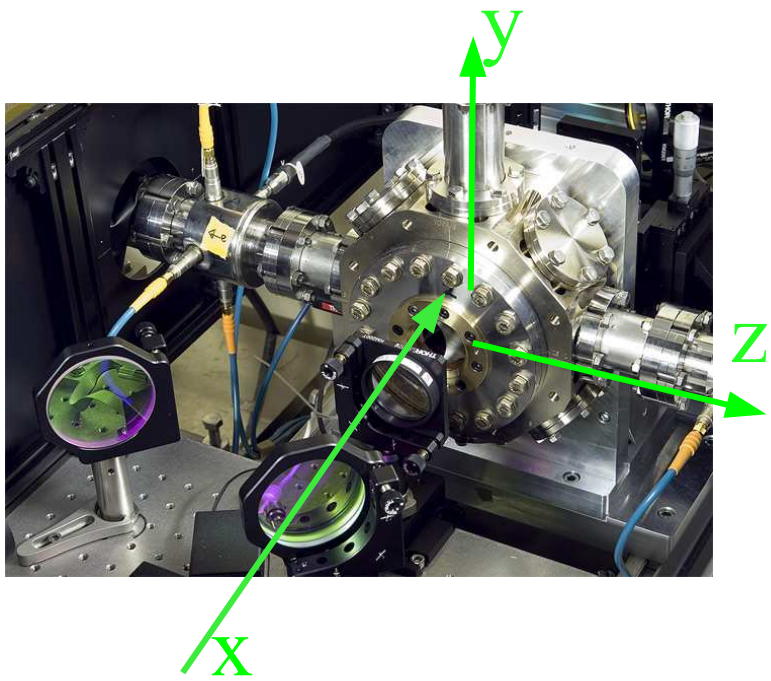

Figure 3.8: A picture of the laser-wire interaction chamber with scanner and final focus lens. The axes are defined with the direction of travel of the incoming laser as x, the direction of travel of the electron beam is z and the vertical as y.

implanted, and can take high powers, and is a mature technology with 20 years of experience behind it. Such a high power laser was readily available at KEK. There is a trade off between mode quality and laser power - the higher the power, the poorer the transverse mode quality. The pulse length of the chosen laser was well tuned to the ATF pulse length. Higher pulse power is available but not required because we did not need to go below the ATF bunch length [30].

The laser system is located on top of concrete radiation shielding blocks above the extraction line at the location shown in Fig 3.2, at a distance ~ 2 m from the beam line. The laser system has an average power output of 600 mW. It consists of three main components: a passively mode locked seed laser, a regenerative amplifier (RGA) and a linear amplifier.

Seed Laser

A neodymium vanadate (Nd:VAN) seed laser produces 20 ps, 1064 nm pulses at 357 MHz, which is frequency locked to the ATF radio frequency (RF) system. The energy of each pulse is 4 mJ. Two Pockels cells are then used to pick pulses at 1.56 Hz (the ATF bunch frequency).

Regenerative Amplifier

The pulses picked by the Pockels cells are then transported into the flash lamp pumped neodymium yttrium garnet (Nd:YAG) RGA where the pulses are amplified to 15 mJ and stretched to 150 ps. These pulses are then amplified in two single pass flash lamp pumped Nd:YAG amplifiers to 500 mJ.

Frequency Doubling Crystal

532 nm (green) light was used because the minimum theoretical spot size is limited by the wavelength of the light (Eq. 2.95). This in turn limits the smallest measurable electron beam size through Eq. 2.100.

A frequency doubling crystal was inserted in order to convert the wavelength of the light coming out of the Nd:YAG amplifiers from 1064 nm (infra red) with a pulse energy of 500 mJ to 532 nm (green) with a pulse energy of 200 mJ. The crystal material was KTP ($KTiOPO_4$), potassium titanyl phosphate, although a number of different materials can be used. Frequency doubling crystals have a nonlinear dielectric coefficient and is transparent. The physical mechanism for frequency doubling, otherwise known as second harmonic generation is as follows.

The dependence of polarisation of a dielectric upon electric electric field E may be expressed schematically as

$$P = \chi E(1 + \frac{E}{E_1} + \frac{E^2}{E_2^2} + ...) \tag{3.1}$$

Where E_1, E_2 are of the order of magnitude of atomic electric fields ($\sim 10^8$ esu). With a sinusoidally varying electric field, such as a light wave, the quadratic term in Eq. 3.1 results in a polarisation wave which is the second harmonic, or double the frequency, of the original electric field. The polarisation wave propagates through patterns of electric and magnetic polarisation. This wave emits an optical field, producing frequency doubled light [34].

The remaining infra red light was removed with the aid of a dichroic mirror. Therefore the final pulses which are used in laser-wire collisions are 150 ps long pulses of 532 nm light with an energy of 200 mJ.

3.3.3 Layout of Optical Components

The upper annotated photograph Fig. 3.9 shows the laser beam path from the laser, which is located on top of the concrete radiation shielding blocks above the extraction line, to the shutter. From here, it passes down a periscope to the extraction line. The lower photograph shows the path of the beam from the exit of the periscope, through two alignment irises, and then back around the optical table and towards the pre-IP bread board.

Fig. 3.10 shows the view from upstream of the final mirror shown on Fig 3.9 (front of picture) towards the final two mirrors, which are scanning mirrors. The vacuum chamber is in the background. The image on the left is of the post-IP bread board. In the foreground is the vacuum chamber. A beam splitter, centre of image, splits the path of the laser beam to the APD at the rear of the picture, which has the shutter in the closed position. At the rear on the orange platform is a laser power meter. The layout of the components in these images is drawn schematically in Fig. 3.6.

3.3.4 Detectors

For detecting γ_c, two detectors were installed. First, a Cerenkov detector. Secondly, a lead glass calorimeter, which was placed behind the Cerenkov detector (Fig. 3.12)

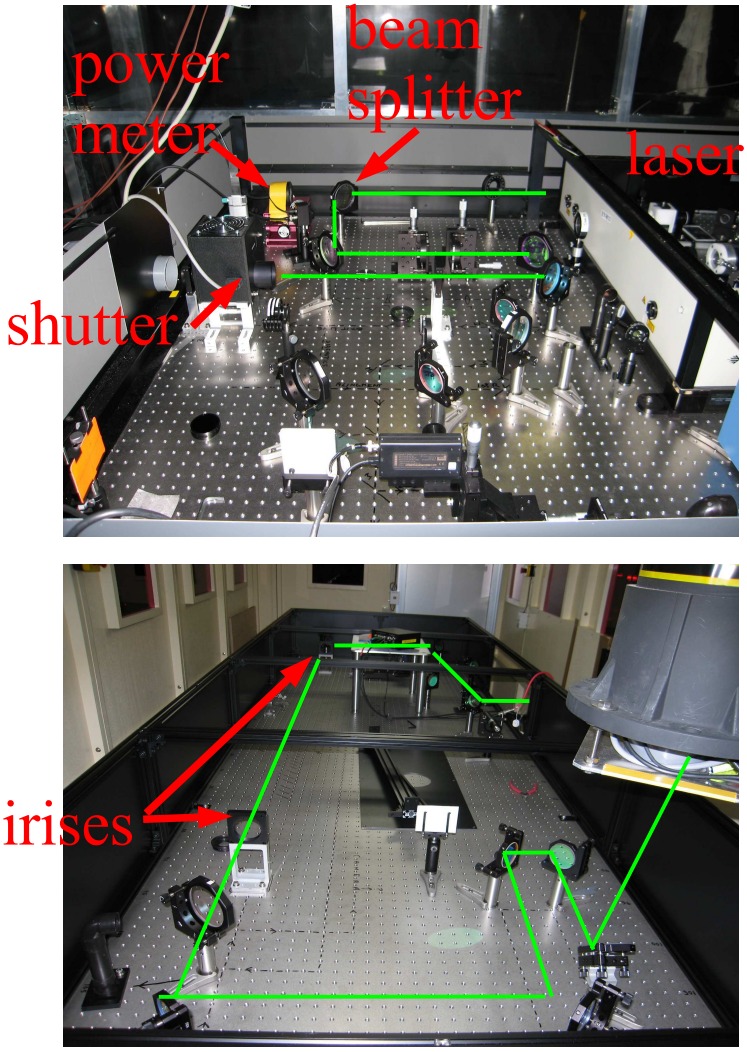

Figure 3.9: Laser beam path from the laser upstairs *(top)* to the alignment table *(bottom)*.

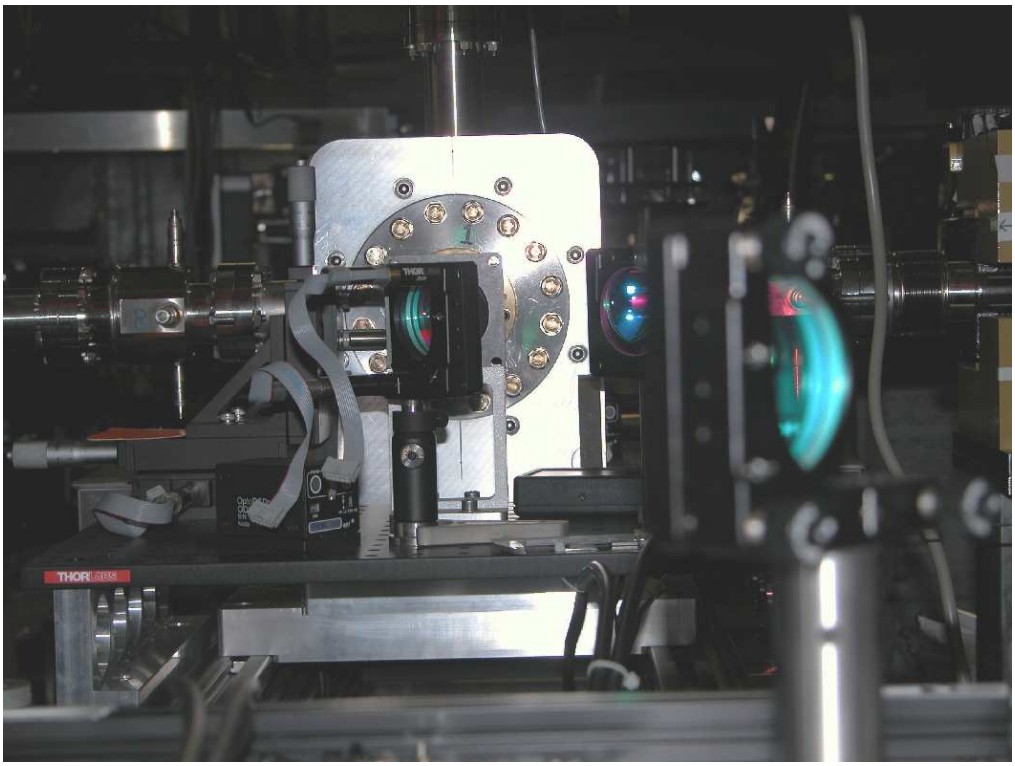

Figure 3.10: Pre-IP optical bread board.

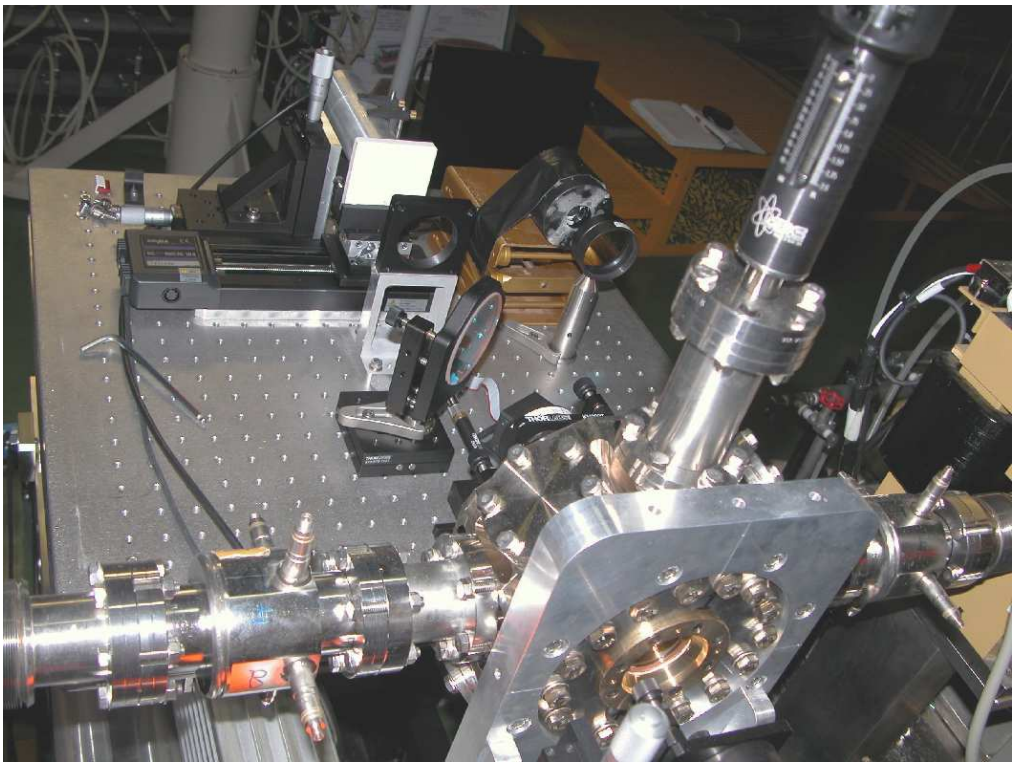

Figure 3.11: Post-IP optical bread board.

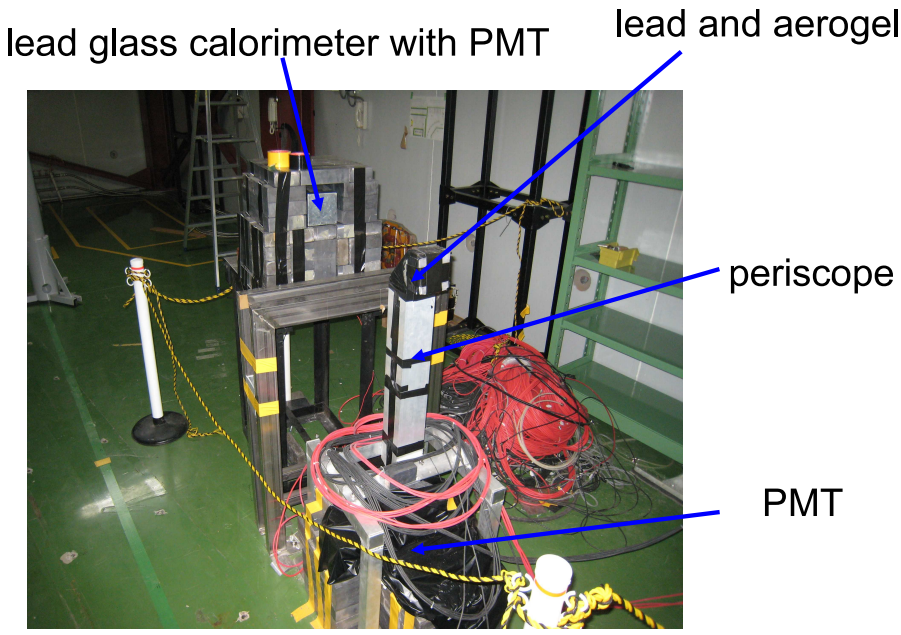

Figure 3.12: ATF laser-wire detectors. The vertical structure in the foreground is the Cerenkov detector periscope. Its photomultiplier tube is out of shot at the bottom of the periscope, completely surrounded by lead shielding. In the background, the front face of the lead glass calorimeter can be seen, with shielding around the sides. The calorimeter and shielding are placed on top of a metal support structure.

The Cerenkov detector consists of four main components:

1. A lead converter, taped to the front face a periscope, with the surface normal to the laser-wire Compton scattered photon beam.

2. A layer of SP-15 aerogel, inside the periscope behind the lead converter, again normal to the laser-wire Compton scattered photons beam.

3. The periscope, which consists of two light tight, silver coated mylar lined, square cross sectioned tubes, connected by a triangular cross sectioned piece for deflecting visible photons downwards.

4. A photomultiplier tube (PMT) at the bottom for detecting visible photons.

Compton scattered photons from the laser-wire (γ_C) hit the lead converter on the front face of the telescope normal to the surface. A fraction (Sec. 3.4) of the γ_C are converted to e^+ e^- pairs in the lead which then pass through the aerogel. As they do this, they emit Cerenkov radiation in the form of visible light. Most of these e^+ and e^- continue forwards into the calorimeter, along with the unconverted γ_c.

The Cerenkov velocity of electrons through SP-15 aerogel was calculated from the Eqs. 3.2, 3.3, from [35].

$$\gamma_t = 1/\left(1-\beta_t^2\right)^{1/2} \tag{3.2}$$

$$\beta_t\gamma_t = 1/\left(2\delta+\delta^2\right)^{1/2} \tag{3.3}$$

where $\delta = n-1$ and n is the refractive index. At the KEK extraction line the current Cerenkov detector is made of SP-15 aerogel and has a refractive index of $n = 1.015$ so the Cerenkov threshold is 2.983 MeV. The laser-wire signal has a spectrum up to 28 MeV (Fig. 6.5). The low energy background below 2.983 MeV is therefore not detected, and almost all the laser-wire signal is detected.

The visible light produced in the aerogel is reflected by a periscope into the photomultiplier tube (PMT). The PMT converts the light into a signal output.

A lead-glass calorimeter was installed behind the Cerenkov detector. The energy per pulse of the Compton scattered photons is detected in the calorimeter. The resolution of the Calorimeter is unknown. The Cerenkov detector was placed 11.4 m downstream of the interaction point. The calorimeter was 365 mm long. Its horizontal $\times$ vertical width was 113×123 mm at the front and 137×123 mm at the rear window where a photomultiplier tube was placed. The calorimeter was placed on a metal support structure and surrounded with lead shielding for background reduction (figure 3.12).

An analogue to digital converter (ADC) then digitises the signal. The data is time stamped and written to hard disk by the DAQ system, along with data from all other detectors in the system, as well as the positions of any actuators such as the DC servomotor mirror movers [36], which are the 40 nm resolution actuators that were installed in the mirror mounts and control the tilts of the mirrors.

3.3.5 Monitoring of Laser Power Output

Laser light power meters were installed in the laser hut and in the damping ring. The data from these power meters were integrated into the DAQ system such that their readings were digitised and recorded along with other data for every pulse.

3.3.6 Temperature Control and Monitoring

The laser hut is an air conditioned plastic and metal structure on thick concrete slabs above the damping ring. This environment helps keep the laser cool and protects people from radiation. Temperature fluctuations adversely affect the stability of the laser. The laser was not operating stably so in order to diagnose the problem a temperature monitoring system was installed as part of the DAQ. A system of thermocouples were installed and integrated into the DAQ system so that temperature readings were recorded with every pulse, along with all the other data collected by the system, in order to monitor any correlation between the performance of the system and temperature fluctuations. Thermocouples were placed in the following locations:

1. On the laser table
2. Near the ceiling of the laser hut
3. In the laser cooling water
4. Near the electronics racks
5. Outside the laser hut, on top of the concrete blocks

It was found that by running the system at night and starting the laser several hours before the beginning of a data taking shift in order to allow it to reach thermal equilibrium that the temperature fluctuations were minimised and the laser could operate stably. Better temperature control and/or laser stability will be required for the final ILC system.

3.3.7 Beam Position and Focus Control

The laser beam is reflected down a periscope into the damping ring where it hits a movable mirror. The mirror's vertical (electron beam y) and horizontal (electron beam z, laser beam y) angle is changed by actuator motors. The motors push the mirror mount to rotate it around an axle. The motors are controlled remotely using a computer. The beam then goes into a lens for focusing. The beam's vertical and horizontal position can be controlled by changing the angle of the laser beam on the lens.

The focusing lens is mounted on a translation stage which uses a similar actuator to move in the accelerator x (laser z, or laser propagation direction) axis. There is also a post interaction

region lens for defocusing and this too has a computer controlled actuator motor on its translation stage.

An automated scanning system was developed as part of the data acquisition system. This made data acquisition quicker, easier and more controlled. The scanning algorithm was as follows:

1. Move the laser to a starting position
2. Take N data samples
3. Move the beam by step size s
4. Repeat steps 2 and 3 until end of scan

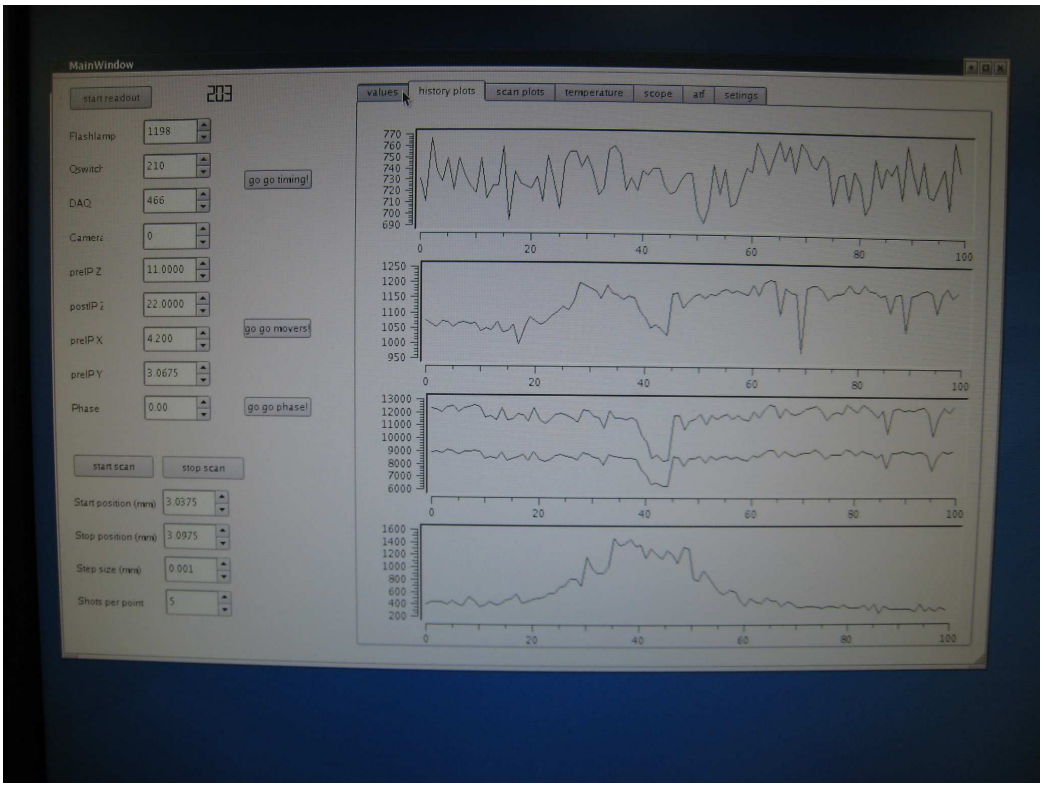

Figure 3.13: Graphical user interface of the laser-wire DAQ

A graphical user interface (GUI) was developed to provide scanning control and to give real time feedback to the user from the various sub systems. Fig. 3.13 shows a screen shot of the GUI taken near the end of a scan. In the bottom left are the scanning controls: start scan, stop

scan, start position, stop position, step size and shots per point. On the upper left hand side the basic controls for the timing systems and actuators. On the right hand side are history plots from various instruments. The bottom right is from the laserwire Cerenkov detector.

3.3.8 Scanning Geometry

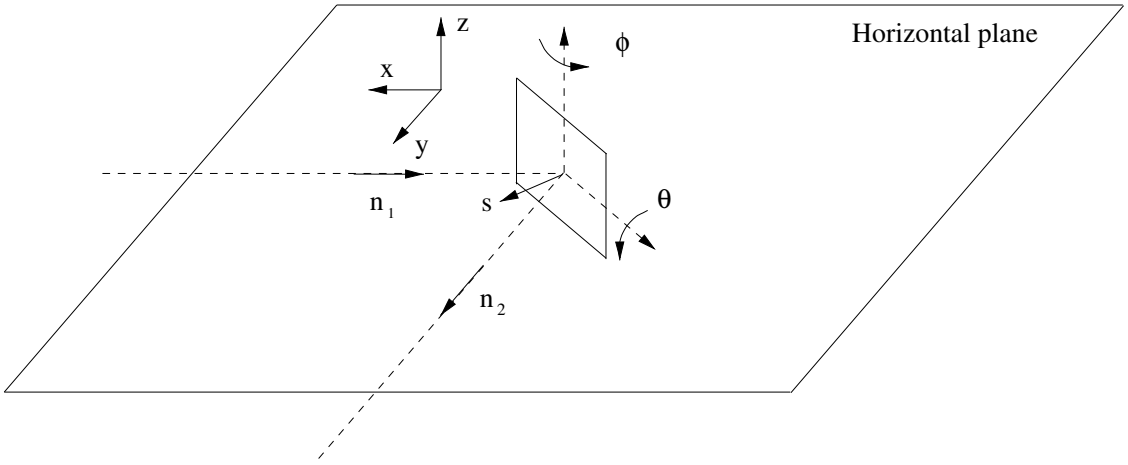

Figure 3.14: Geometry of the final scanning mirror. n_1 and n_2 are the incident and reflected laser beam vectors respectively. n_2 is incident upon the final focusing lens. The s vector is the normal to the mirror plane. The rotation angles θ and ϕ are shown. θ is the angle changed for vertical scanning and ϕ is set to $\pi/4$.

The geometry of the laser beam final scanning mirror is shown in Fig. 3.14. The vector equation for reflection is

$$\hat{n_2} = \hat{n_1} - 2(\hat{n_1} \cdot \hat{s})\hat{s} \tag{3.4}$$

$\hat{s}$ is the surface normal, $\hat{n}_1$ is the incident ray unit vector and $\hat{n}_2$ is the reflected ray. The geometry in Fig. 3.14 but with $\phi = \theta = 0$ such that the incident and reflected ray are parallel to the x axis gives

$$\hat{s} = \begin{pmatrix} 1 \\ 0 \\ 0 \end{pmatrix} \quad \hat{n}_1 = \begin{pmatrix} -1 \\ 0 \\ 0 \end{pmatrix} \tag{3.5}$$

To find the reflected ray vector after the mirror is reflected in θ and ϕ we apply the rotation transformation matrices for rotation about the z and y axes,

$$\mathbf{M}_z(\phi) = \begin{pmatrix} \cos\phi & \sin\phi & 0 \\ -\sin\phi & \cos\phi & 0 \\ 0 & 0 & 1 \end{pmatrix} \quad \mathbf{M}_y(\theta) = \begin{pmatrix} \cos\theta & 0 & \sin\theta \\ 0 & 1 & 0 \\ -\sin\theta & 0 & \cos\theta \end{pmatrix}. \tag{3.6}$$

First the mirror is rotated about ϕ and then about θ so the full transformation matrix is

$$\mathbf{M}_{yz}(\theta,\phi) = \mathbf{M}_y \cdot \mathbf{M}_z = \begin{pmatrix} \cos\theta\cos\phi & \cos\theta\sin\phi & \sin\theta \\ -\sin\phi & \cos\phi & 0 \\ -\sin\theta\cos\phi & -\sin\theta\sin\phi & \cos\theta \end{pmatrix} \tag{3.7}$$

so the vector normal to the mirror surface plane after rotation is

$$\hat{s}' = \mathbf{M}_{yz}\hat{s} = \begin{pmatrix} \cos\theta\cos\phi & \cos\theta\sin\phi & \sin\theta \\ -\sin\theta & \cos\phi & 0 \\ -\sin\theta\cos\phi & -\sin\theta\sin\phi & \cos\theta \end{pmatrix} \begin{pmatrix} 1 \\ 0 \\ 0 \end{pmatrix} = \begin{pmatrix} \cos\theta\cos\phi \\ -\sin\phi \\ -\sin\theta\cos\phi \end{pmatrix}. \tag{3.8}$$

To find $\hat{n}_2$ we apply the reflection law,

$$\hat{n}_2 = \hat{n}_1 - 2\left(\hat{n}_1.\hat{s}'\right)\hat{s}' = \begin{pmatrix} 2\cos^2\phi\cos^2\theta - 1 \\ -2\sin\phi\cos\theta\cos\phi \\ -2\sin\theta\cos\theta\cos^2\phi \end{pmatrix} \tag{3.9}$$

The component of $\hat{n}_2$ entirely in the horizontal plane is simply $\hat{n}_2$ but with the z component equal to zero.

$$\hat{n}_{2,\mathrm{hor}} = \begin{pmatrix} 2\cos^2\phi\cos^2\theta - 1 \\ -2\sin\phi\cos\theta\cos\phi \\ 0 \end{pmatrix} \tag{3.10}$$

The final lens is in the xz plane and so the angle about x of $\hat{n}_2$ incident on the final lens, α, is given by

$$\hat{n}_2 \cdot \hat{n}_{2,\mathrm{hor}} = |\hat{n}_2||\hat{n}_{2,\mathrm{hor}}|\cos\alpha \tag{3.11}$$

For $\phi = \pi/4$, which was how the final mirror and lens were arranged for scanning,

$$|\hat{n}_{2,\mathrm{hor}}| = \sqrt{\sin^4\theta + \cos^2\theta} \tag{3.12}$$

$$|\hat{n}_2| = \sqrt{\sin^4\theta + \cos^2\theta + 2\sin^2\theta\cos^2\theta} \tag{3.13}$$

$$\hat{n}_2 \cdot \hat{n}_{2,\mathrm{hor}} = \sin^4\theta + \cos^2\theta \tag{3.14}$$

so the equation describing the relationship between the angle on the final focus lens, α, and the tilt of the mirror with respect to the mirror surface plane, θ is

$$\cos\alpha = \sqrt{\frac{1-\sin^2\theta\cos^2\theta}{1+\sin^2\theta\cos^2\theta}}. \tag{3.15}$$

Plotting α as a function of theta shows that for small θ, this reduces to

$$\alpha = \sqrt{2}\theta \tag{3.16}$$

Eq. 3.16 is a very good approximation (the difference is less than 1 percent) until $\theta = 0.1$ radians where $\frac{d\alpha}{d\theta}$ begins to decrease. During collision finding, the position of the beam on the lens never deviated by more than 1 mm from the central position. The distance from the final mirror to the lens was 150 mm so this translates to an angle of $\alpha \sim 1/150 = 0.007$ rad. The difference between the exact value and the approximation at this angle is less than 0.005% so all collision data aquired with this scanning mirror setup was analysed using the linear approximation, Eq. 3.16.

3.3.9 Knife Edge and Vacuum Manipulator

A knife edge (Fig. 3.15, left) was attached to a vacuum manipulator and installed in the laser-wire vacuum chamber (Fig. 3.15, right). The knife edge was similar to that used in optical diffraction radiation (ODR) experiments [19, 18] (Sec. 2.4).

The knife edge was installed rotated 45° anticlockwise around the vertical axis (as viewed from above) from parallel to the beam line. The purpose of the knife edge was to aid in the vertical and temporal overlap of the laser and electron beam during a collision search (Sec. 3.3.9). The manipulator works using a stepper motor and moves the knife edge up and down in

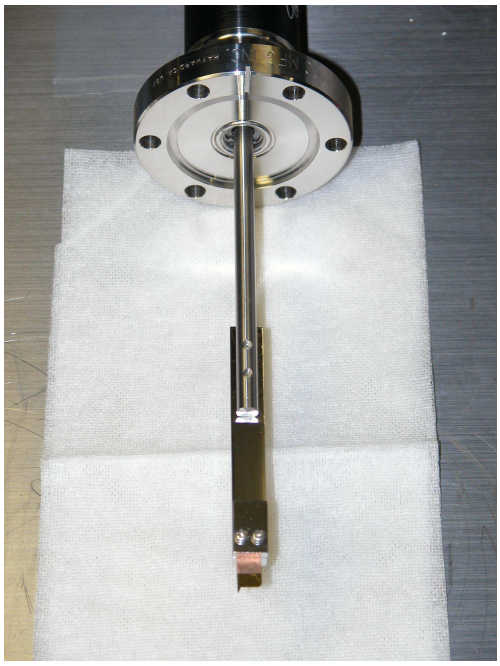

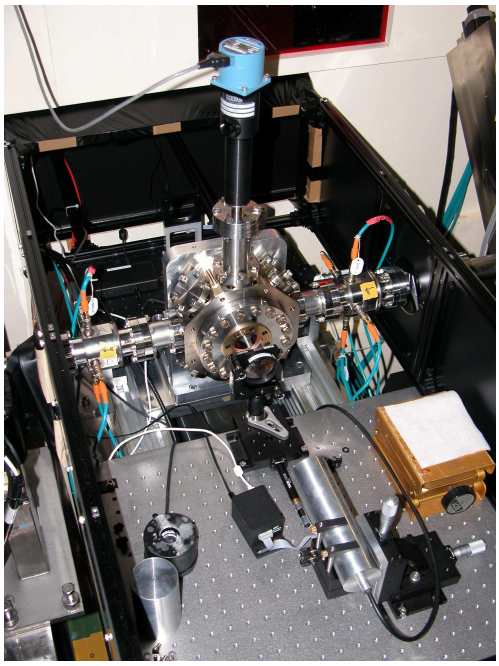

Figure 3.15: *Left:* knife edge (bottom of image) and vacuum manipulator. *Right:* vacuum chamber with knife edge and manipulator installed at the top. The picture foreground shows the post IP optics bread board with the f=100 mm re-collimating lens and the avalanche photo-diode.

steps of 1 μm so that it can be moved in and out of the beams. The position of the laser beam can be checked by moving the knife edge into the laser beam until the knife edge blocks the beam. To avoid damage to the knife edge, when checking the laser position low power laser light was used. The position of the electron beam was checked by moving the knife edge into or near the electron beam where it causes the beam to emit ODR and/or optical transition radiation (OTR) (Sec. 2.4). The low power laser, ODR and OTR photons are detected using an avalanche photo-diode on the post-IP breadboard after the re-collimating lens (Fig. 3.15 (right), Fig. 3.6).

3.3.10 Data Acquisition System

The data acquisition is built around a central program that communicates with multiple small programs in either Linux C++, Windows Visual C++ or Labview, running on either the same (Linux) machine, or on other Windows or Linux machines, and communicating via a messaging protocol based on TCP/IP. This allows communication between all the different components (accelerator, actuators, laser, digital to analogue converters) and effective data distribution. All data are collected, time stamped and stored on the central DAQ machine in a single file in ASCII format with a separate, labelled line for each component so that the data is both human readable

and easily loaded into arrays by a data analysis program. The timing of the system is controlled via a NIM pulse generated from a trigger signal from the extraction line kicker, which notifies the system of beam arrival in the extraction line. Latency and desynchronisation of recorded data does not occur because the ATF runs at only 1.5 Hz in single bunch mode, allowing the system plenty of time to complete all data collection tasks.

3.4 Simulation of laser-wire Signal

The conversion rate of γ_c and the number of γ_c reaching the detector was calculated by simulating the system in BDSIM [37] (Sec. 6.2).

Laser power normalisation

A laser power meter was installed to measure pulse by pulse laser power for normalisation purposes. In principle this could improve the scan resolution. In practice the uncertainty was dominated by other factors (see Sec. 3.5.4).

3.5 Collision Measurements

Here the collision measurements carried out with the commercial lens system are described, and results are presented.

3.5.1 Laser Scan

The laser beam is scanned vertically across the electron beam in steps in the manner described in Sec. 3.3.7. At each new position, the detector signal is recorded for some number of pulses. This signal is averaged at each position and the signal is plotted against position. σ_c is found by fitting the plot to a Gaussian (signal) plus a constant or computing the second moment.

3.5.2 Waist Scan

The laser focus position is changed by moving the lens along the laser propagation axis (Sec. 3.3.7) and at each focus position a laser scan (Sec. 3.5.1) is performed. σ_c is plotted as a function

of lens position and fitted to the laser propagation function (2.86). The minimum of this function is the lens position with the laser beam is focused on the electron beam.

3.5.3 Quad Scan

The electron beam focus position is changed by varying the current through an upstream quadrupole (QD4X) to change its focusing strength. QF4X is changed together with QD4X in order to move the horizontal axis focus position at the same rate, so that the horizontal waist is at the same position as the vertical waist. This effectively changes the electron beam size, σ_e, at the laser-wire interaction point. A laser scan is performed for each different quadrupole setting and σ_c is plotted as a function of quad current. The minimum of this curve is the location of the electron beam focus and σ_c at this location is the minimum σ_c.

3.5.4 Results and Analysis

The first ATF laser-wire data were taken in May 2006 where there was a minimum convoluted spot size of $\sigma_c = 15$ μm. The minimum measured σ_c achieved prior end of running with the commercial lens system in December 2007 was $\sigma_c = 5.5 \pm 0.1$ μm (Fig. 3.16). The fit function is a Gaussian plus a constant:

$$s(y) = Ae^{-\frac{1}{2}\frac{(y-y_0)^2}{\sigma_c}} + k, \tag{3.17}$$

Detector	A	σ_c [μm]	k
Cerenkov	0.5939 ± 0.0087	5.46 ± 0.29	0.280 ± 0.017
Calorimeter	0.3654 ± 0.0032	5.73 ± 0.38	0.339 ± 0.011

Table 3.5: Fit parameters from the fit of Eq. 3.17 to the Cerenkov and Calorimeter data in Figs. 3.16 and 3.19. A and k have the same (arbitrary) units.

where y is the laser vertical position (laser position in Fig. 3.16), y_0 is the position of the peak, A is the amplitude of the Gaussian function and k is a constant.

Laser waist scans like that in Fig. 3.17 are done first in order to focus the laser beam on the electron beam by moving the final focus lens to the minimum of the fitted curve. The quad scans show clear variation in the size (measured with the laser-wire), consistent with changing the strength of quadrupole magnets.

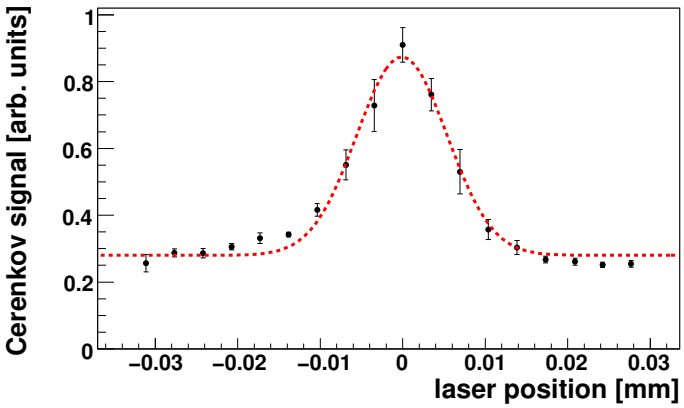

Figure 3.16: A 6 μm size vertical (y) scan fitted to a Gaussian. Each point is the average of 5 pulses. The signal is normalised to the electron beam current which was measured using a wall current monitor. The fit, red dashed line, is a constant + Gaussian.

Figure 3.17: Convolution of laser and electron beam vs. final focus lens position

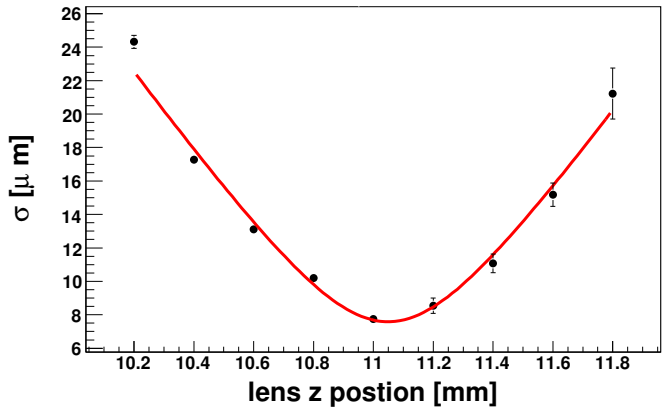

The temporal overlap of the laser pulse and the electron bunch are achieved by using an adjustable phase shifter, as described in Sec. 3.3.9. Fine tuning of this overlap can be achieved by scanning the phase and plotting the peak signal versus time delay (Fig. 3.18). The peak signal is achieved at the point of maximum overlap. The scan also shows information about the laser pulse length. A Gaussian fit gives an estimate of the pulse length but is not an exact fit. The fit results give a pulse length of 165.8 ± 0.5 ps. The fluctuations are due to fluctuations in laser and/or electron beam power.

As a cross check, a calorimeter was placed behind the Cerenkov detector so that they could simultaneously measure the laser-wire Compton scattered photons. The same collision signal

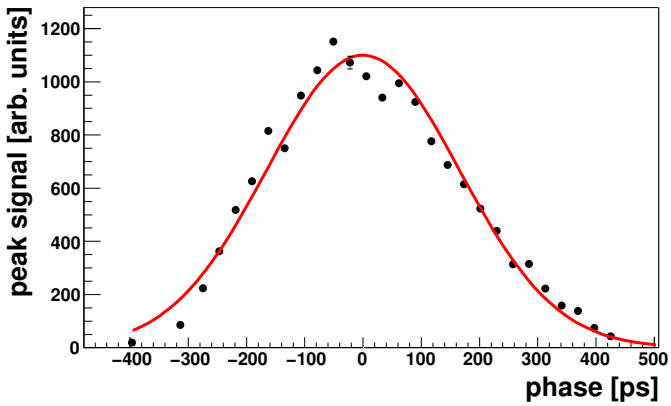

Figure 3.18: Laser and electron bunch relative peak signal vs. phase.

as collected using the Cerenkov detector and plotted in Fig. 3.16 was also detected by the calorimeter and is shown in Fig. 3.19.

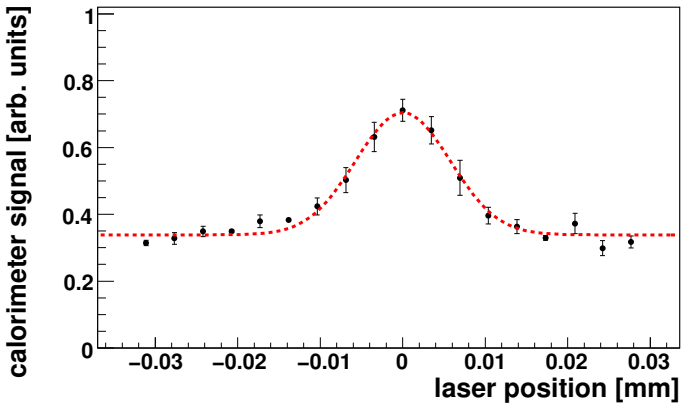

Figure 3.19: Same data as in Fig. 3.16 but measured using the calorimeter

In Figs. 3.16 and 3.19 the signal to noise ratio, defined as the amplitude of the Gaussian divided by the background level, is 0.8 for the calorimeter. For the Cerenkov detector it is 1.8. The Cerenkov detector has a low energy threshold of 2.983 MeV (Sec. 3.3.4) so it does not detect particles below this energy, which would include low energy background particles. The calorimeter measures both Compton and background particles below this threshold, so is more sensitive but suffers from greater backgrounds.

Bunch charge was measured using both a wall current monitor (WCM) and an integrating current transformer (ICT). The wall current monitor is located upstream near the laser-wire

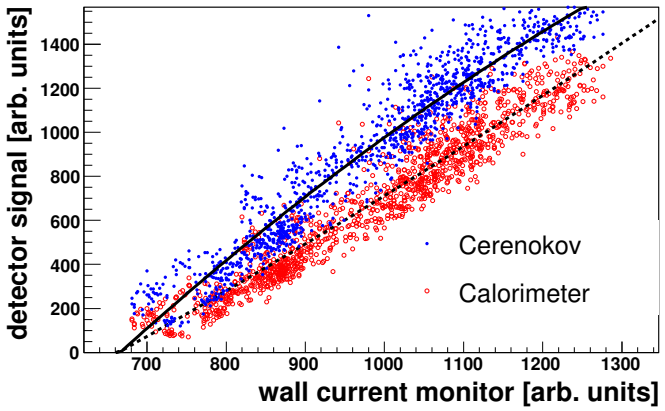

Figure 3.20: Cerenkov and calorimeter signals vs. beam charge. The intercept is far from zero due to pedestal in the wall current monitor.

interaction point (IP) and the ICT is located at the end of the extraction line near the beam dump. With the beams optimally overlapping at the laser waist, 20 minutes of data were taken. During this period the bunch charge was varied from 0.1×10^{10} to 1.4×10^{10} electrons. The response of both detectors as a function of bunch charge is shown in Fig. 3.20.

Detector.	$p_0/10^3$	p_1	$p_2/10^{-3}$
Cerenkov	-2.6 ± 0.1	4.5 ± 0.3	-1 ± 0.2
calorimeter	-1.2 ± 0.1	1.6 ± 0.3	0.3 ± 0.1

Table 3.6: Detector linearity fit for calorimeter and aerogel Cerenkov detectors.

The data were fitted to second order polynomials. The data (Tab. 3.6, Fig. 3.20) indicate that the calorimeter is slightly more linear than the Cerenkov detector [33].

The emittance of the electron beam can be measured by varying the strength of the quadrupole through a beam size minimum, as described in Sec. 2.1.9. As a test of the laser-wire's ability to measure different electron beam sizes a quad scan was performed. Here the quad current of an upstream defocusing quadrupole is changed and a vertical laser-wire scan is performed at each quad setting. The plot (Fig. 3.21) shows clear beam size variation from 54 μm down to the minimum at 6 μm. Above 54 μm the signal to noise ratio is too low to make a measurement. The fluctuations could be due to changes in electron beam position with respect to the laser beam focus position when changing the quadrupole strength; this can occur if the magnetic field in the quadrupole is not a pure quadrupole field, but contains a dipole field, or if the electron beam

is off-centre in the quadrupole. In later quad scans, such as that shown in Fig. 4.45, this was corrected for by refocusing the laser beam after each change in quadrupole strength.

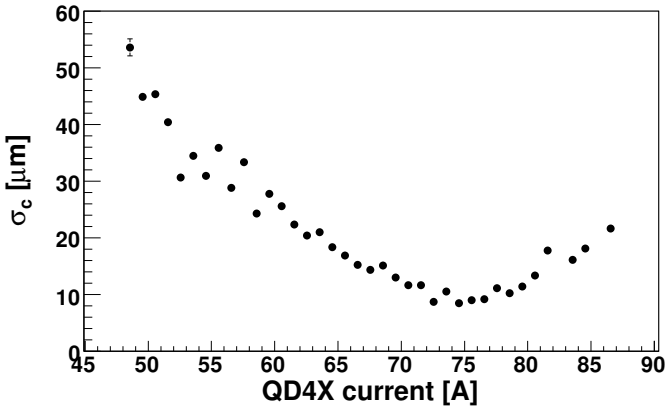

Figure 3.21: Convolution of laser and electron beam size vs. quadrupole current

Chapter 4

Upgraded Laser-Wire System

4.1 ATF Extraction Line Laser-Wire Custom f/2 lens

4.1.1 Lens Description

The laser beam has a diameter of a few millimetres. We required a focus spot size of micrometres. No commercially available lens seemed to be available that suited our needs. Therefore a custom lens was designed (Figs. 4.1 and 4.2). The lens design was started by an external consultant and was completed by members of the ATF laser-wire group.

Figure 4.1: Photograph of the custom lens.

The lens design is based on a doublet, including an aspheric element for optimum performance. All of the optical elements are made of fused silica to sustain both high laser power and

high radiation environment.

Eq. 4.1 is the equation describing an even asphere surface, like the first surface of the laser-wire lens (surface 2 in Tabs. 4.1 and 4.2).

$$z = \frac{cr^2}{1 = \sqrt{1-(1+k)c^2r^2}} + \alpha_1 r^2 + \alpha_2 r^4 + \alpha_3 r^6 + \ldots \tag{4.1}$$

Here $c = \frac{1}{R}$ where R is the radius of curvature, k is the conic constant and the α_i are the higher order terms.

The lens parameters are shown in Tabs. 4.1, 4.2.

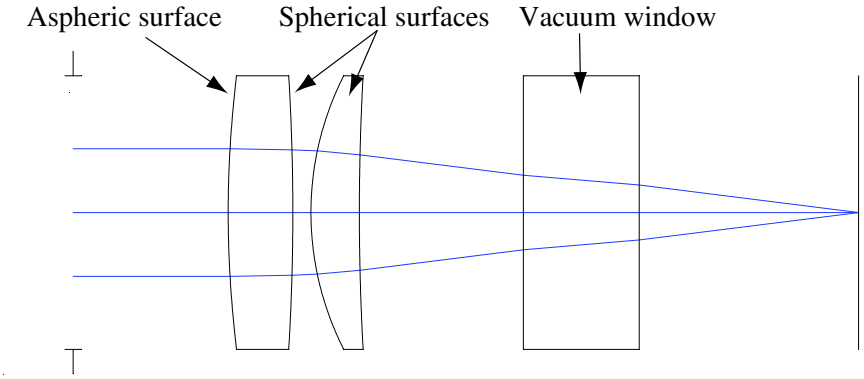

Figure 4.2: Diagram of the custom lens. The blue lines are rays traced through the system.

Surf	Type	Radius [mm]	d [mm]	Glass	Semi-Diameter [mm]
2	A	117.126106	7.093310	Silica	15.621904
3	S	−250.070725	1.987140		15.419735
4	S	33.118324	5.309160	Silica	14.999603
5	S	274.998672	17.985135		14.444878
6	S	Infinity	12.700000	Silica	9.483961
7	S	Infinity	24.075710		7.084259

Table 4.1: Custom laser-wire lens design parameters. Surface types are Even Asphere (A) and Standard (S). “d” is the distance from the previous surface. “Radius” is the radius of curvature of the surface. Semi-diameter is the semi-diameter of the aperture.

Surf	k	α_1	α_2	α_3
2	−14.455280	0	$2.160486 \cdot 10^{-7}$	$7.467086 \cdot 10^{-10}$

Table 4.2: Custom laser-wire lens design parameters. k is the conic constant and the α_i are the higher order terms in Eq. 4.1

4.1.2 Chamber Mover System

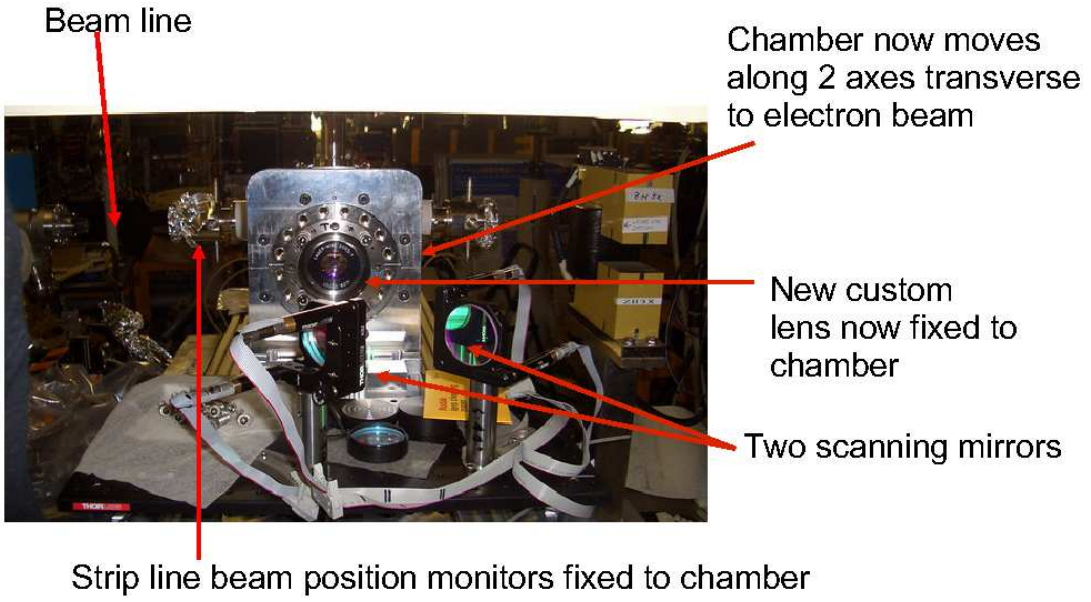

Figure 4.3: New chamber with movers

A new chamber mover system was constructed (Fig. 4.3). The strip line beam position monitors are attached to the chamber. Vacuum bellows were inserted between the vacuum chamber/BPM system to allow the vacuum chamber to move in the horizontal and vertical directions perpendicular to the beam line. Powerful stepper motors were installed to move the chamber horizontally and vertically. The purpose of the system was to enable translation of a new final focus lens which, due to its short focal range, needed to be mounted directly onto the vacuum chamber. This also made it possible to scan using a perpendicular laser beam kept centred on the lens (Sec. 4.1.3). This method of scanning, if successful, will remove the optical distortions associated with with light entering the lens off axis or off centre, keeping the laser spot size and shape constant over long range scans.

Encoders were used to monitor the position of the chamber to within 0.1 μm. The encoder readout was fed back to the control software and a variable velocity feedback loop was used to move the chamber quickly and accurately to any position. Limit switches were used to prevent the chamber from crashing into the end stop. The motor controller software was precompiled and loaded via USB onto the controller box. Control of the box was carried out via a serial connection using a communications protocol. The protocol was programmed into the DAQ

system so that the chamber mover could be controlled by the operator via the GUI front end (Fig. 3.13), including automated scanning.

4.1.3 Dual mirror scanning system

The dual mirror scanning system consists of two mirrors rotating simultaneously to translate a laser beam whilst keeping it parallel to the electron beam. The chamber mover is moved the same distance as the laser beam to keep the perpendicular laser beam in the centre of the final focus lens.

4.2 Types of Measurements Performed on Custom Lens System

Measurements performed on this system fall into three main categories:

1. Measurements of the state of the laser beam and characteristics of the lens using cameras, knife edges, power meters etc. (Sec. 4.3).
2. A continuation of, and additional measurements on the state of the electron beam using wire scanners, beam position monitors, current monitors etc. (Sec. 4.4).
3. Measurements of the interaction between the laser and electron beam under varying conditions (collision measurements) (Sec. 4.5).

These three groups of measurements (often performed during the same shift period) were analysed.

4.3 Laser Beam and Lens Measurements and Simulations

4.3.1 Simulation of Lens M^2

The lens was simulated [30] using Zemax version 12 physical optics propagation to find the M^2 of the lens as a function of input beam size (Figs. 4.4 and 4.5 [30]) using a $M^2 = 1$ laser. Physical optics propagation uses diffraction calculations to propagate a wavefront through and optical system surface by surface, accounting for the coherent nature of the light. The wavefront is modelled using an array of points containing complex amplitude information about the beam.

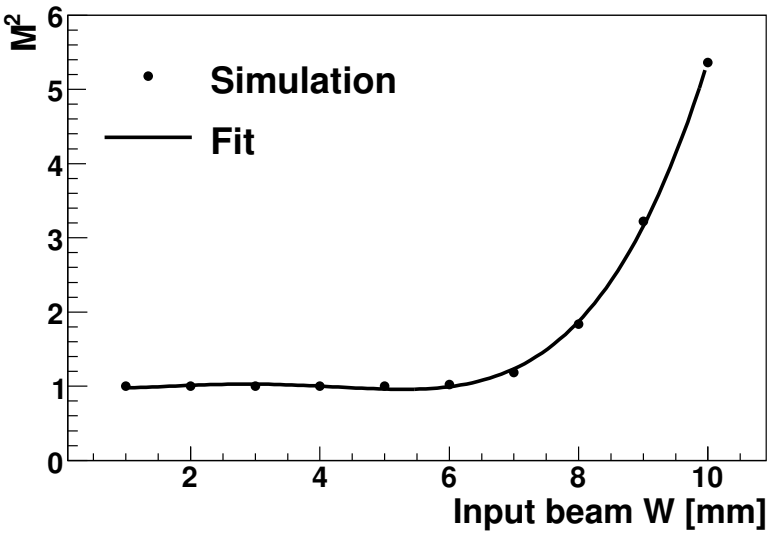

Figure 4.4: Results of Zemax simulation of the M^2 after propagating through the custom lens of a laser beam with input $M^2 = 1$ for different input beam sizes. The resulting M^2 is called *lens* M^2 in the text.

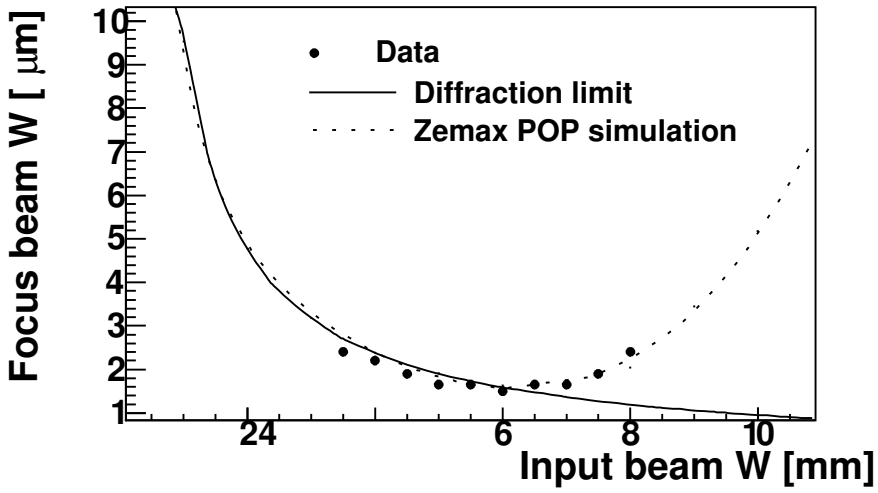

Figure 4.5: Results of Zemax simulation of the W_0 of the custom lens for different input beam sizes. "POP" stands for "physical optics propagation". Experimental data are also shown. The input laser has $M^2 = 1$.

The experimental data in Fig. 4.5 is from [38]. The lens M^2 is due to spherical aberrations when the lens is over filled and goes as the fourth power of input beam size. The simulation data were fitted to a fourth order polynomial (Eq. 4.2). The data and fit are shown in Fig 4.4, and the fit results are in Tab. 4.3.

$$M^2 = p_0 + p_1 W + p_2 W^2 + p_3 W^3 + p_4 W^4 \tag{4.2}$$

	p_0	p_1	p_2	p_3	p_4
value	1	$-9.181 \cdot 10^{-2}$	$9.257 \cdot 10^{-2}$	$-2.6338 \cdot 10^{-2}$	$2.2382 \cdot 10^{-3}$
error	0	$5 \cdot 10^{-5}$	$3 \cdot 10^{-5}$	$4 \cdot 10^{-6}$	$2 \cdot 10^{-7}$

Table 4.3: Results of fit of Eq. 4.2 to the lens simulation data, Fig. 4.4

This result agrees with IP laser profile measurements and laser waist collision measurements (see Secs. 4.3.7 and 4.5.2).

4.3.2 Profiling of Laser System

The propagation of the laser was investigated using a WinCamD camera [39]. This was done in order to better understand the physics of the propagation of the laser and how this relates to the expected beam size at the LWIP and how the data from collision between the laser beam and electron beam could be interpreted in order to extract information about the electron beam. It also helped to gain a better understanding of how the spot size could be improved.

The theory of laser propagation and laser-wire Compton rates was presented in Secs. 2.3.1 and 2.3.3. M^2 was measured in the following way. The setup is shown in Fig. 4.6. The camera was placed on a translation stage with a range of 500 mm. A lens with a focal length of 1118 mm was put in the path of the laser beam after a beam splitter and just before the camera on the translation stage and images of the laser beam profile were taken at intervals of 10 mm more than 40 mm from the waist and at intervals of 5 mm within 40 mm of the laser waist. The interval between profile positions was halved near the waist because the rate of change of beam size is greater there. The beam splitter was used to enable profile measurements to be taken while the laser was running at full power. Profile measurements were also taken without the splitter at low power. The RMS of 64 images was used to produce two data points at each camera position: one for each orthogonal axis, u and v (Figs. 4.7, 4.8, 4.11). Each data point in the laser profile

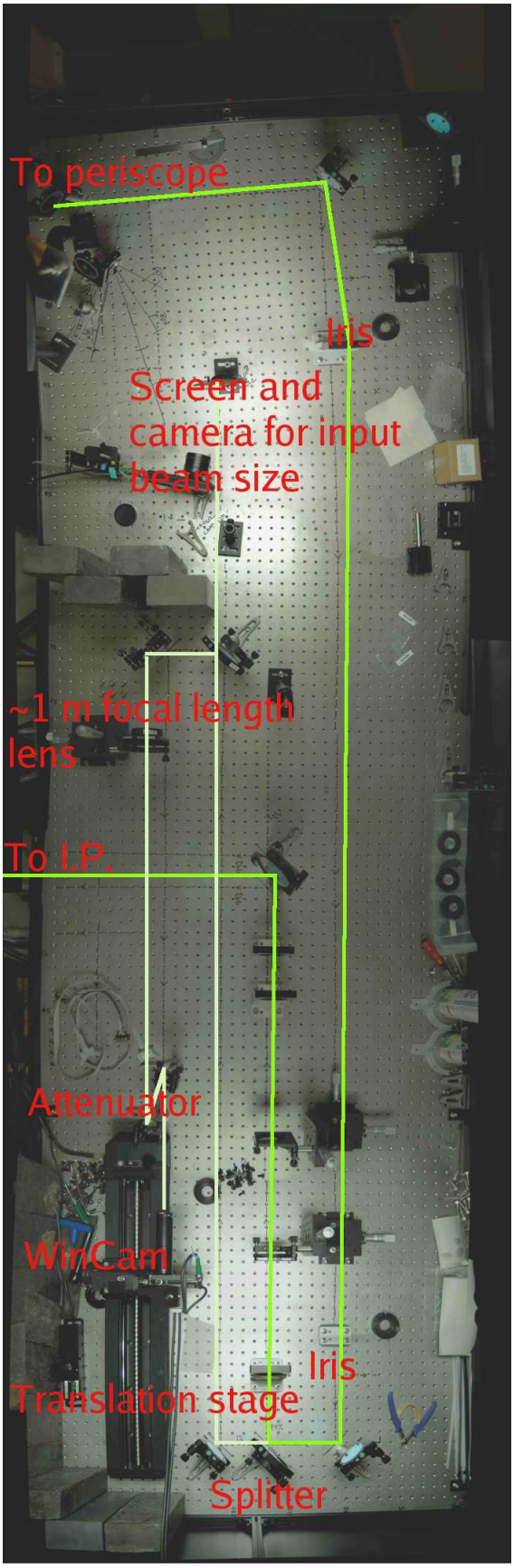

Figure 4.6: Photograph of the "downstairs" optical table. The spacing between the holes is 1.25 cm.

plots is an average of the 64 different images. As will be shown, there was astigmatism present in the beam and so the beam propagated differently in the two axes and as a result the location of the laser waist, Z_0, was different for the two different axes. The astigmatism was increased by the splitter, increasing the distance between the two foci (compare Fig. 4.7 and Fig. 4.8). Once all the data had been taken the images were analysed using a Labview implementation of the camera's software libraries. There was one file for each camera position, containing 64 images. The software loaded each file in turn, averaged the data and wrote to an ASCII file along with the stage position. These ASCII files were analysed, plotted and fitted using Root. Each laser axis was fitted to the laser propagation function, Eq. 2.86.

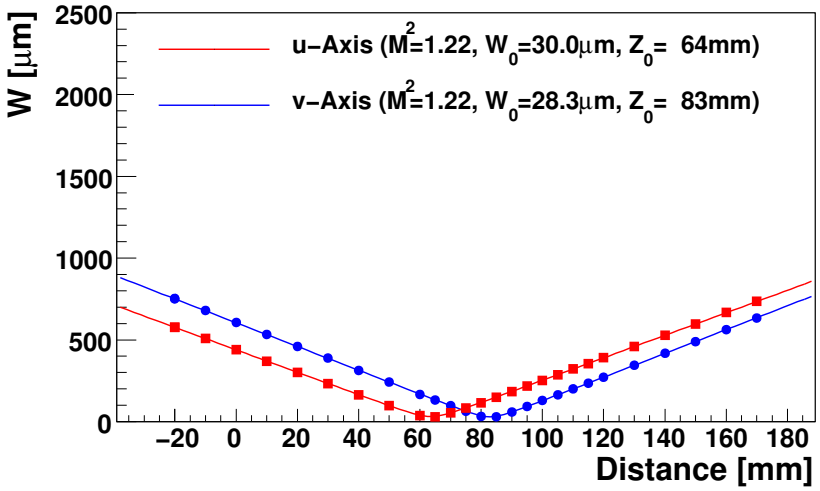

Figure 4.7: A profile measurement using a continuous wave (CW) laser with the layout the same as for the measurements taken during the shift. Red = *u*-axis, blue = *v*-axis.

The same measurement was performed with the pulsed laser, which is the laser used for laser-wire operation (Fig. 4.11). The M^2 of the pulsed laser is shown to be ~ 2, whereas for the CW laser it is ~ 1. The data do not fit as well to Eq. 2.86. This is probably due to the fact that the pulsed laser is generally astigmatic (Sec. 4.3.4) instead of simply astigmatic, which means that Eq. 2.86 is a somewhat simplistic model of the pulsed laser's propagation. It may also be due to the fact that the pulsed laser's image profile is more complicated and less Gaussian than the CW laser's (compare Figs. 4.9, 4.10).

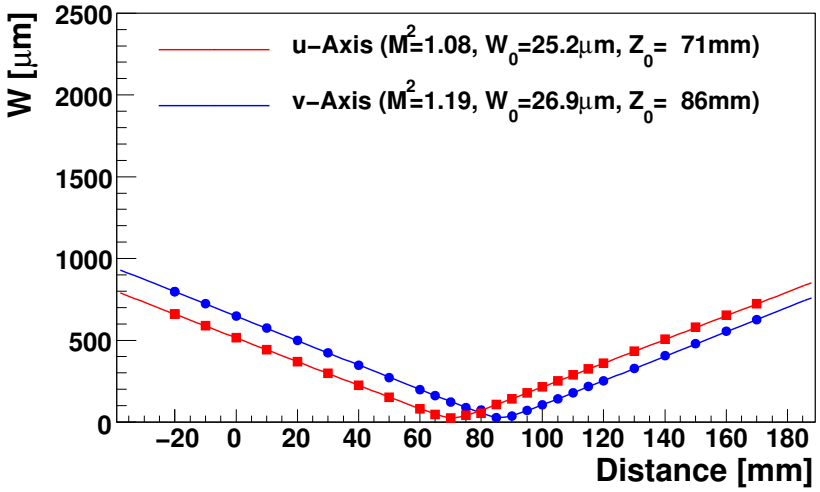

Figure 4.8: A profile measurement using a continuous wave (CW) laser. In this case, no splitter was used.

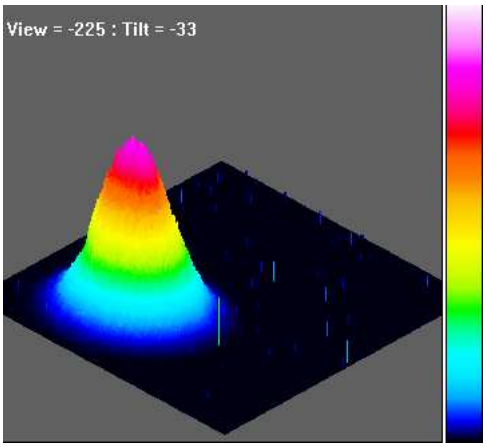

Figure 4.9: An image of the CW laser profile with the camera stage at -50 mm. The vertical axis is intensity.

	CW laser	CW laser, no splitter	Pulsed laser, no splitter
M_u^2	1.2209 ± 0.0002	1.1930 ± 0.0001	2.07 ± 0.02
M_v^2	1.2177 ± 0.0002	1.0848 ± 0.0002	2.116 ± 0.001
$W_{0,u}$ [μm]	29.998 ± 0.005	25.173 ± 0.008	40.5 ± 0.4
$W_{0,v}$ [μm]	28.289 ± 0.006	26.87 ± 0.03	39.178 ± 0.008
$Z_{0,u}$ [mm]	63.6 ± 0.5	70.7 ± 0.5	86.1 ± 0.5
$Z_{0,v}$ [mm]	82.9 ± 0.5	86.2 ± 0.5	104.1 ± 0.5

Table 4.4: M^2 measurements on the CW and pulsed lasers (Figs. 4.8 4.11 and 4.7). The errors are statistical errors.

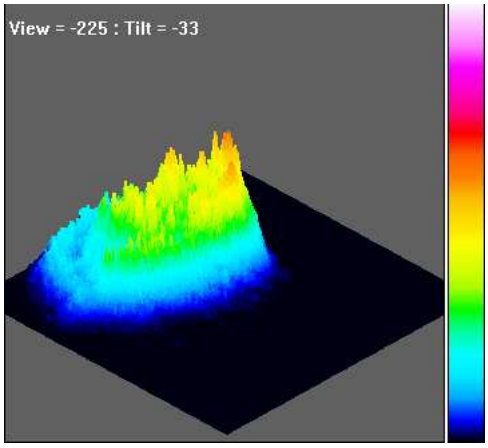

Figure 4.10: An image of the pulsed laser profile with the camera stage at -50 mm. Vertical axis is intensity.

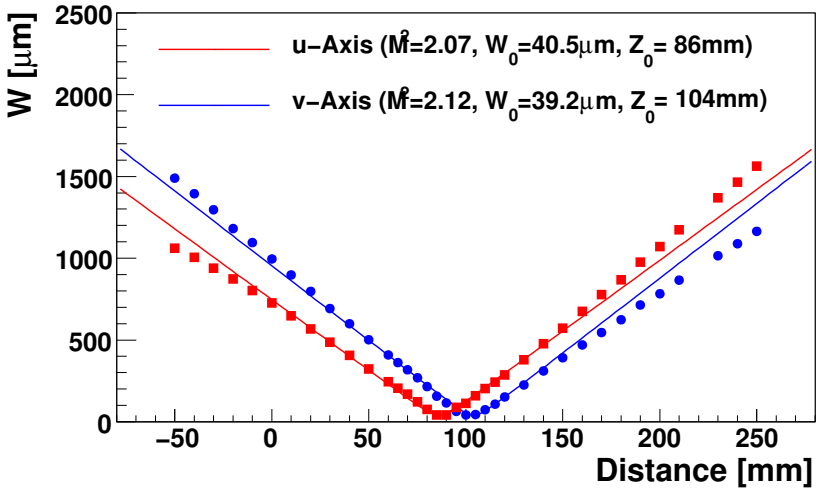

Figure 4.11: A profile measurement of the pulsed laser. In this case, no splitter was used.

4.3.3 Ellipticity

Ellipticity, ε, is defined as the ratio of the minor and major widths:

$$\varepsilon = W_{\mathrm{maj}}/W_{\mathrm{min}} \tag{4.3}$$

The error, therefore, is

$$\varepsilon\sqrt{\left(\frac{\delta W_{\mathrm{maj}}}{W_{\mathrm{maj}}}\right)^2+\left(\frac{\delta W_{\mathrm{min}}}{W_{\mathrm{min}}}\right)^2} \tag{4.4}$$

This equation determines the sizes of the error bars in Fig. 4.12. A larger error in the beam size measurement in one or both axes produces a larger error in ε.

ε has a maximum of 1, for a circular beam, and gets smaller as the beam becomes more elliptical. As the beam is astigmatic, the beam is closer to zero at the two foci and is closer to 1 at the point midway between the two foci (Fig. 4.12). Therefore, the ellipticity has two local minima at the $Z_{0,u}$ and $Z_{0,v}$ and a local maximum midway between these two points, where the ellipticity peaks at about 0.74. Because the beam is generally astigmatic, as will be shown in Sec. 4.3.4, the beam profile never becomes fully circular.

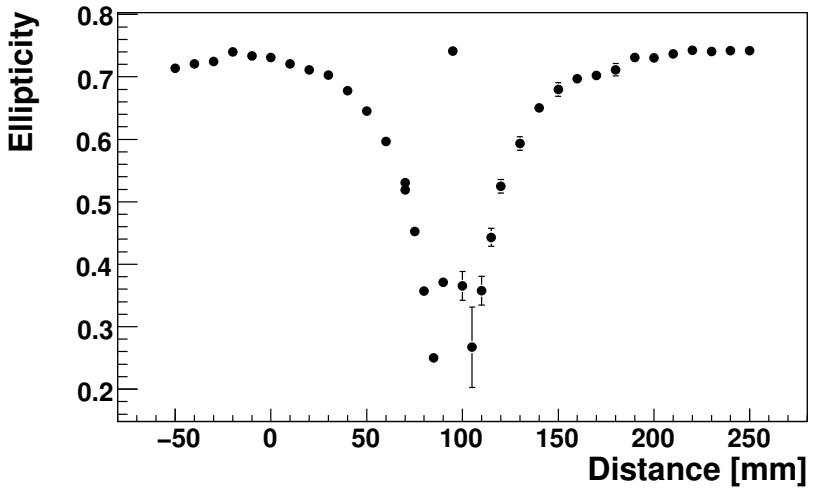

Figure 4.12: Ellipticity of the pulsed laser as a function of propagation distance z.

4.3.4 Effect of General Astigmatism on the Principle Beam Radii, w_u and w_v

A change in orientation was observed in the intensity ellipse as a function of propagation distance z, as shown in Fig. 4.13. The uncertainties are estimated from the RMS spread of the 64 images used at each point.

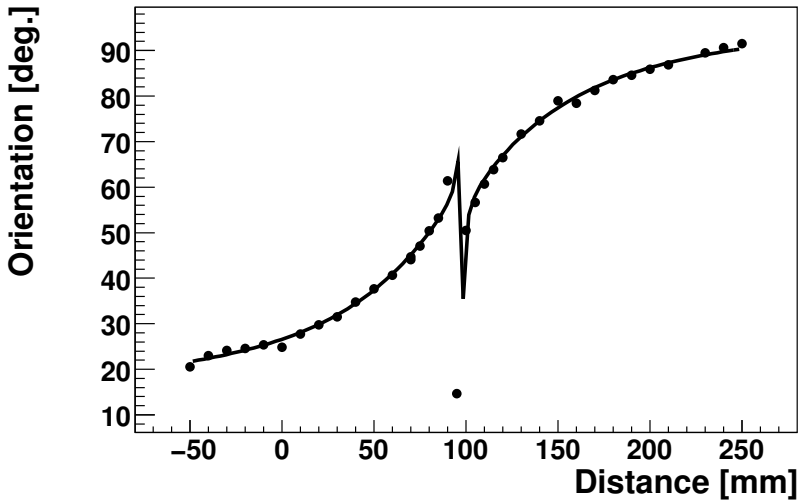

Figure 4.13: Orientation of the pulsed laser as a function of propagation distance z.

This indicates a general astigmatism, where the rotation angle of the intensity and phase ellipses is a complex number $\varphi = \beta + \alpha i$ [40].

General astigmatism results from the passage of Gaussian beam through non-orthogonal systems, such as a sequence of two or more astigmatic lenses with oblique orientations. This causes the beam to have constant intensity ellipses and constant phase ellipses oriented at an oblique angle with respect to each other. The orientation of the ellipses changes along the propagation path [40].

The orientation of the intensity ellipse is given by

$$\tan 2\phi_\omega = [(\rho_1 - \rho_2)/(\omega_1 - \omega_2)] \tanh 2\alpha. \tag{4.5}$$

Here, ϕ_ω is the orientation angle of the intensity ellipse, and

$$\omega_i(z) = \frac{p_i}{z_i^2 + p_i^2}, \tag{4.6}$$

$$\rho_i(z) = \frac{z_i}{z_i^2 + p_i^2}, \tag{4.7}$$

where the indices denote the orthogonal axes u and v in the x-y plane. p_i is twice the Rayleigh length and $z_i = z - z_{0i}$. For simply astigmatic beams z_{0i} is interpreted as the position of the waist of axis i, but for generally astigmatic beams this physical interpretation no longer holds.

Eq. 4.5 was written in terms of ϕ, the constant angle β was added and the resulting function was fit to the orientation ϕ_ω as a function of z (Fig. 4.13). The results of the fit are shown in Tab. 4.5.

α [rad.]	β [rad.]	z_{0u} [mm]	z_{0v} [mm]	p_u [mm]	p_v [mm]
0.0861 ± 0.0004	57.67 ± 0.06	93.5 ± 0.1	101.99 ± 0.06	4.93 ± 0.02	5.03 ± 0.02

Table 4.5: Results of the orientation fit. The fit function is Eq. 4.5 and the data points and fit function are plotted in Fig. 4.13.

The principle beam radii are given by [40]

$$\frac{\lambda}{\pi w_{u,v}^2} = \frac{1}{2}\left\{\omega_1 + \omega_2 \pm \left[(\omega_1 - \omega_2)^2 \cosh^2 2\alpha + (\rho_1 - \rho_2)^2 \sinh^2 2\alpha\right]^{\frac{1}{2}}\right\} \tag{4.8}$$

where λ is the wavelength of the light. The $\pm$ sign in Eq. 4.8 is positive for the u axis and negative for the v axis.

For the value of α in Tab. 4.5, $\cosh^2 2\alpha = 1.03$ and $\sinh^2 2\alpha = 2.99 \cdot 10^{-2}$. The z_{0i} are close to the observed waists (Tab. 4.5, Fig. 4.11) and $\sinh^2 2\alpha$ is small compared to $\cosh^2 2\alpha$, so we can approximate the laser propagation as simply astigmatic.

4.3.5 Laser Beam Position Stability

The laser beam position stability affects the resolution of the laser-wire because the beam size measurements depend upon the separation between the laser beam and the electron beam. The more the laser beam moves around, the more uncertain this displacement becomes.

The laser position stability was measured using a WinCamD at 100 mm from the laser. 5870 pulses were taken and the standard deviation of the centroid was found to be 29 μm. The distance from the laser to the camera is 13 m. If we assume the light originates from a point source at the exit of the laser then standard deviation of the angle is $2.2 \cdot 10^{-6}$ rad. With the 56 mm focal length f/2 lens this corresponds to a standard deviation in the position of 0.12 μm.

4.3.6 Input Laser Beam Size

From the input beam size on the lens, the M^2 and general astigmatism measurements, the σ_{lw} can be determined.

The input beam size was measured by putting a sheet with centimetre spaced markings the same distance from the laser exit port as the final focus lens position (screen and camera for input beam size measurement in Fig. 4.6). The positions of the markings were estimated to be accurate to within about 3% and this was the dominant source of error. The WinCamD camera was pointed at the sheet. The camera was then calibrated using the centimetre markings on the sheet by measuring the intensity along the line, and measuring the distance between the dips in intensity caused by the markings on the sheet. The markings were aligned with the camera's horizontal and vertical axes to ensure correct orientation of the sheet.

The laser beam was then fired at the piece of paper and W was measured by calculating the centroid, calculating the rotation (see Sec. 4.3.7), and calculating the second moment of intensity in the major and minor axes.

The results of the input beam size measurements are shown in Tab. 4.6.

Laser	$W_{\text{in,major}}$ [mm]	$W_{\text{in,minor}}$ [mm]	η_{in}	ϕ_{in} [deg.]
CW	9.2 $\pm$0.3	9.0 $\pm$0.3	0.98	$-$13.9
Pulsed	10.1 $\pm$0.3	9.1 $\pm$0.3	0.88	$-$75.3

Table 4.6: Input laser beam sizes (W_{in}), ellipticities, (η_{in}), and rotation angles (ϕ_{in}).

4.3.7 IP Profile Measurements

Prior to dismantling the laser-wire system at the end of ATF operations, in preparation for the upgrade to ATF2, the downstream side of the vacuum chamber was removed and laser beam measurements were performed near the focus using the BeamMapC [39] knife edge profiler. An image near the focus is shown in Fig. 4.14. A CW laser was set up with a lens input beam size of ~ 9 mm. The beam was aligned centrally on the horizontal axis following the normal procedure.

As the BeamMapC is a knife edge scanner it can only profile the beam in two orthogonal planes. These planes were set to 45° from the horizontal. The angle makes little difference to the measurements because the CW laser is effectively stigmatic; its ellipticity after propagating ~ 11 m from the laser exit port is greater than $8.7/9.5 = 0.92$ (from Tab. 4.6).

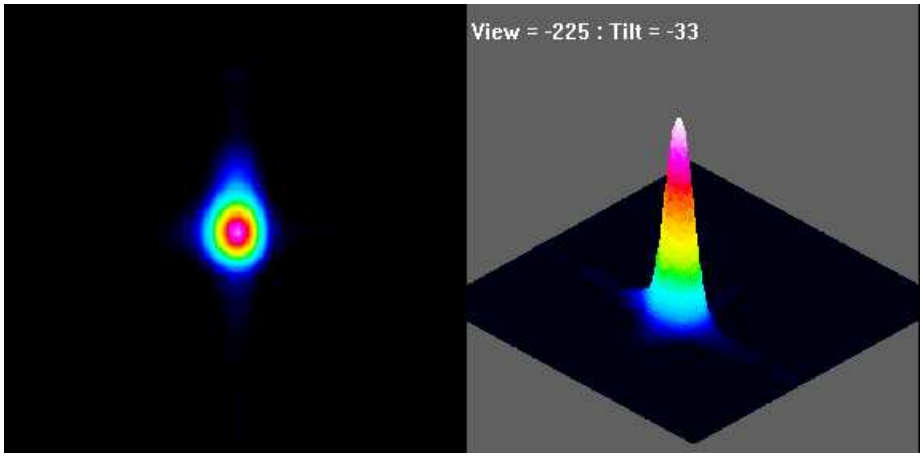

Figure 4.14: A knife edge image taken using the BeamMapC near the focus using the CW laser.

The v-axis beam size was fitted to the laser propagation function around the LWIP. W was measured in two ways: at the 13.5% clip level, and the second moment calculated using 99% of the total beam power international standards organisation criteria for beam size measurement. For a circular Gaussian beam, this is where the intensity falls to 1% of the peak intensity. Functions for calculating these quantities are built in to the knife edge's software. The second moment is the more accurate measurement because the it is less sensitive to different profile shapes than the clip level. Two fits are shown: in the first fit, M^2 is a free parameter (Fig. 4.15).

The knife edge was placed on a translation stage to achieve a long scan range. The horizontal error bars are due to the position error in the translation stage. There are several points at each location because the BeamMapC contains several knife edges.

It is apparent from this plot that the fitted W_0 is considerably smaller than the minimum W measured directly by the knife edge. M^2 is characterised by the ratio of the divergence to the minimum beam size. This means that the closer the minimum measured W is to the actual W_0, the more accurate is the measurement of M^2. The upper limit is the M^2 for which W_0 is equal to the minimum measured beam size. In this case, the upper limit is $M^2_{\text{laser+lens}} = 2.3$ (Fig. 4.16).

4.3.8 Optical Simulation of Laser-Wire System

A framework was developed for modelling the propagation of a Gaussian laser beam through drift space and lenses [30] using the following arguments: wavelength (λ), $\frac{1}{r}$ (r = the real part of the radius of curvature), radius (σ) and M^2. The complex radius of curvature was computed using

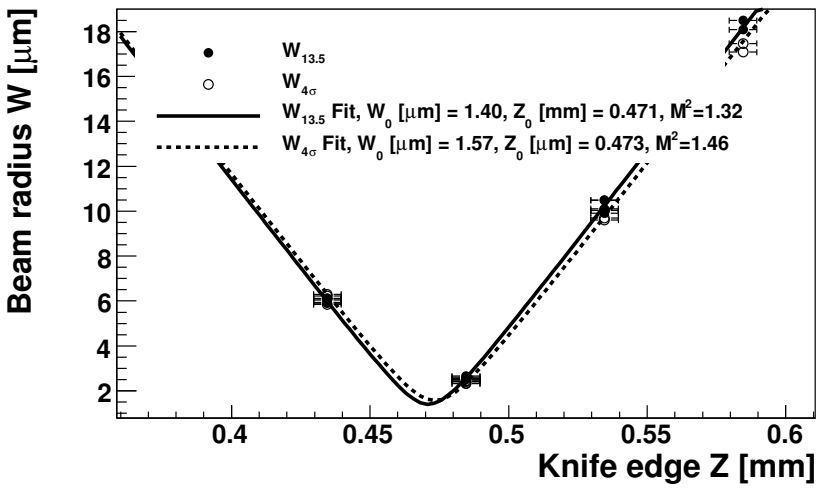

Figure 4.15: An IP profile measurement in the vertical axis of the CW laser after the custom final focus lens.

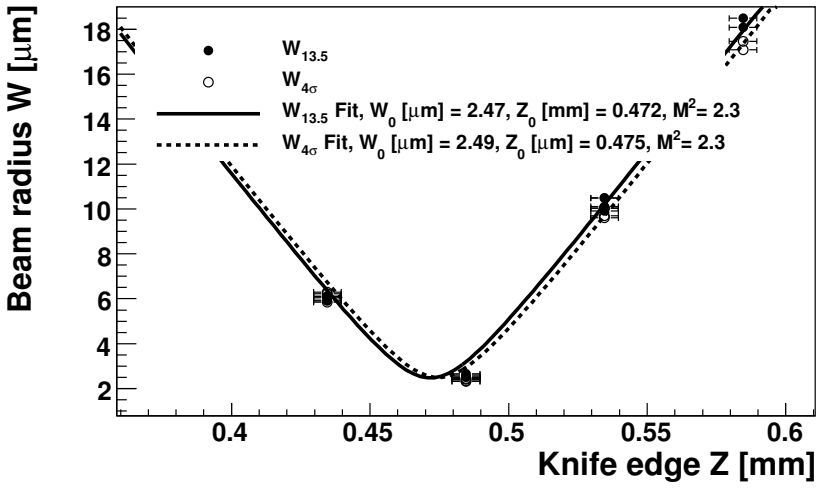

Figure 4.16: An IP profile measurement in the vertical axis of the CW laser after the custom final focus lens. The M^2 fit parameter is fixed at 2.3.

$$\frac{1}{q} = \frac{1}{r} - \frac{\lambda}{\pi(\sigma/M^2)^2} i \tag{4.9}$$

The simulated beam was transformed by applying a 2×2 propagation matrix to it to compute the new $\frac{1}{q}$ using

$$\frac{1}{q} = \frac{D \cdot \frac{1}{q_0} + C}{B \cdot \frac{1}{q_0} + A} \tag{4.10}$$

where q_0 is the initial complex radius of curvature. The beam size is calculated as

$$\sqrt{M^2} \cdot \sqrt{\frac{-\lambda}{\frac{1}{q_i}\pi}} \tag{4.11}$$

where q_i is the imaginary part of q.

Two propagation matrices were used: one for empty space of a certain length d (Eq. 4.12) and one for a thin lens of a certain focal length f (Eq. 4.13).

$$S_{\text{drift}} = \begin{bmatrix} 1 & d \\ 0 & 1 \end{bmatrix} \tag{4.12}$$

$$S_{\text{thinlens}} = \begin{bmatrix} 1 & 0 \\ -\frac{1}{f} & 1 \end{bmatrix} \tag{4.13}$$

Using this framework a model of the laser-wire system was created including the diagnostic arm with the 1 m focal length lens. The diagnostic lens is positioned on the table such that it is the same distance from the laser exit port as the final focus lens (11 m); therefore the state of the beam at the diagnostic lens and the final focus lens is the same. The beam's M^2 and radius were specified for each of the orthogonal axes at the final focus lens, along with the rotation angle, using the measurements of Secs. 4.3.2 and 4.3.6. The M^2 of the laser was measured in Sec. 4.3.2, along with the waist locations in the diagnostic arm after the 1 m focal length lens. The simulated M^2 of the final focus lens (Sec. 4.3.1) was also applied in this model.

CW Laser

The beam size at the exit of the CW laser is $\sim 75\%$ of its size at the lens input and its shape is circular. Using these criteria, the divergences at the lens input were calculated. Then further

divergences were applied at the diagnostic lens in order to match the measured focus locations (see Sec. 4.3.2). These divergences were slightly different, introducing additional astigmatism (this could be caused by lens tilt). The predicted diagnostic lens focus sizes in the two axes were then calculated.

Pulsed Laser

The same model was used to calculate the pulsed laser's beam size at the LWIP (σ_{lw}), including the divergences introduced by the diagnostic lens that were calculated using the CW laser data (Sec. 4.3.8). The M^2s and input beam sizes in the calculation were changed to match the measured values. The divergences were calculated using the diagnostic lens focus positions. Using this configuration, the beam size of the CW laser at the laser exit port was calculated to be 8.2 mm by 8.3 mm with 0.99 ellipticity, as expected. The calculated beam sizes at the diagnostic lens foci matched the measured values. The IP focus also matched the experimental data (Sec. 4.3.7), confirming the validity of the model.

To simplify matters the pulsed laser was assumed to be simply astigmatic; this is a reasonable approximation since the complex part of the rotation angle is small (Sec. 4.3.4). Furthermore, the general astigmatism could have been introduced by the diagnostic lens.

Finally, the pulsed laser was rotated by the astigmatism angle and propagated through the IP to estimate the minimum vertical laser beam size, σ_{lw}. Tab. 4.7. summarise these results. This model provides an estimate of σ_{lw}, however, further cross checks should be done to confirm its validity. The blank spaces in the table indicate places where a measurement either was not or could not be made. For example, the pulsed laser could not be measured directly at the IP due to the small spot size for which a knife edge scanner is required, and these only work with CW lasers. A measurement of the laser beam at the laser and at many points along its path would have been very useful in understanding the laser's propagation to the lens, but was not carried out due to time constraints.

Explanation of Values in Tab. 4.7

Shown in this table are measured values from Secs. 4.3.2, 4.3.6 and 4.3.7, which were used as inputs to the simulation. Rows 1 and 2 show the input beam sizes, W_{in} in the two axes. These values are inputs to the model. In rows 3 and 4 are the estimated beam sizes at the laser. These

were calculated after calculating the divergences by propagating back the distance from the lens to the laser, which is 11 m. The divergences were calculated using the locations of the minima of the 1 m diagnostic lens (Sec. 4.3.2). The astigmatism angle is from Sec. 4.3.6. The error in the measurement of the input beam size dominates the systematic uncertainties in all the outputs of the model because M^2_{lens} goes as the fourth power in W (Sec. 4.3.1)

Lines 6 and 7 in Tab. 4.7 show the foci of the main 56.6 mm focal length lens used in laser-wire running, as outputs from both the CW laser model and the pulsed laser model, as well as the IP profile measurement (Sec. 4.3.7). The measurement and model agree, within the uncertainties, to the lower bound of the model. W_{lw} is the vertical projection according to the astigmatism angle. The main result from the model is that it estimates that for the pulsed laser, W_{lw} is between 3.8 and 4.6 μm.

The bottom table of Tab. 4.7 summarises the measured M^2 values for the laser itself, as well as the total M^2, which includes contributions to the M^2 from the lens. Comparing the measured value of M^2_{tot} from the CW laser IP profile measurement (Sec. 4.3.7) we see that the lower bound of the output from the model is just above the upper bound given by the measurement.

In conclusion, the CW laser measurements were used to validate the model. The model shows some degree of success, although, because the lower bounds of the model values meet the upper bounds of the measurement values, this may be an indication that the model tends towards overestimation. However, the main systematic error, which is the error on the measurement of the input beam size, has been considered, and the main result is an estimate of the vertical beam size of the pulsed laser at the interaction point, $W_{\text{lw}} = 4.2 \pm 0.4$ μm.

4.3.9 Photo-diode Laser Power Meter Installation

A photo-diode was installed in order to monitor the laser beam power. The results using the photo-diode showed that the laser beam power does not change significantly during running with a stable room temperature. However, experience has shown that the laser is unstable during the first several hours after switching on. The laser is also sensitive to temperature fluctuations (Sec. 3.3.6). Under these conditions, the power may fluctuate.

	CW, mod.	CW, meas.	Pulsed, mod.	Pulsed, meas.
$W_{u,\mathrm{in}}$ [mm]	8.5−9.5 (input)	8.5−9.5	8.8−9.4 (input)	8.8−9.4
$W_{v,\mathrm{in}}$ [mm]	8.7−9.7 (input)	8.7−9.7	9.8−10.4 (input)	9.8−10.4
$W_{u,\mathrm{laserexitport}}$ [mm]	6.5−7.3 (output)		5.8−6.1 (output)	
$W_{v,\mathrm{laserexitport}}$ [mm]	6.5−7.3 (output)		6.2−6.6 (output)	
ϕ_{in} [deg.]	−13.9 (input)	−13.9	−75.3 (input)	−75.3
$W_{0,u}$ [μm]	2.4−4.2 (output)	1.6−2.5	5.6−4.4 (output)	
$W_{0,v}$ [μm]	2.7−4.6 (output)		5.1−6.3 (output)	
W_{lw}	3.0−4.6 (output)		3.8−4.6 (output)	~ 4 (coll. meas.)
$M^2_{\mathrm{las},u}$	1.08 (input)	1.08	2.07 (input)	
$M^2_{\mathrm{las},v}$	1.19 (input)	1.19	2.12 (input)	
$M^2_{\mathrm{tot},u}$	2.4−4.1 (output)	1.5−2.3	3.3−4.2 (output)	4.8−5.2 (coll. meas.)
$M^2_{\mathrm{tot},v}$	2.7−4.6 (output)		5.2−6.8 (output)	4.8−5.2 (coll. meas.)

Table 4.7: Input/output parameters to the laser propagation model and measured values.. Mod. means the value is either an input to or an output from the model. Meas. means measured value. Coll. meas. means collision measurement, see Sec. 4.5

4.4 Electron Beam Measurements

4.4.1 Beam Tests of Knife Edge for the f/2 Lens System

Because of the anticipated increased difficulty of finding collisions with the smaller laser beam sizes from the new f/2 lens, a new vacuum manipulator was installed for the knife edge. The same knife edge was used as described in Sec. 3.3.9. This new manipulator has four axes of travel: one vertical and two horizontal translational axes and a rotational axis. The translational axes allow the knife edge to be moved in and out of the electron beam. The rotational axis allows the knife edge to be rotated about the y axis to any angle. By rotating the knife edge to be perpendicular to the laser or electron beam, each beam's position can be found independently. At 45°, signal from both beams can be observed simultaneously. This helps to overlap the beams temporally. The knife edge can be extended or retracted until the laser beam is blocked. This locates the laser beam. Then the chamber is moved until ODR/OTR signal is observed. This locates the electron beam, and brings the separation between the to beams to within a few hundred microns. The fully retracted knife edge position is defined arbitrarily as 0 μm.

The vacuum manipulator was installed in the vacuum chamber and beam tests were performed. First, laser-wire electron beam optics were loaded and a wire scan was performed to check the beam size and approximate position using a wire scanner 63 cm upstream of the LWIP. The vertical beam size was ~ 50 μm.

Then the knife edge was rotated perpendicular to the electron beam and vertical knife edge scans were performed at different horizontal chamber positions. Fig. 4.17 is with the chamber at 0 μm horizontal position.

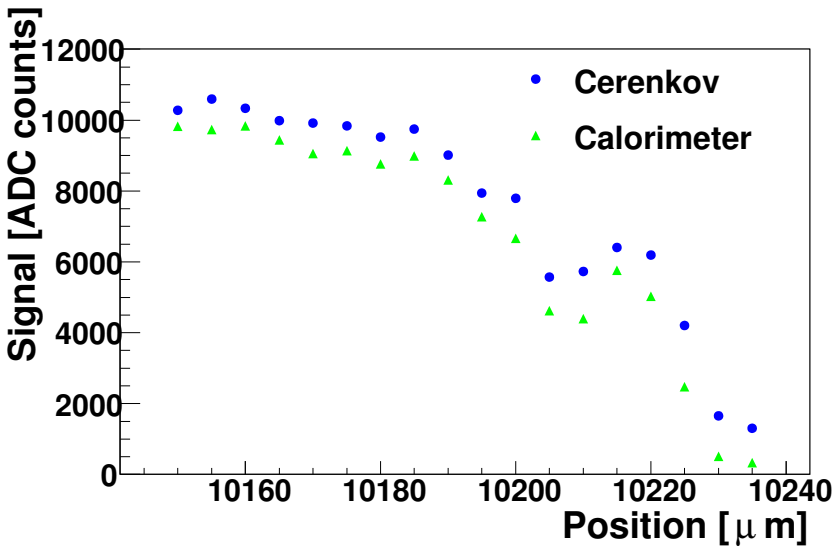

Figure 4.17: A vertical knife edge scan with the target perpendicular to the electron beam at 0 μm horizontal chamber position.

Next, the approximate positions of the sides of the knife edge were found. The knife edge was lowered into the beam by moving it to 10100 μm. Then the knife edge was moved in the horizontal axis. The sides were found at -3500 ± 200 μm and 3500 ± 200 μm (where the signal went to 0). There is a vertical "spike" on one side where the knife edge was broken. The negative side of this spike was found at -2700 ± 200 μm.

The same procedure was then carried out more carefully. Hysteresis was observed; there was a difference in the measured positions depending on the direction of motion of the chamber because there is a delay between the encoder readout and signal delay. The encoder readout is practically instantaneous but the signal only updates at a rate of ~ 1.5 Hz.

To remove the hysteresis we changed the method of finding the edge. We defined the edge as the position where the signal is half the maximum (~ 5000 ADC). This gave the results in Tab. 4.8. The data are consistent with the knife edge width of 7 mm. They show that the centre of rotation is near the centre of the knife edge.

Next an avalanche photo-diode (APD) was inserted post-IP to detect ODR and OTR (Fig.

Angle [deg.]	− edge [μm]	+ edge [μm]
45	-2700 ± 100	2700 ± 100
0	-3250 ± 100	4000 ± 100

Table 4.8: Beam line elements between QD4X and LWIP.

3.6). With the knife edge at 45° to the electron beam, the peak APD value was read from the scope as a function of manipulator z-shift and plotted in Fig. 4.18.

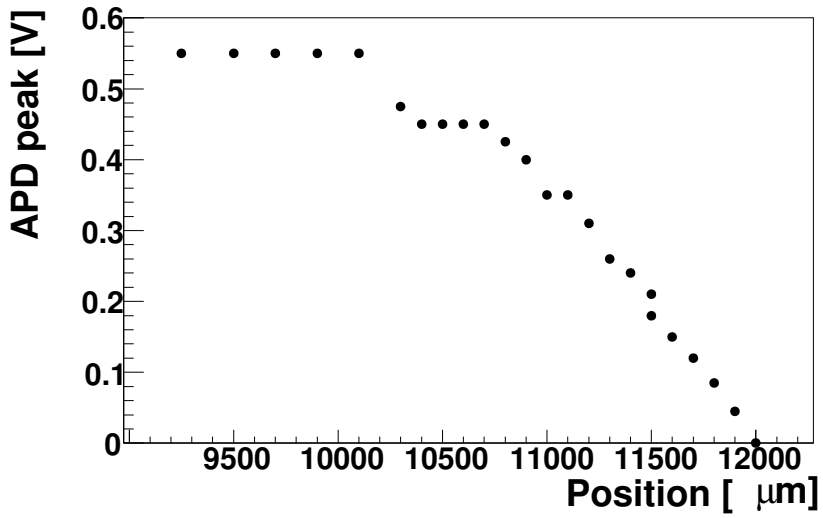

Figure 4.18: A vertical knife edge ODR/OTR scan using an APD as a detector with the knife edge 45° to the electron beam.

This scan helped to find the midpoint in the signal output. The knife edge was moved to a z-shift of 9250 μm, with the beam passing through the knife edge, and the results are plotted in Fig. 4.19. These tests were done to ensure that the knife edge was at an angle where a signal from the knife edge could be observed during the collision finding process. The structure appears similar to that of ODR/OTR. Further information can be found in [18, 19].

Laser/Chamber Alignment with the Knife Edge

In order to find collisions with the electron beam, the chamber/lens and knife edge must be aligned with the laser. To do this, the following procedure was carried out.

First the laser alignment was completed using a CW alignment laser to make sure the laser was going through the centre of all the optics and going through the centre of the final lens with all the back reflections aligned.

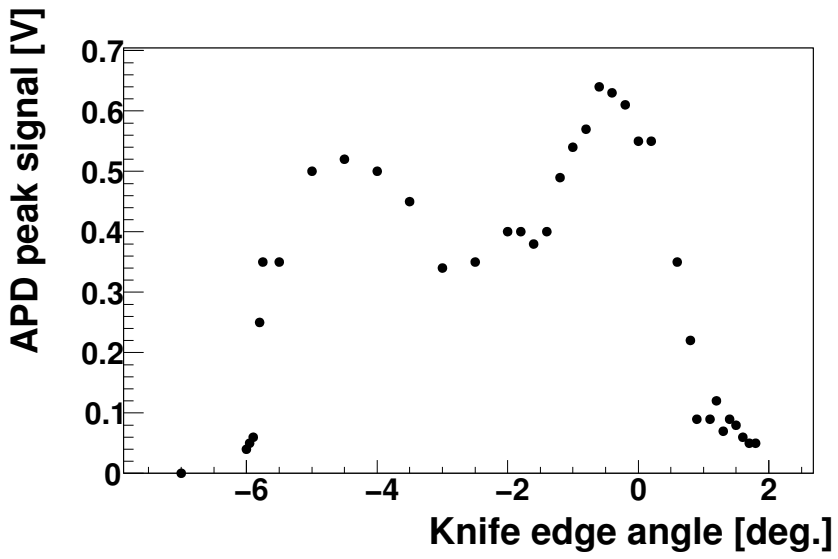

Figure 4.19: A knife edge angular ODR/OTR scan using an APD as a detector with the z-shift at 9250 μm (full signal). Here, 0° means 45° to the electron beam.

Then the knife edge was moved into the laser beam and the post-IP laser light was observed, using a piece of lens tissue taped over the exit window, at different values of the knife edge manipulator z-shift, with the laser beam focused on the knife edge. In Fig. 4.20 (left) the top half of the beam is obscured by the knife edge. In Fig. 4.20 (centre) the knife edge is in an intermediate position. In Fig. 4.20 (right) the bottom portion of the laser beam is obscured. The distance of knife edge travel in z between Fig. 4.20 (left) and Fig. 4.20(right) is of the order of a few μm. When the knife edge is just above the focus, the beam can be blocked by moving the knife edge down 5 μm. Therefore the laser beam's position with the knife edge can be found to a sufficient degree of accuracy to narrow the collision search to an acceptable range.

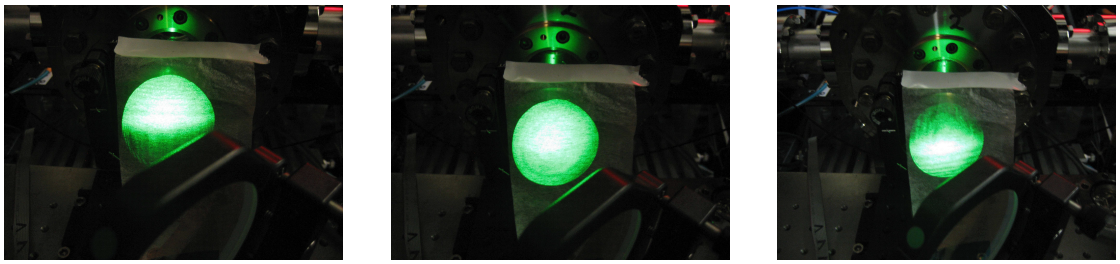

Figure 4.20: *Left:* CW laser light at exit window with knife edge before the focus in z. The top part of the beam is obscured. *Centre:* CW laser light at exit window with knife edge at the focus in z. The laser beam is small enough to pass under the knife edge. *Right:* CW laser light at exit window with knife edge after the focus in z. The bottom part of the beam is obscured.

4.4.2 BPM Calibration

The pedestal of a BPM is the output seen when there is no beam passing through the accelerator. The pedestals of the BPMs were taken. The chamber was then scanned vertically and horizontally; the pedestal subtracted signal was plotted as a function of vertical and horizontal displacement and the data fitted to a straight line. The results are in Tab. 4.9. The chamber position was calibrated using precision encoders which measure the chamber position to within 0.1 μm.

	x [μm]	y [μm]
1	$(6.21 \pm 0.01) \cdot 10^{-2} + (5.57 \pm 0.01) \cdot 10^{-5} x$	$(-1.93 \pm 0.01) \cdot 10^{-2} + (5.32 \pm 0.01) \cdot 10^{-5} y$
2	$(3.33 \pm 0.01) \cdot 10^{-2} + (3.13 \pm 0.01) \cdot 10^{-5} x$	$(-6.12 \pm 0.01) \cdot 10^{-2} + (8.11 \pm 0.01) \cdot 10^{-5} y$

Table 4.9: 29/05/08. Calibration equations for BPM 1 (downstream) and BPM 2 (upstream) in x (horizontal) and y (vertical) axes.

4.4.3 Dispersion Measurement

The laser-wire optics were designed such that there is a point of zero dispersion at the LWIP (Sec. 3.2.1). This was verified by carrying out dispersion, D, (Sec. 2.2) measurements using the 2 calibrated BPMs attached to the chamber upstream and downstream of the LWIP, and the wire scanner WS, 63cm upstream of the LWIP.

Wire Scanner

A horizontal wire scanner measurement was performed to measure σ_x with the QD4X current set to 74.56 A, so that the electron beam waist is at the LWIP. σ_x was measured as 169.117 ± 0.025 μm.

The equation for the beam size in terms of β function and dispersion is

$$\sigma = \sqrt{\beta\varepsilon + D^2 \left(\frac{\Delta E}{E}\right)^2}. \tag{4.14}$$

In the ATF the horizontal emittance is ~ 2 nm. From the MAD calculations β_x at the WS is 0.194 m. Therefore, with zero dispersion, from Eq. 4.14, $\sigma_x \sim 19.7$ μm which is much less than 169 μm. This means that the horizontal dispersion dominates the measurement. Therefore, we can approximate the dispersion with $D_x = \frac{\sigma_x E}{\Delta E}$. The quantity $\frac{\Delta E}{E}$ is measured as $8 \cdot 10^{-4}$, so

$D_x = 0.2$ m. This agrees approximately with the MAD [9, 10, 11] calculation, $D_x = 0.140$ m.

Beam Energy and BPMs

The beam energy was changed by changing the frequency of the damping ring accelerating cavity by -4 kHz to +2 kHz from the original setting (-1 kHz) in 1 kHz steps, and the position was plotted as a function of change of frequency. A parabola was fitted to each of these plots and the tangent calculated at -1 kHz to find the change in position as a function of change in cavity frequency. These values were plotted with distance from the beginning of the extraction line s (Figs. 4.21, 4.23). The test was repeated with skew quadrupole QS1X turned on, with a current of -5A (Figs. 4.26, 4.25). In each of these plots the LWIP is shown by a vertical red dashed line. The MAD [9, 10, 11] calculation is shown (Fig. 3.3 is 4.21 repeated again here) for comparison.

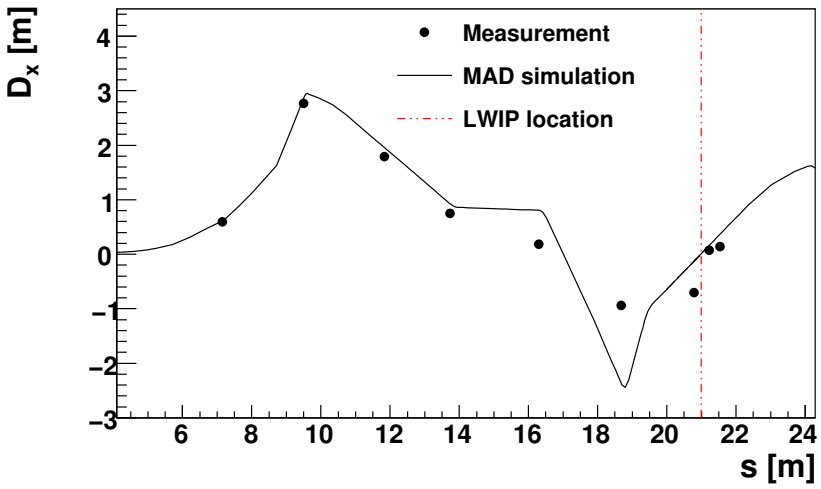

Figure 4.21: ATF extraction line measured and simulated dispersion. The upstream quadrupole focusing strengths where $k_{QD4X} = -1.516659$ [1/m], $k_{QF4X} = 1.574676$ [1/m], and $s = 0$ corresponds to the beginning of the extraction line. The error bars are too small to be visible.

The measured D_x function (Figs. 4.21, 4.22) is approximately in agreement with the MAD [9, 10, 11] calculation (Fig. 4.21). However, the measured horizontal dispersion at the LWIP is -0.32 m, whereas the MAD [9, 10, 11] simulation predicts -0.013 m. At BPM1, the simulation predicts $D_x = -0.140$ m, but the measured value is $D_x = -0.7$ m. At BPM2, the MAD [9, 10, 11] simulation predicts $D_x = 0.134$ m, but the measured value is $D_x = 0.04$ m.

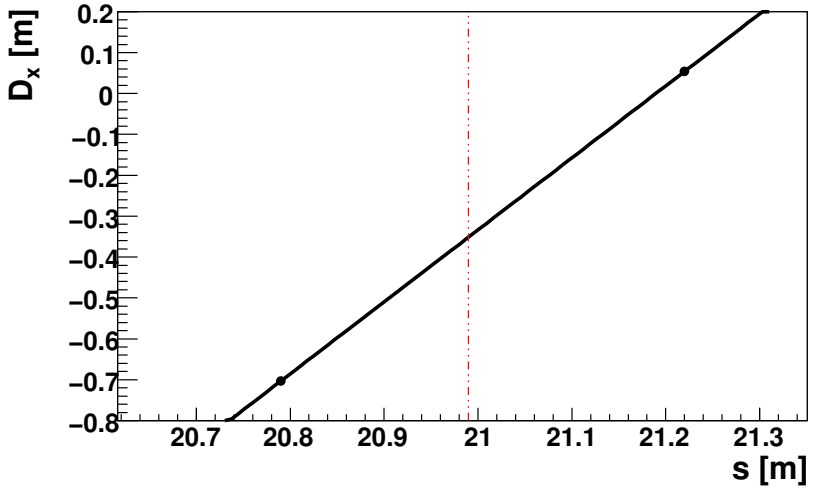

Figure 4.22: ATF extraction line measured dispersion function $D_x(s)$, where $s = 0$ corresponds to the beginning of the extraction line. The vertical dashed line indicates the location of the LWIP. The error bars are too small to be visible.

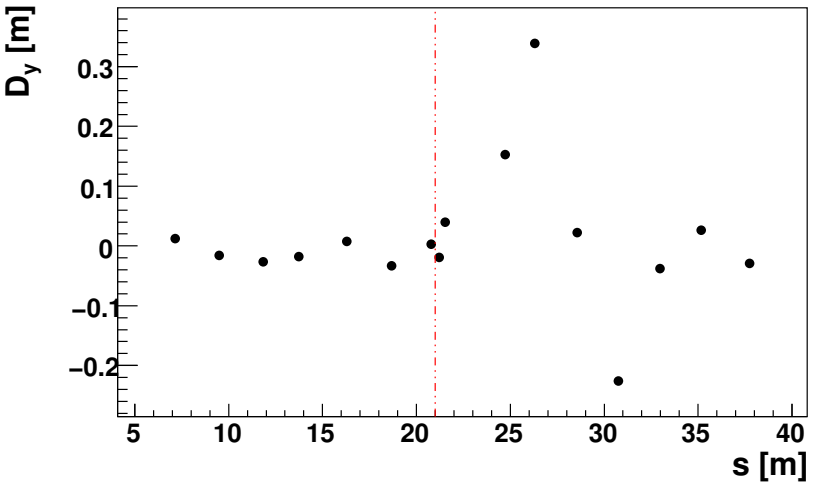

Figure 4.23: ATF extraction line measured dispersion function $D_y(s)$, where $s = 0$ corresponds to the beginning of the extraction line. The vertical dashed line indicates the location of the LWIP. The error bars are too small to be visible.

The D_y plot (Fig. 4.23) shows some vertical dispersion is present.

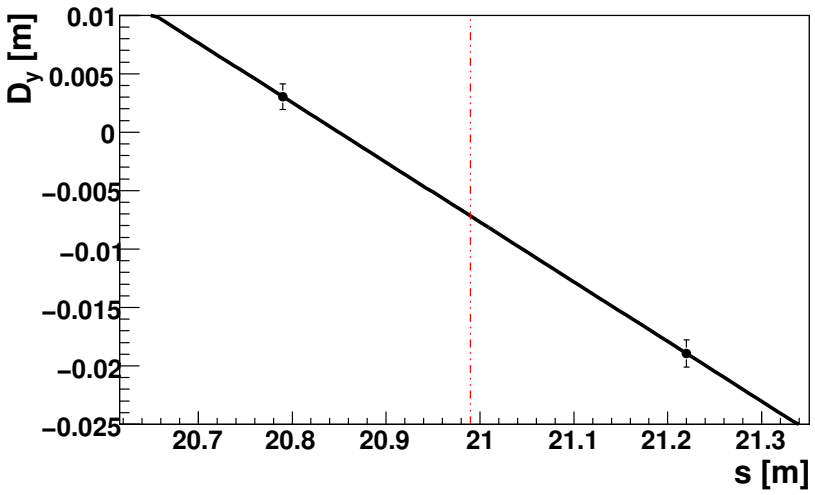

Figure 4.24: ATF extraction line measured dispersion function $D_y(s)$, where $s = 0$ corresponds to the beginning of the extraction line. The vertical dashed line indicates the location of the LWIP.

Fig. 4.24 shows D_y at the laser-wire BPMs. The dispersion function will be a straight line between the laser-wire BPMs either side of the LWIP as there are no magnets present. Therefore, a straight line is fitted to the dispersion data at the two laser-wire BPMs to estimate the dispersion at the LWIP. The fitted function was zeroed at $\bar{s}$, the average position, to make calculating the extrapolated error in D at the LWIP easier by cancelling the covariance term. This is a purely statistical technique. The results of the fits are summarised in Tab. 4.10.

	p_0 [m]	p_1	D @ LWIP [m]	σ_D [μm]
29/05/2008				
Hor.	-37.3 ± 0.3	1.76 ± 0.01	$(-3.2 \pm 0.1) \cdot 10^{-1}$	251 ± 11
Ver.	1.07 ± 0.08	-0.051 ± 0.004	$(-3.9 \pm 0.8) \cdot 10^{-3}$	3.03 ± 0.66
Hor., QS1X=-5A	-5.3 ± 0.3	0.25 ± 0.01	$(-3.2 \pm 0.1) \cdot 10^{-1}$	251 ± 11
Ver., QS1X=-5A	4.0 ± 0.1	-0.192 ± 0.005	$(-20.0 \pm 2) \cdot 10^{-3}$	15.8 ± 1.3

Table 4.10: Straight line ($p_0 + p_1 s$) dispersion fits between the LWBPMs.

Figs. 4.22 and 4.24 show that the horizontal dispersion crosses zero 20 cm downstream of the LWIP and the vertical dispersion crosses zero 14 cm upstream of the LWIP. There are two contributions to the error in the dispersion measurement: a statistical error and a systematic error associated with the uncertainty of the position of the LWIP relative to the BPMs. This uncertainty in the position is ~ 5 mm. The dispersion was calculated with the LWIP shifted by

5 mm to calculate the systematic error and this was added to the statistical error to produce the error shown in Tab. 4.10. At the LWIP the dispersion is ~ -3.9 mm.

In order to calculate σ_D, the contribution to the beam size from the dispersion, an estimate of the momentum spread was needed. The momentum spread depends on intra-beam scattering, assuming a low emittance beam, and is a function of bunch charge. This effect was studied previously in the ATF extraction line [22]. Bunch charge measurements taken during the dispersion measurements show that the bunch population was $0.7 \pm 0.05 \times 10^{10}$ electrons. With this information, and the momentum spread plot from [22] the momentum spread $\frac{\delta E}{E}$ is estimated to be $(7.8 \cdot 10^{-4} \pm 2.8 \times 10^{-5})$, where the error is the statistical error in the momentum spread due to fluctuations in the bunch charge (1.25×10^{-5}) added in quadrature to the estimated error on the measurement in Fig. 3 in [22], which is $\sim 2.5 \times 10^{-5}$. This assumes that $\varepsilon_y/\varepsilon_x \sim 1\%$, in other words $\varepsilon_y \sim 10$ pm. The contribution from this systematic error is negligible compared with the other uncertainties; it is 1.5%. Therefore, this estimation of the momentum spread is sufficient, and to improve the error in σ_D, improvements need to be made in the accuracy of the dispersion measurement first, for example, by improving the resolution of the BPMs.

With $\frac{\Delta E}{E} = 7.8 \cdot 10^{-4}$, this gives a beam size due to dispersion of $\sigma_d = 3.0$ μm at the LWIP. The minimum β function, calculated by MAD [9, 10, 11], is 0.008 m. This is consistent with Tab. 3.3 because the minimum falls between two of the quad settings. The emittance was measured in the dispersion free region as 207 pm. Therefore the beam size without dispersion is $\sigma_\beta = 1.28$ μm. Therefore we expect a vertical electron beam size at LWIP of $\sigma_e = \sqrt{\sigma_\beta^2 + \sigma_d^2} = 3.26$ μm. Moving the zero dispersion point, or the laser-wire, along the beam line so that the LWIP crosses is at the zero dispersion crossing, or correcting the dispersion, would reduce σ_e to ~ 2 μm, or smaller, depending on the emittance.

4.5 Collision Measurements

Here the collision measurements carried out with the custom lens system are described and the results are presented.

For laser scanning with the upgraded system the method of changing the position of the laser beam is different. The lens is fixed to the vacuum chamber. The laser is aligned in the centre of and perpendicular to the lens surface using the final two mirrors. The vertical position of the

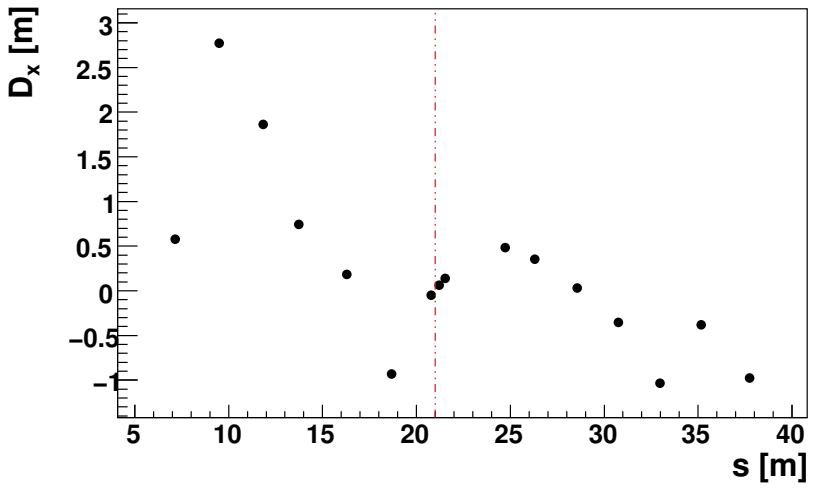

Figure 4.25: ATF extraction line measured dispersion, $D_y(s)$ with $I_{QS1X} = -5$ A, where $s = 0$ corresponds to the beginning of the extraction line. The vertical dashed line indicates the location of the LWIP. The error bars are too small to be seen.

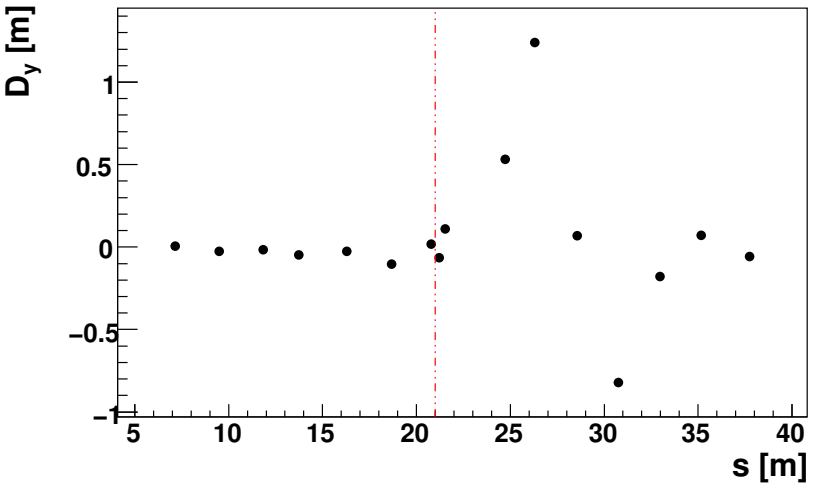

Figure 4.26: ATF extraction line measured dispersion, $D_x(s)$ with $I_{QS1X} = -5$ A, where $s = 0$ corresponds to the beginning of the extraction line. The vertical dashed line indicates the LWIP. The error bars are too small to be seen.

laser beam is changed by moving the chamber vertically. There is a 1:1 relationship between the change in the vertical positions of the chamber and the laser beam.

σ_c was estimated from data in three different ways:

1. A constant + Gaussian fit function, Eq. 4.15.
2. The full electron beam- laser beam overlap integral, Eq. 2.96, + a constant.
3. A 4 sigma second moment calculation. The beam size is estimated using a Gaussian + straight line fit and the second moment is calculated using 95% of the area of the profile. The advantage of this method is that it calculates the second moment correctly for any profile shape. The disadvantage is that any noise in the tails of the profile is added to the second moment. If the signal to noise ratio is low then the beam size will be overestimated.

Here the Gaussian fit function is written out explicitly:

$$Ae^{-\frac{1}{2}\left(\frac{x-x_0}{\sigma_c}\right)^2} + p_0, \tag{4.15}$$

In all cases the background is subtracted first by fitting a straight line to the tails of the distribution.

Laser waist scans were performed using the electron beam, similar to Sec. 3.5.2. With the upgraded custom lens system the lens is fixed to the vacuum chamber instead of to a lens mount on a stage; the chamber is moved along the laser beam propagation axis to change the focus position. Quad scans are performed as described in Sec. 3.5.3. A quad scan using a single quadrupole was also performed; in this case only I_{QD4X} is changed. The results of simulations of these scans are shown in Tab. 3.3. The double quad scan keeps the horizontal and vertical waists at the same s as each other. However, scanning with two quads makes emittance measurement more complicated (Sec. 2.1.9).

4.5.1 Smallest σ_c Laser Scan

A plot of the smallest σ_c laser scan is shown in Fig. 4.27.

This scan was performed after tuning the skew quadrupoles (Sec. 4.5.6). σ_c for this scan is shown in Tab. 4.11. This scan's σ_c is the lowest point in Fig. 4.38.

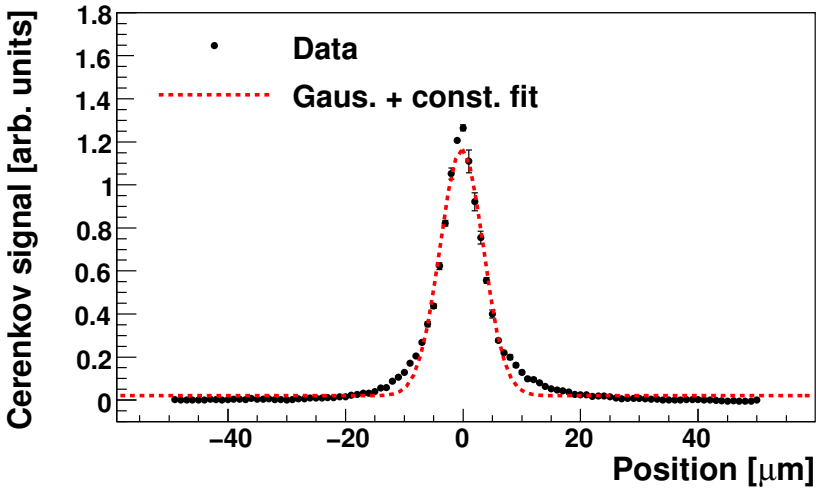

Figure 4.27: The smallest σ_c laser scan measured using the laser wire system. Gaussian + constant fit function is shown. The scan was performed on 29th May 2008 after skew quadrupole tuning.

Analysis Method	σ_c [μm]
Gauss. + const.	3.65 ± 0.09
RMS at 95%	5.1 ± 0.4

Table 4.11: σ_C calculated from Fig. 4.27 using Gaussian + constant and Gaussian + line fits and 4σ second moment calculation.

The tails in Fig. 4.27, which occur at small electron beam sizes cannot be attributed to electron beam halo (Chap. 5) or to tails in the laser beam profile (the laser knife edge scans at the LWIP an almost Gaussian beam, 4.3.7) because they are too large. The full electron beam-laser beam overlap integral (Eq. 2.96) produces tails in the convoluted distribution when the horizontal electron beam size is of a similar size to the Rayleigh length of the laser beam.

An overlap integral fit is shown in Fig. 4.28. The limits to the range of values the fit parameters were allowed to take is shown Tab. 4.12. These limits are taken from the laser beam measurements (Sec. 4.3). The fit results are shown in the same table. The fit takes as one if its inputs the laser beam size input on the lens, W_{in}, and includes the input beam size versus M^2_{lens} model (Eq 4.2, Tab. 4.3). The function fits the data well and the fit results are reasonable, despite the large error on σ_{ex}, which was not measured directly, but influences the shape of distribution. We conclude that the tails in the distribution are due to Rayleigh range effects.

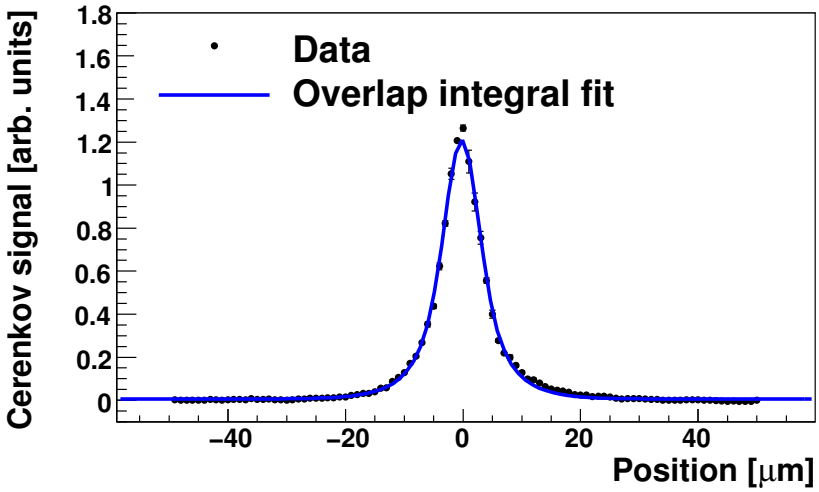

Figure 4.28: The smallest σ_c laser scan measured using the laser wire system. Overlap integral fit function is shown. The scan was performed on 29th May 2008 after tuning the skew quadrupoles.

Since σ_x is not known, the overlap integral is not used in the main data analysis. Because the tails in the convoluted distributions are due to Rayleigh range effects, σ_c is measured approximately by fitting a Gaussian.

Parameter	x_0 [μm]	σ_{ey} [μm]	σ_{ex} [μm]	W_{in} [mm]
Inputs	$0 \pm \sigma_{\text{sm}}$	0.8 - 3$\times\sigma_{\text{sm}}$	16 - 200$\times\sigma_{\text{sm}}$	8.8 - 10.04
Fit results	0.65 ± 0.03	1.8 ± 0.2	58 ± 20	8.8 ± 0.01

Parameter	f [mm]	M^2_{las}	Δx [μm]
Inputs	55.55 - 56.65	1.8 - 2.2	0 (fixed)
Fit results	56.6 ± 0.01	1.998 ± 0.004	0 (fixed)

Table 4.12: Limits applied to the input parameters of the overlap integral fit. x_0 is the mean position in the distribution. W_{in} is the input beam size ($W = 2\sigma$). f is the focal length of the lens. σ_{sm} is the calculated second moment. Δx is the displacement of the electron beam along the laser propagation axis.

4.5.2 Profiling the Laser Beam Using the Electron Beam

The laser propagation was measured using a laser waist scan. σ_{ey} was large enough that the vertical scan profiles remained approximately Gaussian. A second moment calculation was also performed for each vertical scan. The measurement was performed before the dispersion was corrected and so the 3 μm contribution to the beam size from the dispersion (Sec. 4.4.3) was subtracted quadratically from each σ_c data point. The dispersion is the dominating contribution to the electron beam size (see Sec. 4.4.3). The data and fits are plotted in Fig 4.29, and the results from the fit function are shown in Tab. 4.13.

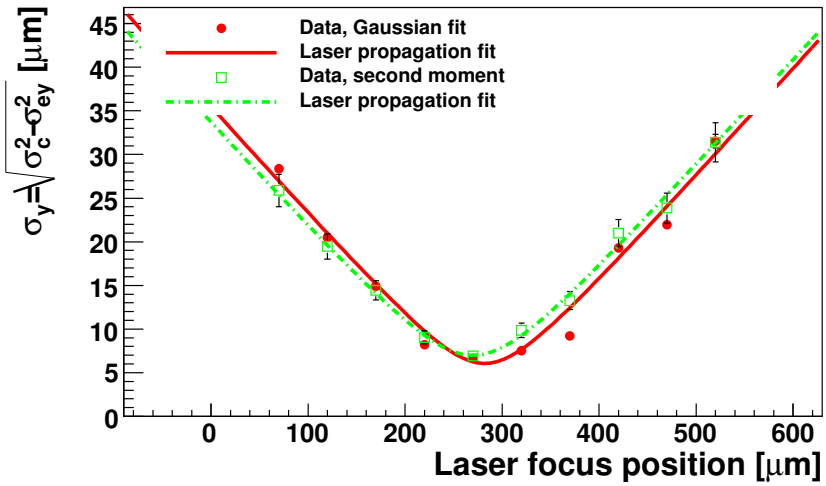

Figure 4.29: Waist scan. 29/05/2008. The laser focus position is x in electron beam coordinates. The fit function is the laser propagation function, Eq. 2.86.

This agrees with the hypothesis that the lens was overfilled, creating a large M^2 (Secs. 4.3.1, 4.3.6).

Analysis Method	W_0 [μm]	M^2
Gauss. + const.	7.0 ± 0.4	5.0 ± 0.2
Second moment	11.0 ± 0.1	8.7 ± 0.1

Table 4.13: Results of laser propagation fits to Fig. 4.29.

4.5.3 Vertical Scans Statistics Study

Two scans were performed with a different number of shots at each laser-wire position, for comparison. A single shot scan is shown in Fig 4.30 and a 10 shot scan is shown in Fig. 4.31. A Gaussian + constant was fitted.

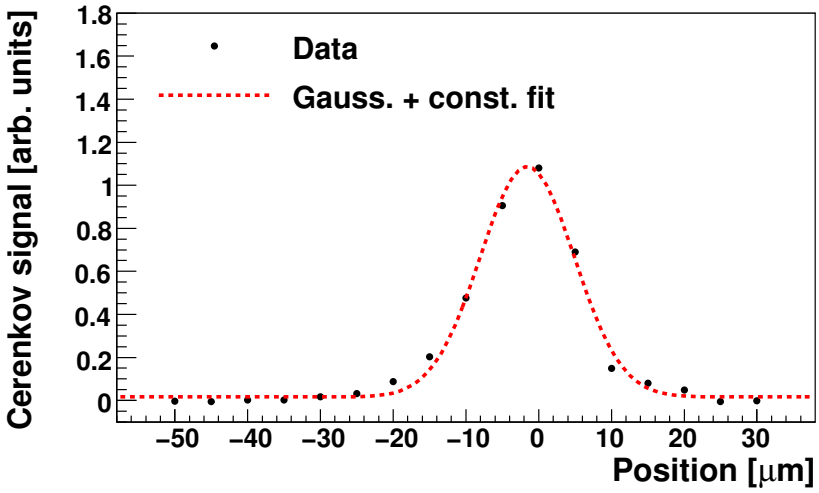

Figure 4.30: A single shot scan near the laser focus at the default quad settings

With the single shot scan, the fitted size is $\sigma_c = 6.5 \pm 0.3$ μm (statistical error).

With the ten shot scan, the fitted size is $\sigma_c = 6.1 \pm 0.3$ μm (statistical error).

There was no change in statistical error and the beam sizes were the same to within the error.

4.5.4 Single Quad Scan

A single quad scan was performed. The current through QD4X was changed while the current through QF4X was held constant at 73.58 A. The results are shown in Figs. 4.32 and 4.33. The vertical beam sizes were calculated using two different methods: a Gaussian plus constant fit and a second moment calculation.

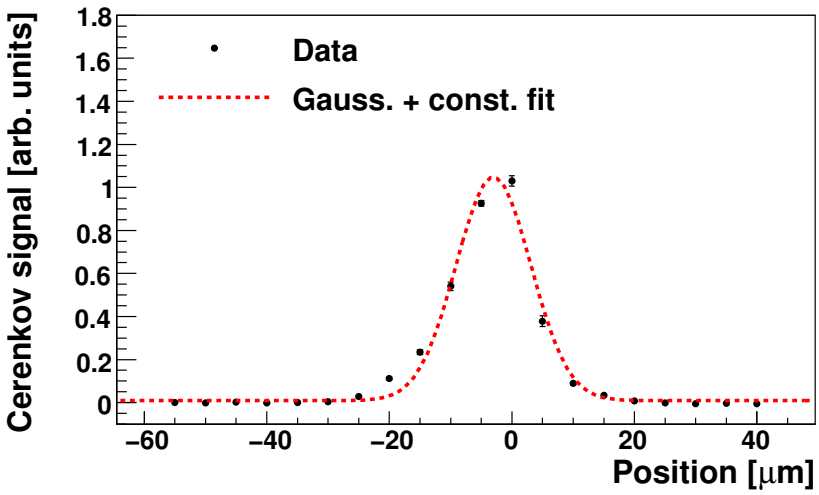

Figure 4.31: A 10 shot scan near the laser focus at the default quad settings

4.5.5 Emittance Measurement Using Wire Scanner

The emittance can be measured using the method described in Sec. 2.1.9. Firstly, the transfer matrix between the quadrupole and the point where the electron beam is measured, S_{12}, must be calculated.

The thin lens approximation assumes that the thickness of the quadrupoles is zero. To test the validity of the thin lens approximation applied to this specific calculation, we compare the thin lens components of the transfer matrices with the thick lens components of the transfer matrices.

The thick lens transfer matrix for a quad followed by a drift space is

$$\begin{bmatrix} 1 & L \\ 0 & 1 \end{bmatrix} \begin{bmatrix} \cos k\lambda & \frac{\sin k\lambda}{k} \\ -k\sin k\lambda & \cos k\lambda \end{bmatrix} = \begin{bmatrix} \cos k\lambda - Lk\sin k\lambda & \frac{\sin k\lambda}{k} + L\cos k\lambda \\ -k\sin k\lambda & \cos k\lambda \end{bmatrix} \tag{4.16}$$

where L is the drift length, λ is the thick quad length and k is the focusing strength. The thin lens followed by drift space matrix is

$$\begin{bmatrix} 1 & L \\ 0 & 1 \end{bmatrix} \begin{bmatrix} 1 & 0 \\ -K & 1 \end{bmatrix} = \begin{bmatrix} 1-LK & L \\ -K & 1 \end{bmatrix} \tag{4.17}$$

where $K = kl \sim \sqrt{k}\sin\sqrt{k}\lambda$. Therefore the thin lens approximation is valid if $\cos k\lambda \sim 1$ and

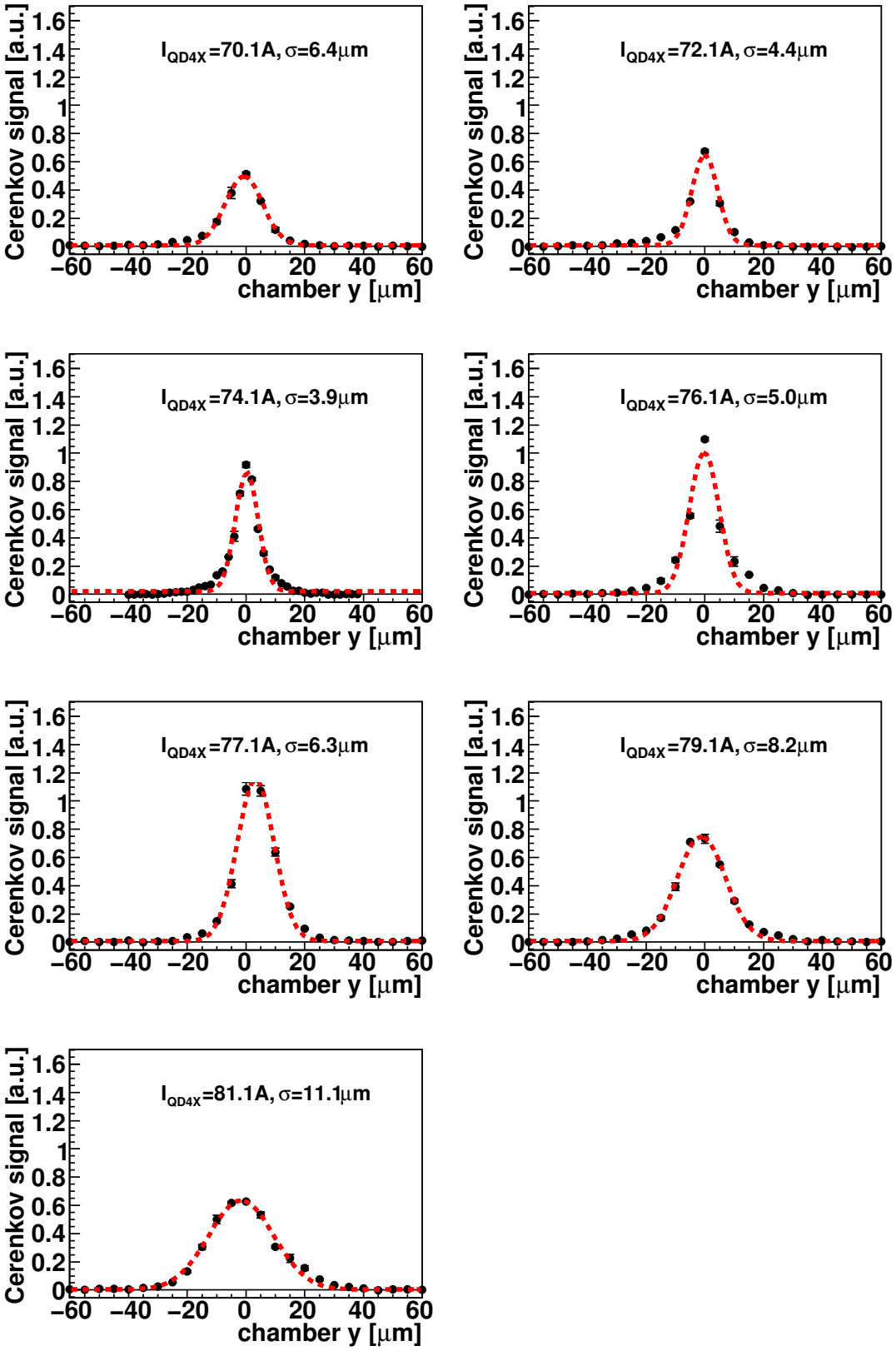

Figure 4.32: QD4X quad scan. QF4X current was kept constant at 73.58 A. The black dots are data. The red lines are Gaussian + constant fits.

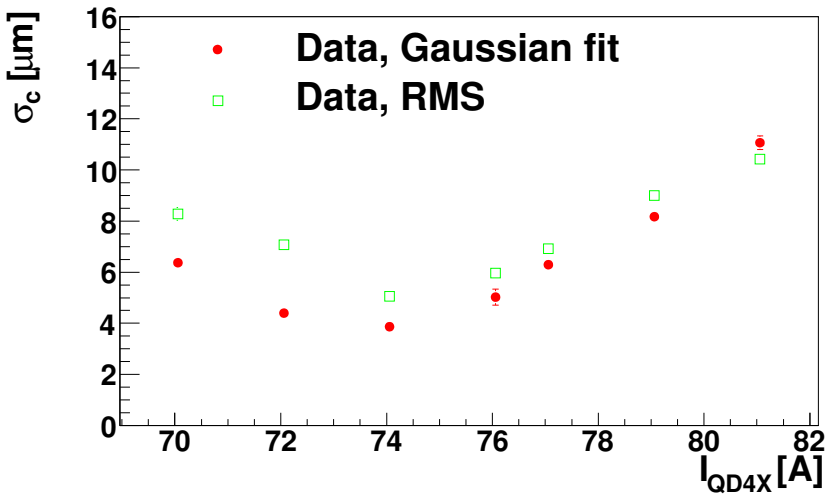

Figure 4.33: QD4X quad scan. QF4X current was kept constant at 73.58 A.

$\frac{\sin k\lambda}{k} << L\cos k\lambda$. In our case, $\lambda = 0.19861$ m and $L = 1.3$ m. For the given scan range, $-1.7 < k_{QD4X} < -1.5$ and $0.32 < k_{QF4X} < 0.79$. The worst case is $kL = -1.7 * 0.19861 = -0.34$, which gives $\cos kL = 0.94 \sim 1$. $k\lambda$ is small, so $\frac{\sin k\lambda}{k} \sim \lambda$. $\lambda = 0.15L$. In this case the thin lens approximation provides a rough calculation of the beam emittance.

The downstream beam size σ_2 can be written using the upstream beam parameters [7] (Sec. 2.1.9) as

$$\sigma_2^2 = \varepsilon\beta_2 = \varepsilon(S_{11}^2\beta_1 - 2S_{11}S_{12}\alpha_1 + R_{12}^2\gamma_1) \tag{4.18}$$

Therefore the emittance is calculated by fitting

$$\sigma_2^2 = \varepsilon\left[(1-LK)^2\beta_1 - 2(1-LK)L\alpha_1 + L^2\gamma_1\right] \tag{4.19}$$

where $K = k\lambda$, α_1, β_1 and γ_1 are the Twiss parameters, σ_2 is the measured beam size and ε is the emittance.

Double Quad Scan Emittance Measurement

Double quad scans (Sec. 3.2.1) were performed in order to keep the horizontal and vertical electron beam waists at the same position along the beam line relative to one another. Other combinations such as orthogonal tuning knobs were not considered. The transfer matrix through

two quads and two drifts is found by multiplying Eq. 4.17 by a quad matrix followed by a drift matrix. The terms in the top row of the resulting transfer matrix are

$$S_{11} = 1 - L_1K_1 - L_2K_2 + L_1L_2K_1K_2 - L_2K_1 \tag{4.20}$$

and

$$S_{12} = L_1 - L_2K_2L_1 + L_2 \tag{4.21}$$

where the subscripts 1 and 2 on the RHS refer to the upstream and downstream quadrupole/drift pair respectively. Therefore, the emittance can be found by substituting Eqs. 4.20 and 4.21 into Eq. 4.18 and fitting.

The emittance was measured (data from [41]) by varying quadrupole QD8X and measuring the vertical beam size using wire scanner MW3X, which is 2.52 m from QD8X. The squared beam size was fitted to Eq. 4.19, shown in Fig. 4.34, with the skew quadrupoles QK1X and QK3X turned off, and Fig. 4.35 with the skew quadrupoles turned on.

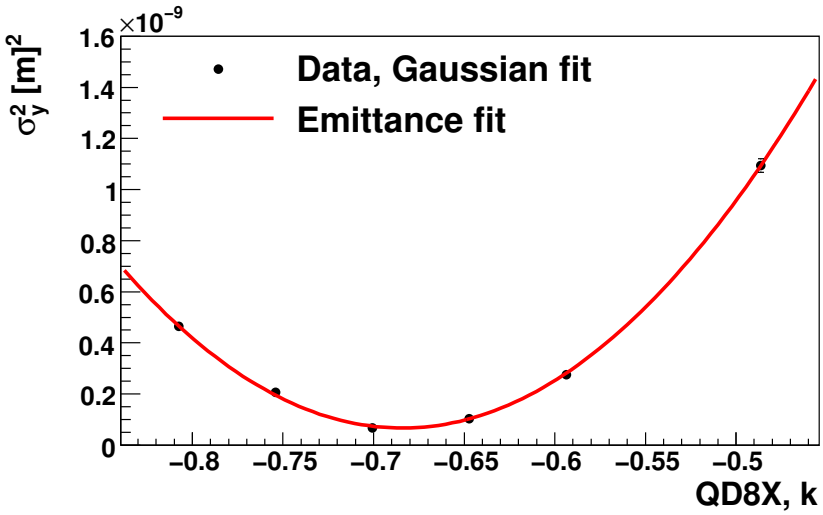

Figure 4.34: Emittance measurement with skew quadrupoles off.

The currents through QK1X and QK3X are -2.2 A and -4.5 A respectively. With the skew quadrupoles turned off the emittance is measured as 213 ± 3 pm. With the skew quads on the emittance is 207 ± 2 pm. The uncertainties in these measurements are statistical. The difference between the two is not significant. The emittance measured here is 10 times bigger than the

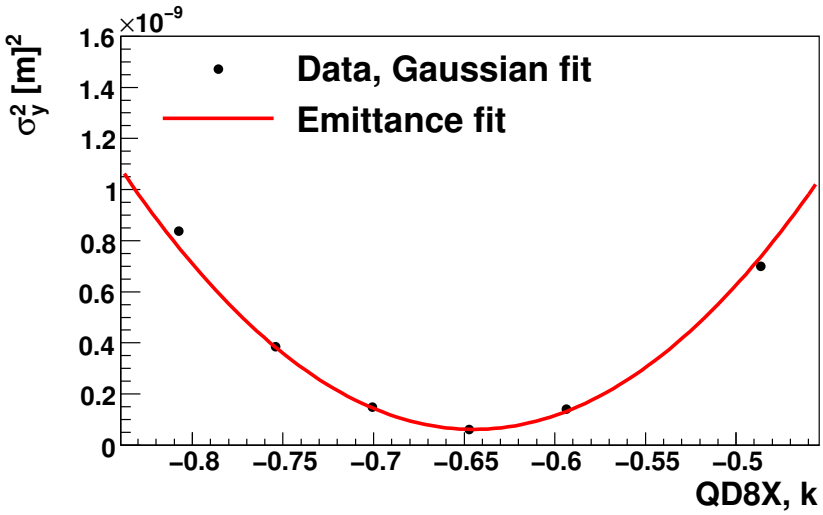

Figure 4.35: Emittance measurement with skew quadrupoles on.

normal value which means that the beam size is 3 times bigger than expected. This means that at the LWIP the vertical beam size is ~ 3 μm.

4.5.6 Skew Quad Scan

The QD4X current was set to the minimum, at 74.06 A, and skew quadrupoles QS1X and QS2X were scanned to try and reduce the vertical beam size.

First QS1X was scanned and σ_c measured at each quad setting (Fig. 4.38). The best value was the maximum negative value, -5 A, with $\sigma_c = 3.7$ μm (Figs. 4.36, 4.37 and 4.38).

With I_{QS1X} at -5.0 A, QS2X was scanned (Figs. 4.39 and 4.40). The minimum was at $I_{QS2X} = -2.0$ A, with $\sigma_c = 3.65$ μm.

The process was repeated on 29/05/08 (Figs 4.41 and 4.42). On this occasion, only QS1X was required to minimise the beam size. σ_c was changed from 4.10 μm at $I_{QS1X} = 0.0$ A to 3.65 μm at $I_{QS1X} = 3.0$ A.

The contribution from dispersion was measured as 3.0 ± 0.7 μm using BPMs. Changing the skew quadrupoles could have changed the focus position slightly. A further quad scan could have confirmed this but due to time constraints this was not possible.

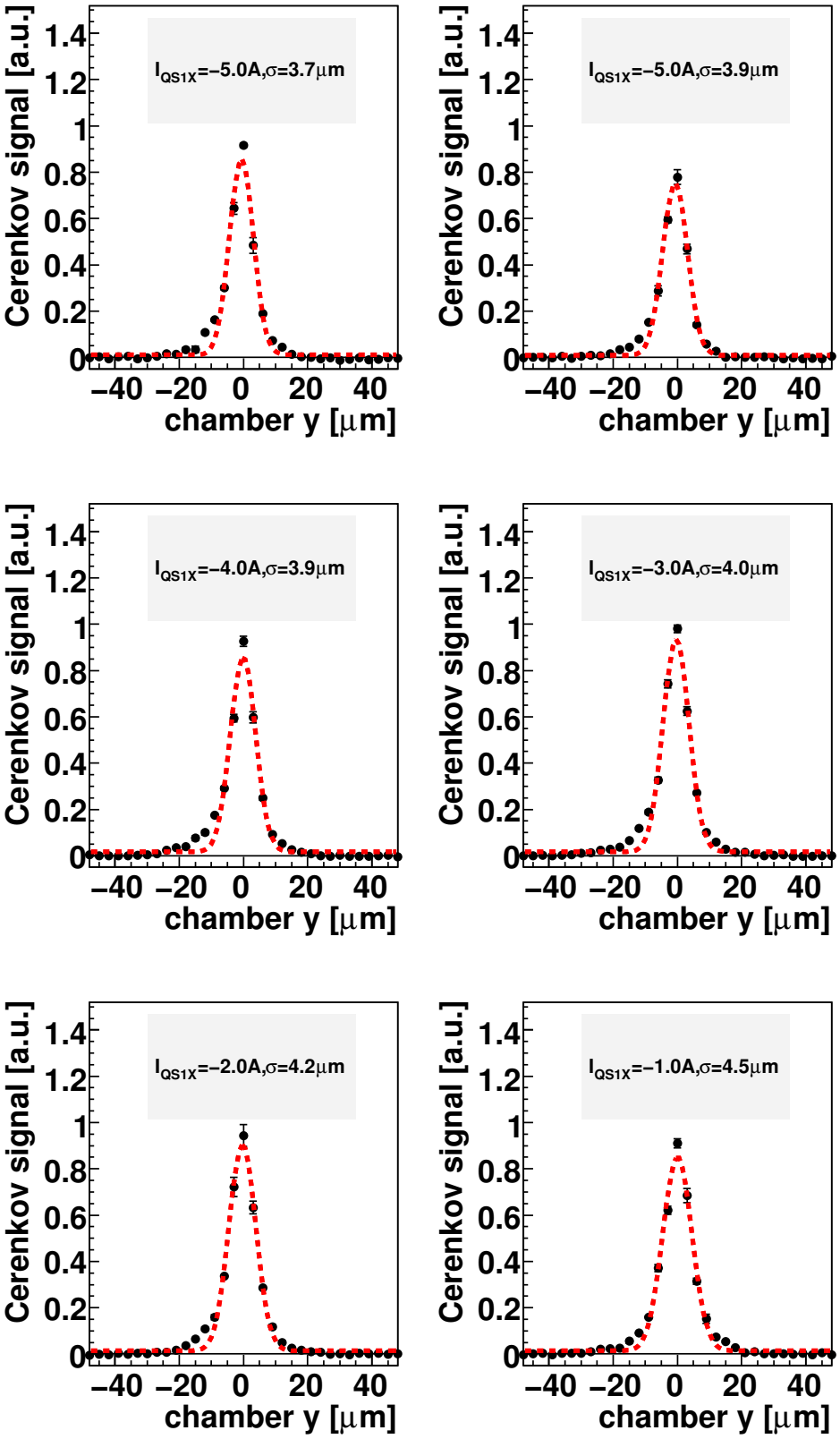

Figure 4.36: QS1X skew quad scan 23/05/08, part 1. QD4X set to 74.06 A. The black dots are data. The red lines are Gaussian + constant fits.

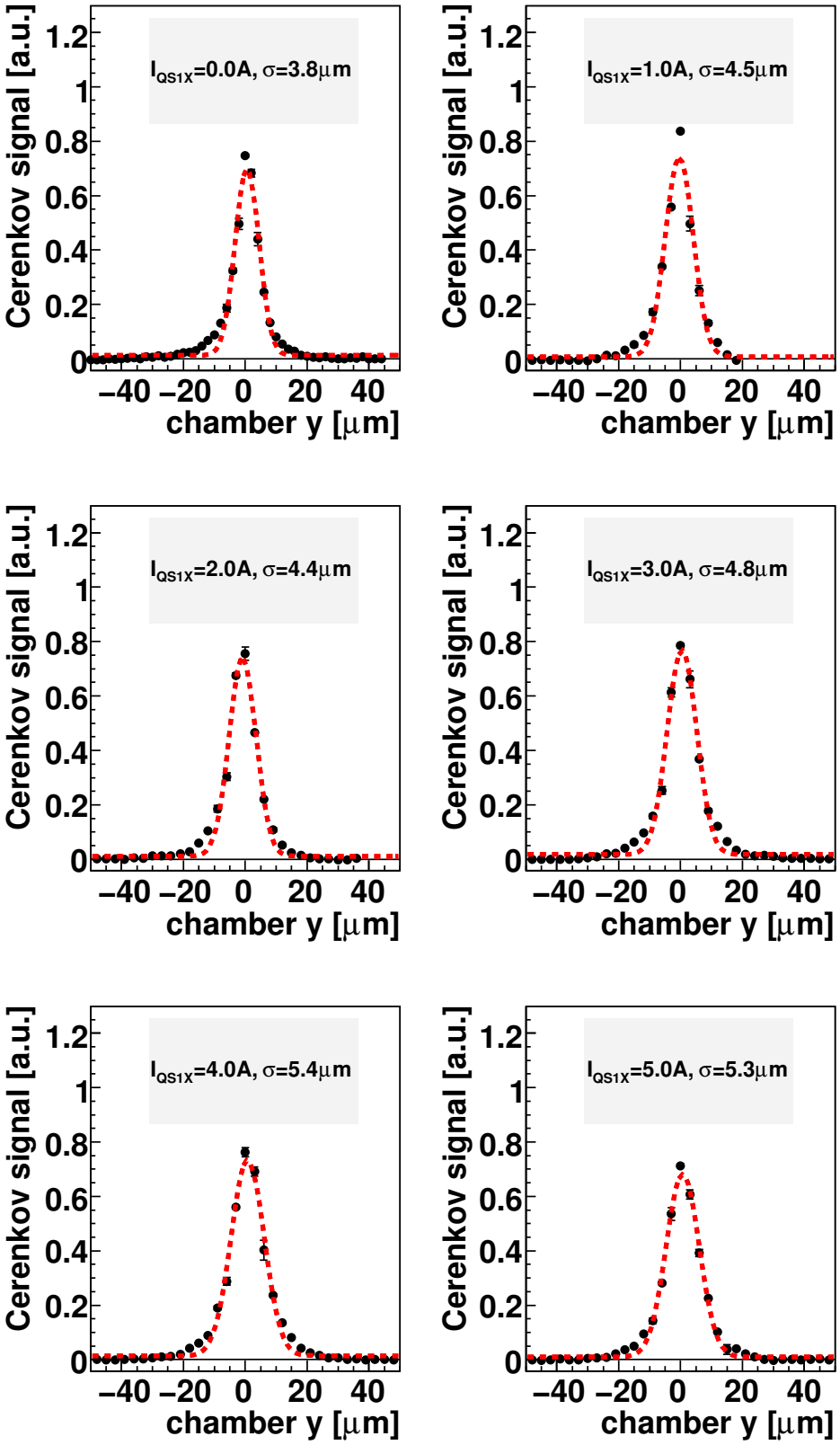

Figure 4.37: QS1X skew quad scan 23/05/08, part 2. QD4X set to 74.06 A. The black dots are data. The red lines are Gaussian + constant fits.

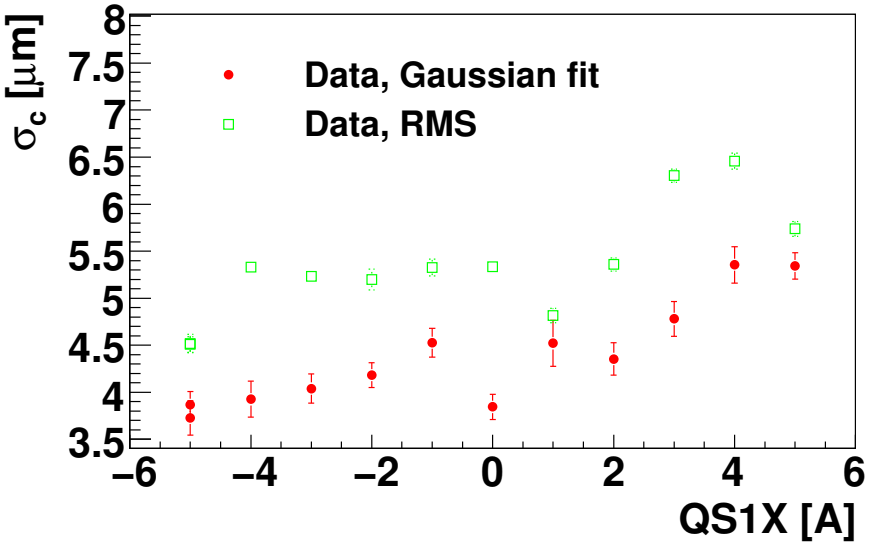

Figure 4.38: QS1X skew quad scan 23/05/08. QD4X set to 74.06 A.

4.5.7 Emittance Measurement Using Laser-Wire

Data from a quad scan fit (Fig. 4.45), dispersion measurement (Sec. 4.4.3) and laser profiling (Sec. 4.3.2) is combined to produce an emittance measurement.

The contribution to σ_C from the laser and dispersion is given by $\sigma_{\mathrm{D+lw}} = \sqrt{\sigma_{\mathrm{D}}^2 + \sigma_{\mathrm{lw}}^2} = \sqrt{3.03^2 + 2.1^2}\ \mu$m$= 3.69\ \mu$m. This value of σ_D comes from the dispersion measurements (Sec. 4.4.3) and σ_{lw} is from the laser measurements (Sec. 4.3). The error propagation is calculated in the following way. The contributions to the size due to dispersion and laser wire add in quadrature:

$$\sigma_{\mathrm{D+lw}} = \sqrt{\sigma_{\mathrm{D}}^2 + \sigma_{\mathrm{lw}}^2} \tag{4.22}$$

Then the error is given by

$$\Delta\sigma_{\mathrm{D+lw}}^2 = \left(\Delta\sigma_D \cdot \frac{\partial\sigma_{\mathrm{D+lw}}}{\partial\sigma_{\mathrm{D}}}\right)^2 + \left(\Delta\sigma_{lw} \cdot \frac{\partial\sigma_{\mathrm{D+lw}}}{\partial\sigma_{\mathrm{lw}}}\right)^2 \tag{4.23}$$

$$= (\Delta\sigma_D^2 \cdot \sigma_D^2 + \Delta\sigma_{lw}^2 \cdot \sigma_{lw}^2)\frac{1}{\sigma_{\mathrm{D+lw}}^2} \tag{4.24}$$

From the results $\sigma_{\mathrm{lw}} = 2.1 \pm 0.2\ \mu$m and $\sigma_D = 3.03 \pm 0.66\ \mu$m and using Eq. 4.24 we find that

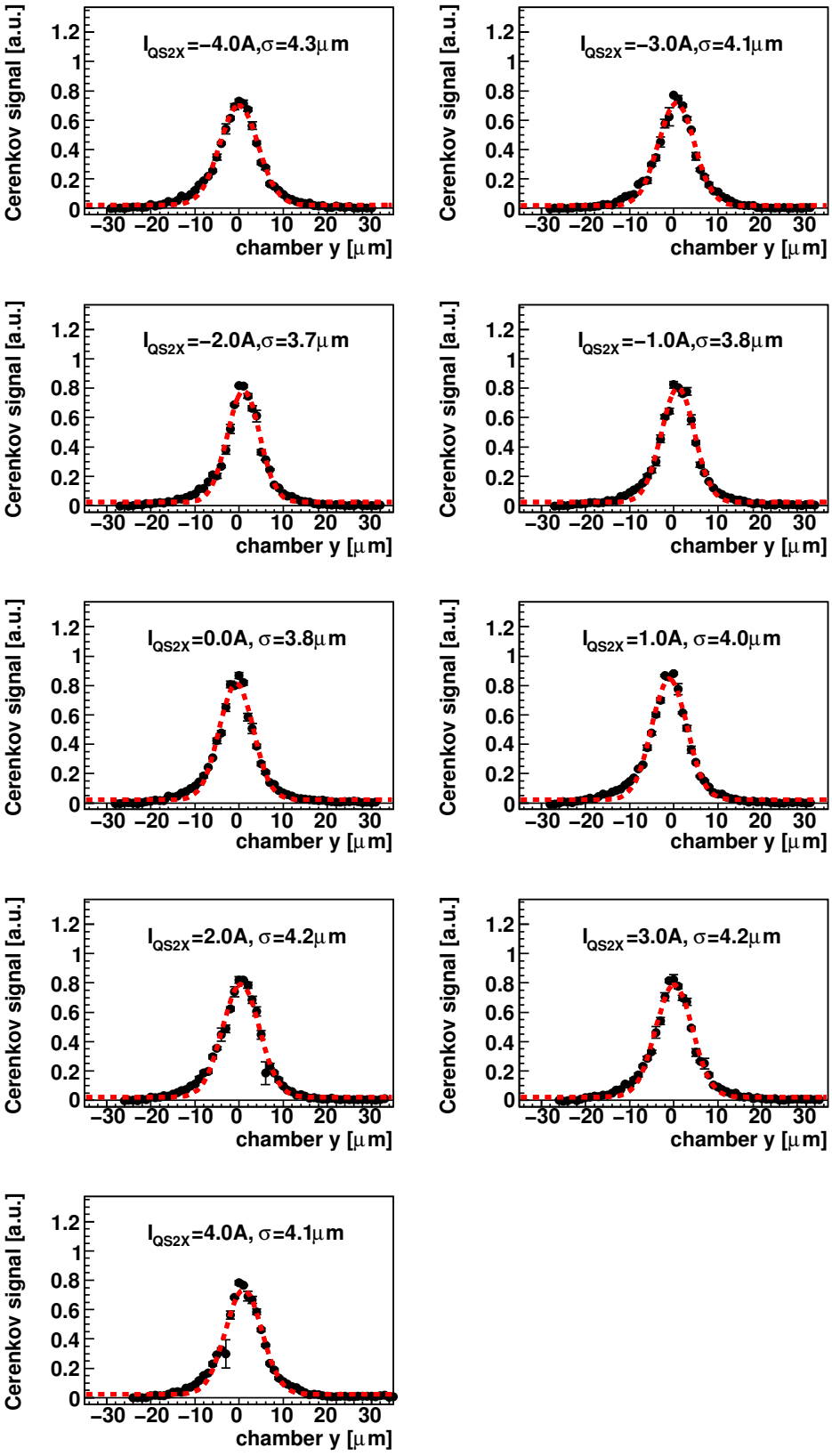

Figure 4.39: QS2X skew quad scan 23/05/08. QD4X set to 74.06 A. The black dots are data. The red lines are Gaussian + constant fits.

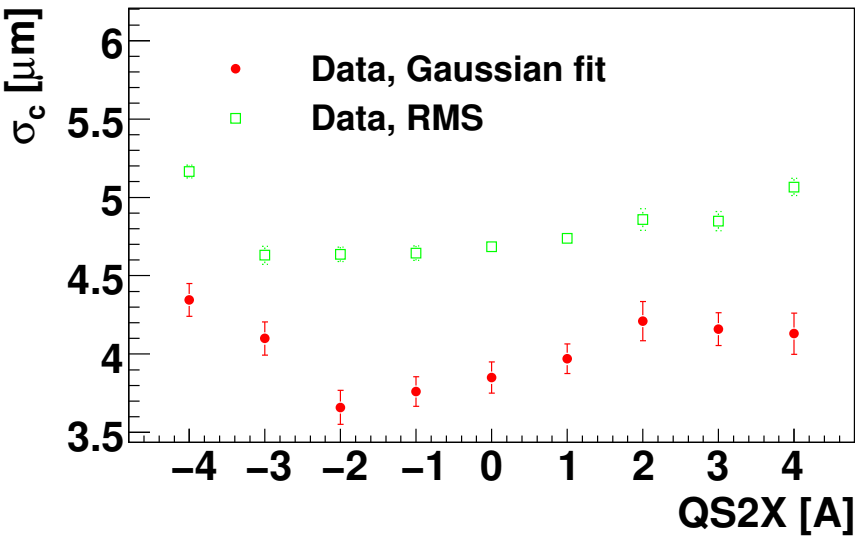

Figure 4.40: QS2X skew quad scan 23/05/08. QD4X set to 74.06 A. Markers as Fig. 4.33

$$\Delta\sigma^2_{\mathrm{D+lw}} = (0.66^2 \cdot 3.03^2 + 0.2^2 \cdot 2.1^2)\frac{1}{3.69^2} \quad (4.25)$$

$$\Delta\sigma_{\mathrm{D+lw}} = 0.55\ \mu\mathrm{m}, \quad (4.26)$$

so $\sigma_{\mathrm{D+lw}} = 3.69 \pm 0.55\ \mu$m.

An emittance measurement was performed using a double quad scan, where both I_{QD4X} and I_{QF4X} were changed, and this was accomplished during the same shift as the dispersion measurement, carried out on 29/05/08 (Fig. 4.44). Subtracting $\sigma_{D+\mathrm{lw}}$ in quadrature from each beam size measurement in the QUAD scan, the emittance was measured as 248^{+92}_{-174} pm, taking into account the above error on $\sigma_{\mathrm{D+lw}}$. The upper and lower values of ε come from subtracting the lower and upper values of $\sigma_{\mathrm{D+lw}}$ in quadrature from each beam size measurement before fitting. The highest value of $\sigma_{\mathrm{D+lw}}$ that could be subtracted was 4.18 μm - this was the minimum measured beam size. The result is in agreement with the wire scanner emittance measurement (Sec. 4.5.5) of 207 pm.

For a more accurate emittance measurement using the laser-wire, a higher resolution dispersion measurement is needed. However, the $\varepsilon = 248$ pm laser wire measurement and the 207 pm wire scanner measurement are $\sim$10 times the nominal value (measured in 2005, before collisions) needed to produce a 1 μm vertical electron beam size. This suggests that a lower

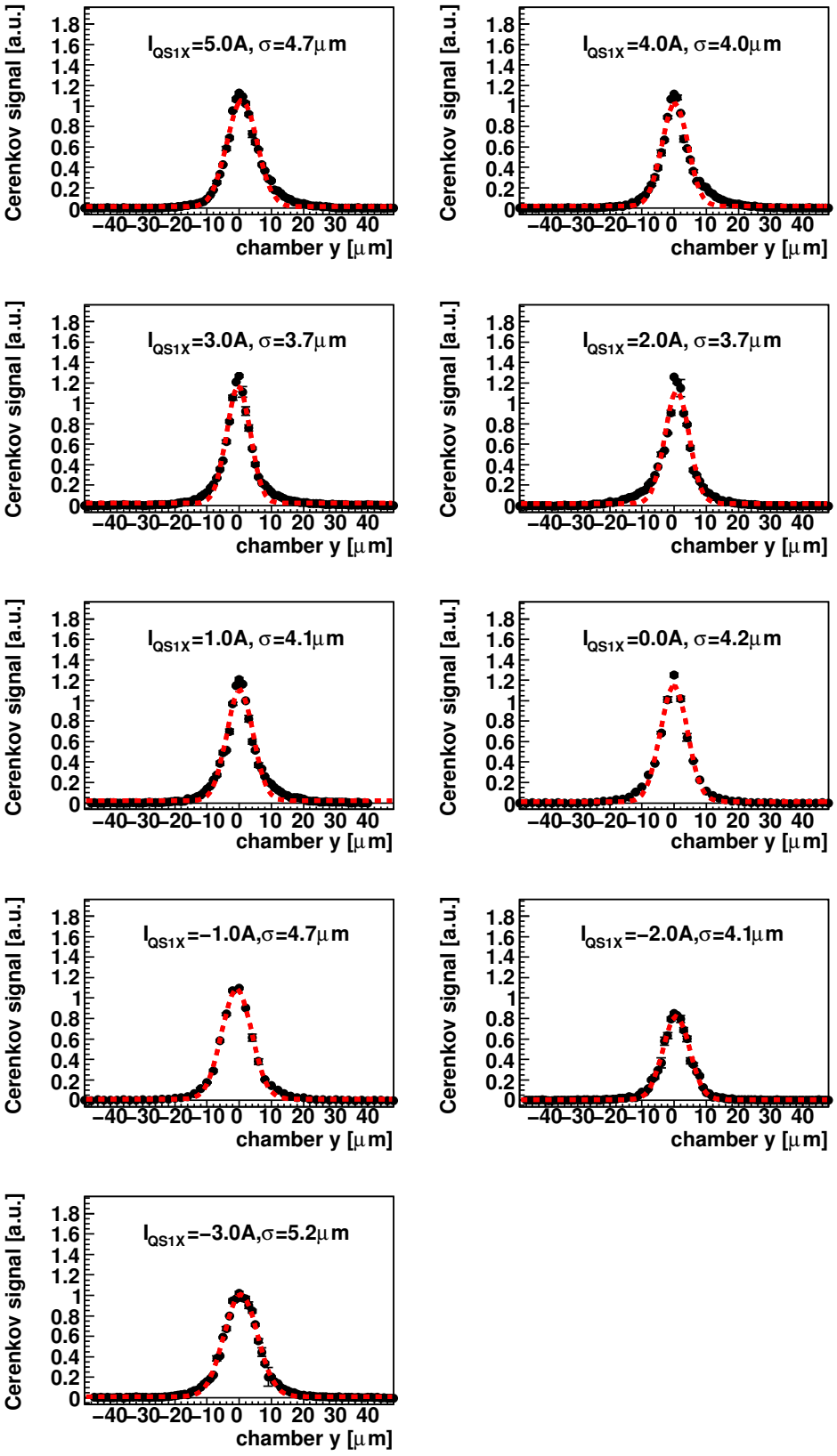

Figure 4.41: QS1X skew quad scan 29/05/08. QD4X set to 74.06 A. The black dots are data. The red lines are Gaussian + constant fits.

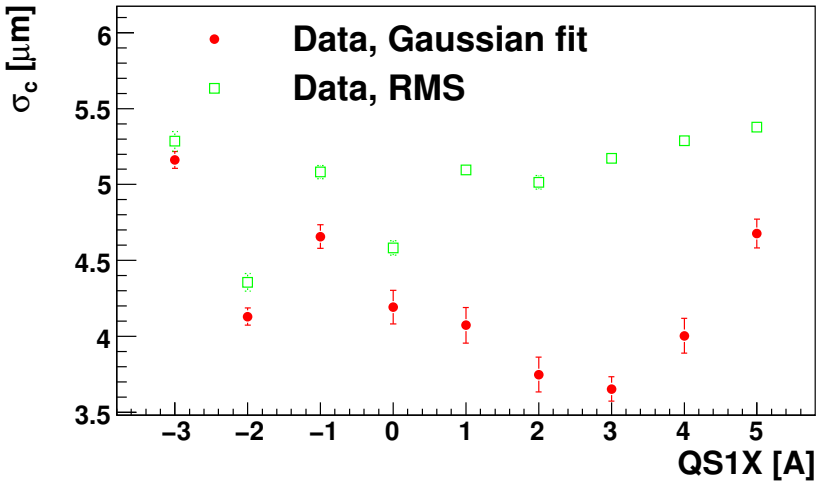

Figure 4.42: QS1X skew quad scan 29/05/08. QD4X set to 74.06 A. The reason for the outlier at −2 A is unknown.

emittance electron beam is required to verify the small laser-wire spot size.

Although dispersion measurements were not performed for every shift, for the time being the contribution to electron beam size due to dispersion, σ_D, is assumed to be 3.03 μm at all times.

σ_{lw} and σ_D were subtracted from each beam size and the data in Fig. 4.4 were fit to the function Eq. 4.19. An example fit is shown in Fig. 4.45.

Results of emittance measurements are shown in Tab. 4.14. The design emittance for ATF is 12 pm. More precise laser profiling will lead directly to a more precise measurement of the emittance. However, this study, along with the wire scanner emittance measurements, show that the ATF emittance at the time all these measurements were performed was not optimal. On the 29/05/08, when the dispersion was known, the simulated and measured data show good agreement. The values on the other dates are unclear because the dispersion was not measured.

4.6 Conclusions

Measurements were made to account for contributions to σ_c, the size of the convolution between the electron beam and laser beam, as measured during an electron beam measurement using a laser-wire scan.

Contributions to the electron beam size are from the emittance, and from the dispersion.

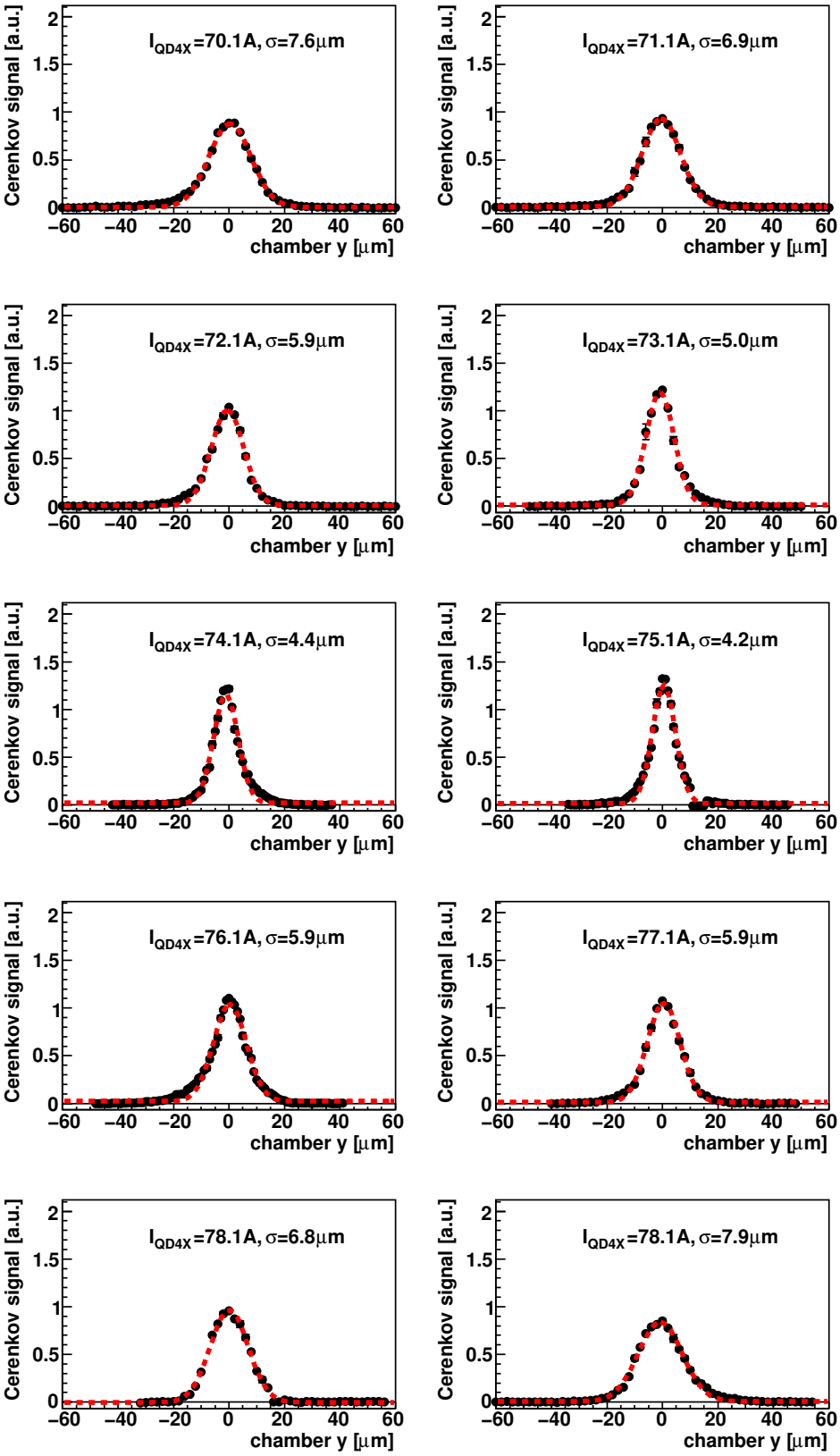

Figure 4.43: 29/05/08: QD4X scan. The black dots are data. The red lines are Gaussian + constant fits.

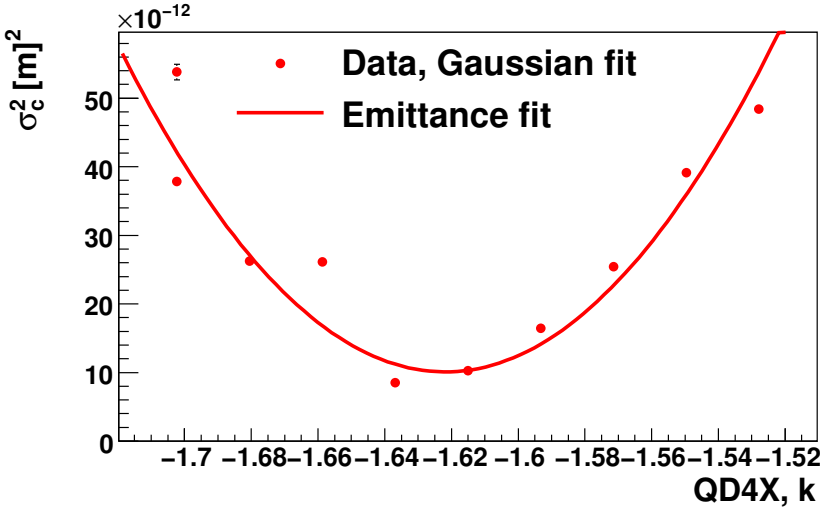

Figure 4.44: 29/05/08: QD4X/QF4X laser-wire scan with emittance fit. Plotted is the QD4X k value versus σ_e^2. The fit function is Eq. 4.18, with S_{11} and S_{12} as Eqs. 4.20 and 4.21.

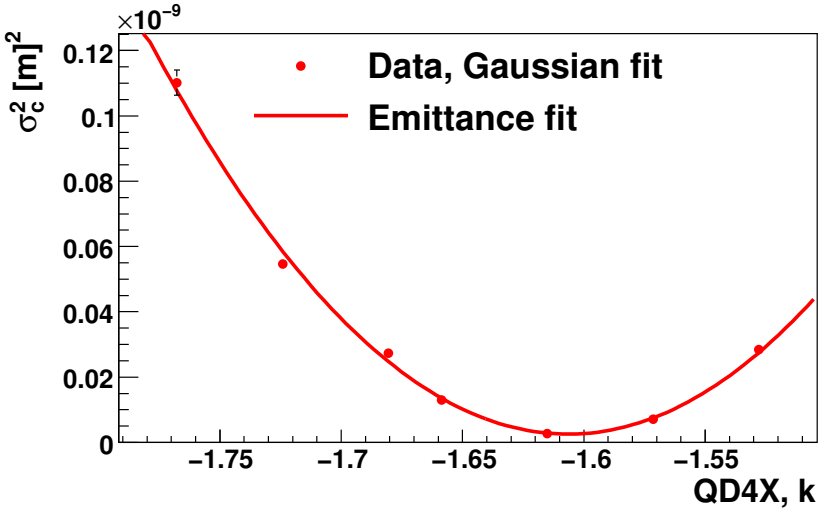

Figure 4.45: QD4X k value versus σ_e^2, as measured by the laser-wire. The fit function is Eq. 4.19

Date	ε [pm]	σ_e [μm] (sim.)	σ_e [μm] (lw)
20/02/2008	862 ± 5	2.63	3.96
18/04/2008	1680 ± 30	7.44	6.28
22/05/2008	69 ± 4	1.5090	1.9
29/05/2008	248^{+92}_{-174}	$1.41^{+1.65}_{-0.64}$ μm	$1.97^{+0.80}_{-0.46}$

Table 4.14: A summary of emittance measurements performed using the custom lens system. σ_C was calculated using Gaussian + constant fits. Vertical electron beam size due to dispersion, $\sigma_D = 3.03 \pm 0.66$ μm and $\sigma_{\rm lw} = 2.1 \pm 0.2$ μm are subtracted in quadrature from the σ_cs in the analysis. The error in ε is the statistical error and does not take into account systematic error in the dispersion measurement and measurement of $\sigma_{\rm lw}$. Also shown is the estimated minimum beam size, and the minimum beam size measured by the laser-wire, again with $\sigma_{\rm lw}$ and σ_D subtracted in quadrature. Note that the dispersion was only measured on 29/05/2008. There is likely to be variation in dispersion between shifts due to the fact that the beam orbit in the extraction line has to be retuned each time. Therefore, the only reliable emittance measurement quoted here is from 29/05/2008. The full systematic error for this measurement is included. The quoted σ_e [μm] (lw) on the 29/05/2008 is after skew quadrupole tuning, with the estimated $\sigma_{\rm lw}$ (2.1 ± 0.2 μm) subtracted in quadrature.

Factors contributing to the laser beam size include the input beam size on the lens, and the M^2 laser quality factor. Simulations and measurements indicate that the lens introduces spherical aberrations above a certain input beam size (Sec. 4.3.1) and these affect the quality of the laser; a input laser beam with $M^2_{\rm in} = 1$ may have a greater M^2 downstream of the lens. We define $\sqrt{(M^2_{\rm lens})^2 + (M^2_{\rm in})^2} = M^2_{\rm final}$. The dominating error in the estimation of the final focus laser beam size, $\sigma_{\rm lw}$, come from the error in the measurement of the input beam size. Simulations and measurements predict that $\sigma_{\rm lw} < 1$ μm could be achieved by reducing the input beam size (Fig. 4.4).

The maximum contribution to beam size from a simple astigmatism is small (< 0.1 μm). The full effects of general astigmatism will be of a similar order, given the measured size of the imaginary part of the rotation angle. Therefore, the contribution to beam size from general astigmatism is neglected.

The smallest convoluted beam size, σ_c, was measured after skew quadrupole tuning, was measured as 3.65 ± 0.09 μm.

Using various measurements and models the laser beam size was estimated to be $\sigma_{\rm lw} = 2.1 \pm 0.2$ μm. Therefore the minimum measured electron beam size was 2.91 ± 0.15 μm (Tab. 4.14).

After measuring the dispersion a contribution to the vertical electron beam size due to vertical dispersion was found to be 3.03 ± 0.66 μm.

Using all the above information the electron beam emittance in the ATF extraction line was

measured as 248^{+92}_{-174} pm using the laser-wire. The design value of ε_y for ATF is 12 pm in the damping ring, and this increases in the extraction line to ~ 3 times this value, but a value of 207 pm was measured on the previous month using a wire scanner, confirming our laser-wire measurement.

These measurements should be done with an input laser beam size of $W_{\text{in}} = 6$ mm (Fig. 4.5), which will allow us to achieve an even smaller spot size. High power fibre lasers are being developed [42] which should be able to produce high power, high quality beams. The dispersion should be removed before performing attempting an emittance measurement.

To verify that the remaining contribution to σ_c is due to a large emittance beam may require an independent emittance measurement simultaneously with the laser-wire emittance measurement, along with dispersion correction and measurements, during a single data taking shift. The emittance at ATF2 [2, 3] is expected to be smaller and more stable.

Chapter 5

Halo Measurement

The distribution of electrons in the ATF beam is not a perfect Gaussian. Instead, it has a main "core" with non-Gaussian tails at the sides. This could be caused by imperfections in the magnetic fields or by scattering from residual gas in the vacuum beam pipe and this could cause a problem with backgrounds at ATF2 [2, 3], particularly in the Shintake monitor [43] which is located after the final focusing magnets. Electrons in the halo far off axis could cause intolerable background in the Shintake monitor's photon detector due to the strong focusing of the final focusing magnets causing a large acceleration, which will generate SR. Also, the beam becomes rather large before the final focus section so there could be a lot of bremsstrahlung radiation emitted due to halo particles hitting the beam pipe, magnets and other materials. This problem was simulated using BDSIM [37].

Before this could be simulated using BDSIM the halo distribution needed to be known so that it could be modelled accurately. The halo distribution and relative population compared to the core would need to be known. Therefore, wire scanner measurements of the beam halo and core were taken. Since the halo population is so small compared to the core population a novel method of measurement was required. The Shintake monitor group attempted this: they measured a tail "connected" to the main Gaussian core at 3 or 4 σ, where σ is the Gaussian σ of the core and estimated the tail as a a N_{σ}^{3} or N_{σ}^{4} power law distribution.

5.1 Linearity of Hamamatsu R877 Photomultiplier Tube

Pulse linearity is defined as "the proportionality between the input light amount and the output current in the pulse operation mode". For the Hamamatsu R877 photomultiplier tube (PMT) this is $\pm 2\%$ at 10 mA and $\pm 5\%$ at 20 mA. This linearity is defined in the following way: a pulsed light source is introduced to produce a 10 mA or 20 mA signal. The power of this light source is then halved. The difference between twice the halved signal output 10 mA (or 20 mA) divided by 10 mA (or 20 mA) is the linearity. By plotting the output current vs the PMT counts for the experimental conditions in which the data were taken, it is possible to determine how much of the data were taken within a linear operating range.

The typical operating voltage of 1250 V was used. At this value, the gain is 5.0×10^5 volts.

The analog to digital converter was a Hoshin C009H where the final H stands for "high resolution" so it has 14 bits instead of 12. It is a charge integrating device.

Tests were conducted to measure the linearity of the PMT across the range of output voltages where data were taken, as discussed in the next section.

5.1.1 Linearity Tests

The photomultiplier tube was placed in a light tight box and illuminated by an LED. The LED was positioned at the end of the same periscope used in the halo measurements and the square wave pulse length was set to 22 ns. The light pulses from the LED are shorter than this due to their finite rise time. The light pulse from Cerenkov radiation during the halo measurements was approximately equal to the bunch length, ~ 50 ps. However, the output pulse length of the PMT is ~ 100 ns. Therefore, light pulses shorter than 100 ns are adequate to approximate the experimental conditions. This was confirmed by the fact that the output pulse widths on the scope trace (Fig. 5.1) for the pulsed LED and beam interaction pulses were the same. The LED was connected in parallel to a pulse generator operating at the ATF normal bunch frequency of 1.57 Hz. The light output of the LED was changed by changing the input pulse voltage and pulse length. The light output of the LED was calculated as $O \propto VP$ where $V$is the voltage and P is the pulse length. Two configurations were used:

1. LED on
2. LED off (background)

Calculation of PMT Output from Attenuation and ADC Counts

In amplitude, voltage and current applications the decibel is defined as

$$O_1 = 10^{\frac{-R_{dB}}{20}} O_0 \tag{5.1}$$

where O_1 is the measured amplitude and O_0 is the reference amplitude. Therefore if O_0 is the number of ADC counts and R_{dB} is the attenuation in decibels then the PMT output measured in ADC counts is O_1.

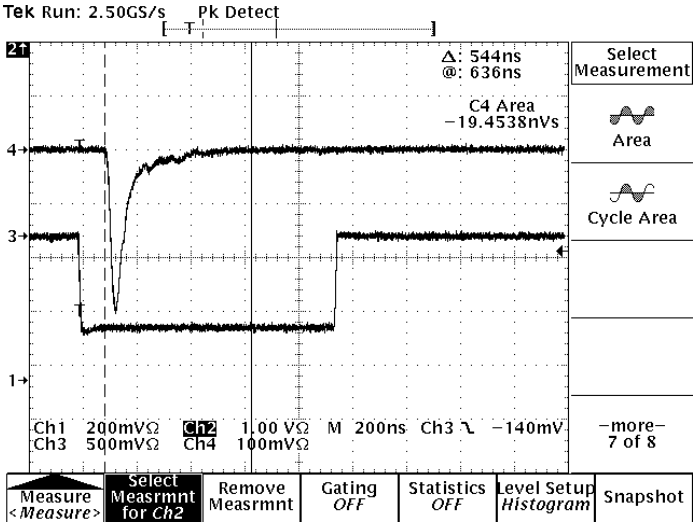

Figure 5.1: Gated signal of LED in scope trace. Amplitude = 300 mV, FWHM = 40 ns and area = −19.4538 nsV.

Linearity Test Across Range of Outputs Used in Halo Measurement

The experimental conditions of the halo measurements were recreated on the lab bench to verify the linearity of the PMT during those measurements. Therefore the voltage across the PMT dynodes was again set to 1250 V. The ADC was a 14 bit device so it can store $2^{14} = 16386$ unique values. The attenuation during the measurements was set to -21 dB. Therefore, in order to test linearity at the maximum in the signal range, the attenuation was set to -22 dB and the LED pulse generator voltage was adjusted until the output from the PMT was 90% of the maximum number in the ADC, or $0.9 \times 16836 \sim 14750$. Then the linearity test described was carried out.

Results of Linearity Test

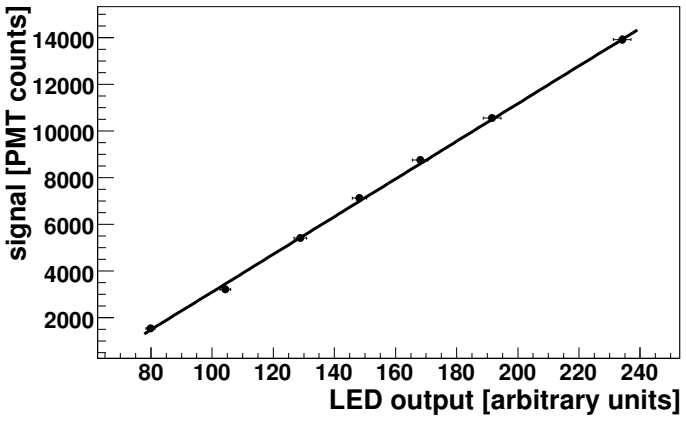

Figure 5.2: LED output vs. PMT output. $\chi^2/\text{NDF} = 38.3/5 = 7.66$ for the straight line fit.

The results are plotted in Fig. 5.2. The PMT signal is an average of 150 pulses and the uncertainty bars show the statistical uncertainties. These error bars are too small to be seen on this plot. The horizontal error bars are from the uncertainty in the voltage and pulse length settings of the LED. The results show that the PMT response is linear across the full range that was used (up to 8300 ADC counts).

5.2 Halo Measurement

In order to cover the full dynamic range across the beam profile, two detectors were installed. One was an air Cerenkov/PMT detector normally used for wire scanner measurements. The other was the lead/aerogel/PMT detector used in the laser-wire experiments, Chap. 3. These detectors were placed side by side and used simultaneously during a wire scan. The higher sensitivity aerogel detector caused ADC saturation as the wire crossed the beam core but the signal produced in this region was within the other detector's dynamic range. By overlaying the two sets of data a full profile was produced (Fig. 5.3). The data and fits are plotted again without the logarithmic scale in Fig. 5.5. A close up of the Gaussian fit is shown in Fig. 5.4.

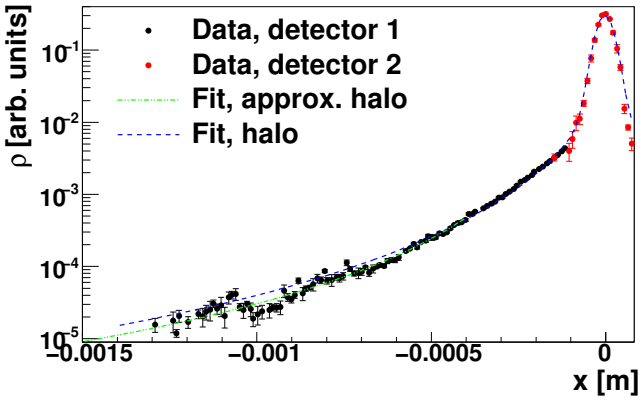

Figure 5.3: Measured beam distribution with fits to a Gaussian, Eq. 5.2 (halo fit) and Eq. 5.3. (approximate halo fit)

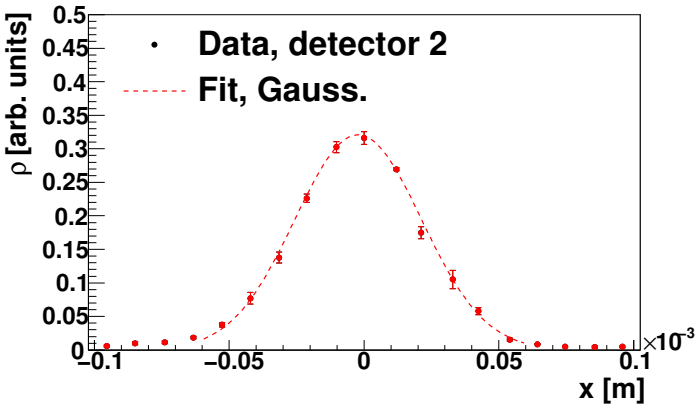

Figure 5.4: The Gaussian fit in Fig. 5.3

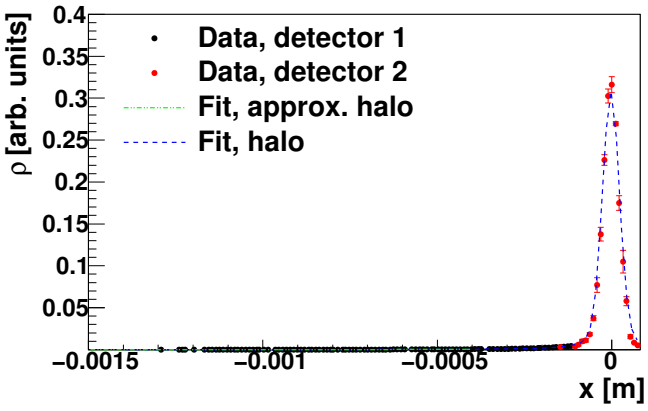

Figure 5.5: Fig. 5.3 plotted without the logarithmic scale.

5.2.1 Comparison with a Theory of Non Gaussian Beam Distributions Due to Gas Scattering

In [44] a theory of the non-Gaussian distribution of beams due to incoherent stochastic processes, such as collision with atoms in the residual gas, is presented. Here the theory is compared to the experimental data from Sec. 5.2. The full distribution is

$$\rho(X) = \frac{1}{\pi}\int_0^\infty dK \cos(KX) \exp\left[-\frac{1}{2}K^2 + N_d \frac{1}{\pi}\int_0^1 d\xi \frac{C\left(\frac{\theta_{min}}{\sigma_0'}\xi\right) - 1}{\xi}\cos^{-1}(\xi)\right] \tag{5.2}$$

which, in the limit of large X, becomes

$$\rho(X) \sim \frac{N_d \Theta^2}{16X^3}, (X \to \infty). \tag{5.3}$$

Here K and ξ are integration variables. $X = \frac{x}{\sigma_0}$ where x is the transverse displacement from the distribution centre (peak), and σ_0 and σ_0' are the nominal RMS size and angle in the damping ring. $N_d = Nd$ where N is the number of collisions per unit time and d is the damping time. $\Theta = \frac{\theta_{min}}{\sigma_0'}$ where θ_{min} is the minimum scattering angle of the electron from the gas molecule as dictated by the uncertainty principle, that is

$$\theta_{min} = Z^{1/3}\frac{\alpha}{\gamma} \tag{5.4}$$

where α here is the fine structure constant and $\gamma = \frac{E}{m_e c^2} = \frac{1.28\text{GeV}}{0.511\text{MeV}}$ is the relativistic Lorentz factor. C is given by

$$C(u) = uK_1(u) \tag{5.5}$$

where $K_1(u)$ is the modified Bessel function of the first order.

The number of collisions per unit time is

$$N = Q\sigma_{tot}c \tag{5.6}$$

where c is the speed of light, $Q = 2.65 \cdot 10^{20} P_a n$ and n is the number of atoms in the gas molecule and P_a is the partial pressure of the CO gas. The total scattering cross section, σ_{tot}, is

$$4\pi r_e^2 \frac{Z^2}{\gamma^2} \frac{1}{\theta_{min}^2}. \tag{5.7}$$

Here, r_e is the classical Bohr radius.

Eq. 5.2 is approximately Gaussian near the centre of the beam when N_d is small.

Name	Symbol	Value
Damping time [45]	d	$6.8 \cdot 10^{-3}$ s
Emittance (nominal)	ε_{nom}	10 pm
Average square root beta function in damping ring	$\sqrt{\beta}$	1.6 m
Relativistic Lorentz factor	γ	$2.51 \cdot 10^3$
Typical partial gas pressure	P_a	$1 \cdot 10^{-6}$Pa

Table 5.1: Quantities for ATF damping ring needed to calculate N_d and Θ.

From the values in Tab. 5.1 we calculate N_d and Θ. We also fit Eq. 5.2 to the full distribution and compare with the values predicted by the theory.

Using Eq. 5.6 we calculate N and use $N_d = Nd$ to calculate N_d, using the values in Tab. 5.1.

σ_0' is estimated using the average $\sqrt{\beta}$ and nominal damping ring emittance in Tab. 5.1 and the equation

$$\sigma_0' = \sqrt{\varepsilon \left(\frac{1+\alpha^2}{\beta} \right)} \tag{5.8}$$

using the measured σ_0 (Tab. 5.3). The results are shown in Tab. 5.2

Symbol	Value
N_d	$2.75 \cdot 10^{-2}$
σ_0'	$1.7 \cdot 10^{-3}$ mrad

Table 5.2: Calculated values for beam-gas scattering.

5.2.2 Data Analysis

First, the saturating points from the high sensitivity PMT were removed. Then the background + pedestal was fitted to and subtracted. This was done by fitting Eq. 5.3 + a constant value in the large X and then subtracting the constant value from the data.

As the population of the tail is very low, the central core of the beam in normal operating vacuum pressures is relatively unaffected and should remain a Gaussian [44]. This is confirmed by the fact that a Gaussian function was fitted to the $\pm 3\sigma$ region with $\frac{\chi^2}{\text{NDF}} = 14.31/8 = 1.79$.

In contrast, if the whole function is fitted to a Gaussian then $\frac{\chi^2}{\mathrm{NDF}} = 6.143 * 10^4/180 = 341$. The results of the core fit are shown in Tab. 5.3.

Parameter	Value	Uncertainty
σ_0 (Gaussian RMS)	23.5 μm	0.3 μm
x_0 (centroid)	-2.1 μm	0.3 μm

Table 5.3: Results of Gaussian fit to the electron beam core (Fig. 5.3)

The data from the high sensitivity detector, from which the peak is missing due to ADC saturation, was spliced with the data from the low sensitivity detector, which lacks information about the tails of the distribution. This was done by scaling data from one set of data until several points overlapped to within $1\sigma_{\mathrm{RMS}}$. Thus the full profile was reconstructed. The uncertainty in this scaling is less than 1%. Fig. 5.3 shows the profile on a logarithmic scale. The measurements were taken simultaneously and therefore correspond to identical measurements at the points where the two sets of data overlap. Any points with PMT value less than 5 times the RMS PMT signal with zero beam current are considered background and are rejected.

The amplitude of the resulting distribution was normalised to the peak value of Eq. 5.2 for comparison with the theory presented in [44]. In the halo fit functions, the values of σ_0 and x_0 (the beam centre or peak) were fixed to be the same as those of the central Gaussian fit. θ_{min} was also fixed to the calculated value. σ_0' and N_d were free parameters.

Eq. 5.3 was fit to the tail of the distribution, from $-\infty$ to $-300\mu\mathrm{m} = 13\sigma_0$ and had $\frac{\chi^2}{\mathrm{NDF}} = \frac{405}{85} = 4.77$. This fit function gave the value of $N_d\Theta^2 = N_d\frac{\theta_{min}^2}{\sigma_0^2}$ which we now call η. This was used to calculate the starting value of N_d in the fit of Eq. 5.2.If we extend the function any closer to the beam core then this χ^2 value rapidly blows up, so the approximation in Eq. 5.3 rapidly becomes less valid for distances from the beam centre of less than $\sim 13\sigma_0$.

Using the σ_0 from the Gaussian fit to the core of the beam, this function was fit to the full distribution data, scaled by a normalisation constant. As expected, this fit agrees with the fit to Eq. 5.3 for large displacement X.

Eq. 5.2 (Fig. 5.3) has $\chi^2/\mathrm{NDF} = 18$. The fit results are shown in Tab. 5.4.

Parameter	Value	Uncertainty
θ_{min}	$5.59 \cdot 10^{-3}$ mrad	fixed
σ'_0	$3.28 \cdot 10^{-4}$ mrad	$0.02 \cdot 10^{-4}$
N_d	0.905	0.006

Table 5.4: The result of the fit of Eq. 5.2 to the data, Fig. 5.3

5.3 Conclusions

Comparing the fit values, Tab. 5.4, to the calculated values, Tab. 5.2, we see that N_d is 7.5 times larger in the fit and σ'_0 is about 5 times smaller in the fit, assuming 10 pm damping ring emittance. These do not seem like reasonable values. Also, the fit of Eq. 5.2 to the data is not very good. The calculated values are estimates. For a more precise comparison with the theory [44], more data is required, such as emittance measurements, Twiss parameter measurements, gas pressure measurements and gas composition in the damping ring. How sensitive the plot of Eq. 5.2 is to the fit parameters is unknown and is left as a future study. How the distribution is modified via the kicker between the damping ring and the extraction line also needs to be better understood.

Chapter 6

Simulations for the ATF and ILC Laser-Wires

6.1 BDSIM

BDSIM is a Geant4 [46] extension toolkit for simulation of particle transport in accelerator beam lines. It can simulate both particle transport through beam lines and secondary particles from various physics processes when particles hit apertures such as the beam pipe or the pole pieces of a magnet.

Dispersion was included in the simulated distributions as the distribution had an energy spread. Quadrupoles were assumed to have perfectly aligned rotation angles, so there was no *x-y* coupling. This could be included by giving the quadrupoles different rotation angles.

In order to provide a more realistic simulation improvements were made to the existing source code. Firstly, the way the initial particle distribution is generated was changed. In the original code bunches were defined in terms of the widths of Gaussian distributions in the horizontal and vertical plane in position and momentum space and energy. The position and momentum distributions were uncoupled. The code was modified to define the distribution in terms of the Twiss parameters (Eqs. 2.19, 2.20, 2.21). Therefore the particle distribution was defined, including a coupling term between position and transverse momentum (α, Eq. 2.19).

Second, the geometry of the quadrupoles and dipoles was changed to make them more realistic. In the original code the geometry of all the magnets was a simple cylinder with the beam pipe going through its central axis. Fig. 6.2 shows the modified quadrupole. There are "pockets"

between the pole pieces. These pockets allow particles from, for example, a laser-wire signal or background due to Bremsstrahlung and synchrotron radiation to to pass through (Fig. 6.1). The horizontal dipole geometry was changed to better match a real dipole, with two blocks of iron, one on either side of the beam pipe. The beam pipe in the dipole is rectangular, with the horizontal dimension twice the normal beam pipe diameter.

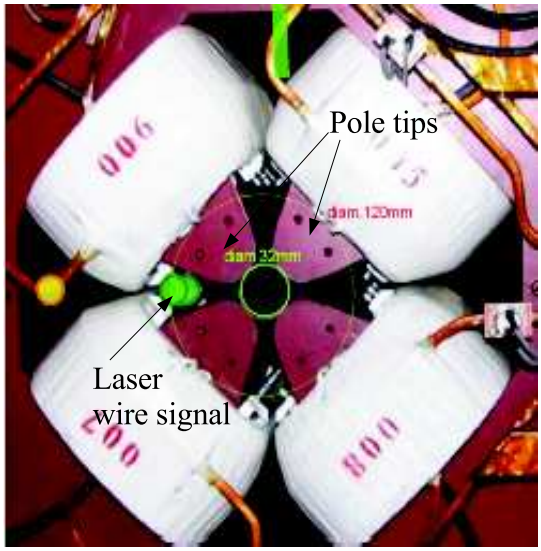

Figure 6.1: A picture of quadrupole QD6 showing the pole tips and the laser-wire signal.

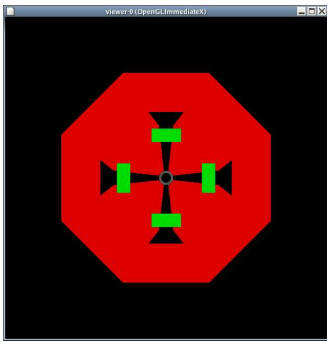

Figure 6.2: A quadrupole geometry

6.2 Simulation of ATF Laser-Wire Using BDSIM

6.2.1 Signal Extraction at ATF

The γ_{lw} were generated at the LWIP by generating a sample of electrons from the Twiss parameters, calculated using MAD [9, 10, 11]. An inverse Compton scattering event was simulated

for each electron using the method described in [15]. The photons were then tracked along the beam line to the detector. Scattering processes were simulated in the various materials between the LWIP and the detector. The γ_{lw} beam passes through a 0.5 mm exit window and 10 m of air before hitting the 7.35 mm lead plate at the front of the detector. The lead plate serves to convert a fraction of the γ_{lw} into electrons and positrons, which are detectable by the Cerenkov detector as detailed in Sec. 3.3.4. The position and trajectory of these electrons and positrons after the lead converter is shown in Figs. 6.3 and 6.4. They show that most of the electrons are travelling forward through the centre of the detector.

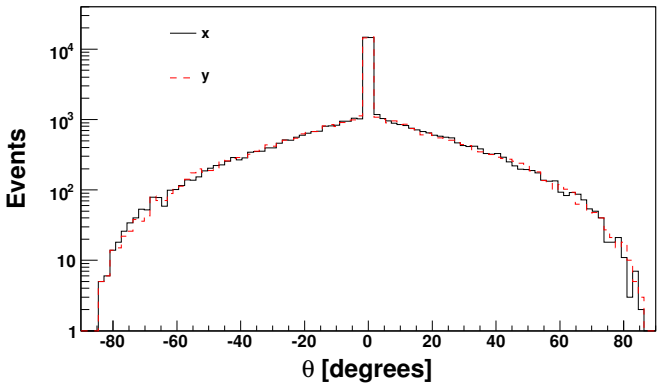

Figure 6.3: Electron and positron angles from normal to the detector surface after photon scattering in the lead converter.

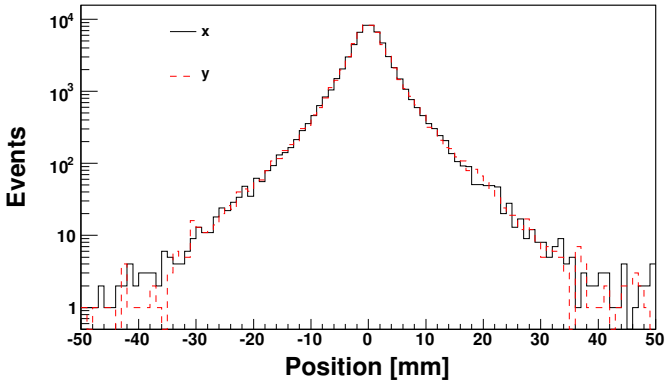

Figure 6.4: Electron and positron positions after γ conversions in the lead converter.

The energies of the particles hitting the lead converter, and the corresponding energies of electrons and positrons after the lead converter, are shown in Fig. 6.5. The ratio of electrons

and positrons above the Cerenkov threshold, shown by the vertical line at 2.983 MeV, after the converter to γ_{lw} at the LWIP is 0.14. The Cerenkov threshold serves to filter out the low energy backgrounds from SR and Bremsstrahlung, increasing the signal to noise ratio as compared to the calorimeter, as verified experimentally (Sec. 3.5).

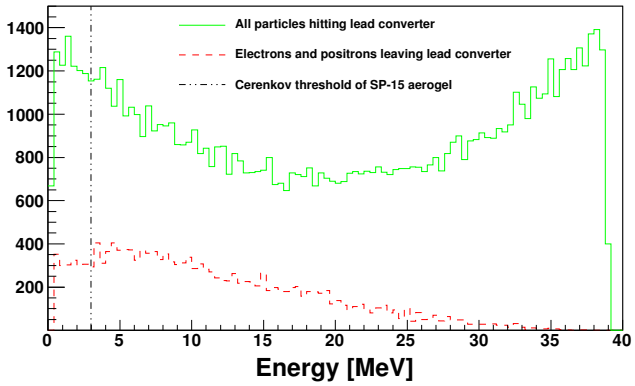

Figure 6.5: Electron and positron energies after lead converter.

6.2.2 ATF Detector Conversion Efficiency

The beam line from the laser-wire IP to the detector was simulated. The Compton scattered photon spectrum is shown in (Fig. 6.5) The simulation showed that the conversion efficiency was 14% (Sec. 6.2). This is the number of forward travelling charged (electrons and positrons) particles with energy above the Cerenkov threshold in the detector as a percentage of the initial number of Compton scattered photons.

6.2.3 Signal Extraction at ATF2

ATF2 [2, 3] is an upgrade of the ATF extraction line. It aims to achieve the small spot size and beam stability required for the ILC. It will also be used as a testing ground for technology such as the laser-wire.

The design of ATF2 [2, 3] presents a new challenge for a laser-wire installation because, unlike in the original extraction line, there is no convenient dipole directly downstream of the laser-wire IP to aid in separating the charged and neutral beams. Instead, there is a dipole further downstream (B5FF). The bending angle of this dipole is smaller than the dipole in the original

extraction line (BH4X) so the charged and neutral beams separate at a slower rate. This means that the neutral beam does not completely clear the magnets, although it can pass between the pole pieces of quadrupole QD6FF. To detect the signal further downstream than sextupole SF5 the magnet would have to be modified. A hole would have to be drilled in the magnet yoke and this could adversely affect the magnetic field. Simulations were carried out to determine the level of signal that would reach the possible detector locations (Fig. 6.6).

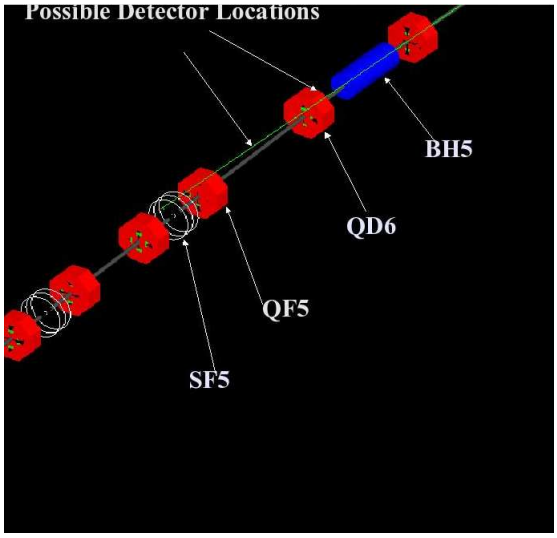

Figure 6.6: A screen shot from BDSIM with quadrupoles in red, a dipole in blue and sextupoles in white. The green line is the trajectory of a photon.

The first possible detector location was directly after the dipole B5FF, where the laser-wire signal separates from the electron beam. The space available is 55 cm. The laser-wire signal here is between 2 and 5 cm from the beam line. A Cerenkov detector will be able to fit in here if the emitted Cerenkov light is reflected away from the beam line using mirrors into the photomultiplier tube. However, a calorimeter may not because they must have a radius of between 2 and 4 cm due to the Moliére radius of the showering particles. This restricts the choice of detector at this location to a Cerenkov detector.

The second possible location is between the quadrupoles QD6 and QF5. The signal must pass between the pole tips of the quadrupole. The current ATF quadrupoles have bolt heads between the pole tips which would block the signal so they will have to be shortened. Bolt heads were not included in the model.

The space available at this location is 1.6 m. The signal will be 15 cm from the beam line so there is space for either a Cerenkov detector or a calorimeter. I have simulated the ATF2 [2, 3]

laser-wire using BDSIM (Fig. 6.7). At ATF2 [2, 3] the bending magnet where the electron beam and laser-wire signal separate will have a window in it to allow the laser-wire signal to exit the beam pipe. I have modelled this in the simulation by making the material of the beam pipe here a vacuum.

In the simulation the low energy cutoff for particle production processes is 1 MeV. The laser-wire is 532 nm with a spot size of 15 microns.

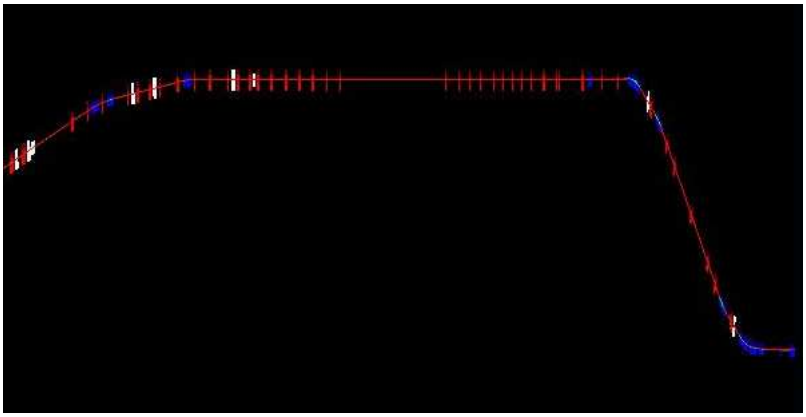

Figure 6.7: Simulation of the ATF2 extraction line using BDSIM.

At ATF2 [2, 3] there will be many high precision beam position monitors along the beam line, which are necessary in order to achieve the beam position stability and final focus beam size goals and have been included in the BDSIM simulation. Their apertures are narrower than the rest of the beam line. This affects the laser-wire photon signal which must propagate along the beam line for some distance before exiting the beam line after dipole B5FF.

Effect of IPBPM and laser-wire Detector Type and Location on laser-wire Signal

One of the narrow apertures is due to the IPBPM. The laser-wire signal diverges as it propagates, and it was predicted that the IPBPM in its original proposed location would cut out a large fraction of the laser-wire photon signal. I have shown using the simulation that relocating the IPBPM to a new position further upstream increases the transmitted laser-wire signal, in terms of the number of photons propagating, from 40% to 59%. In terms of energy, relocating the IPBPM increases the transmitted signal from 61% to 82%. Tab. 6.1 summarises the results.
The results show that it is preferable to detect the energy by putting a calorimeter before QD6. However, as already explained, this would be impracticable because the Moliére radius here is

	Original location	New location
$N_{\gamma\,\mathrm{LW}}$ at LWIP	45727 (100%)	45868 (100%)
$N_{\gamma\,\mathrm{LW}}$ before QD6	18438 (40%)	26685 (59%)
$N_{\gamma\,\mathrm{LW}}$ after QD6	18409 (40%)	25961 (57%)
$E_{\gamma\,\mathrm{LW}}$ at LWIP	$1.05 \cdot 10^3$ GeV (100%)	$1.05 \cdot 10^3$ GeV (100%)
$E_{\gamma\,\mathrm{LW}}$ before QD6	$6.37 \cdot 10^2$ GeV (61%)	$8.53 \cdot 10^2$ GeV (82%)
$E_{\gamma\,\mathrm{LW}}$ after QD6	$6.37 \cdot 10^2$ GeV (61%)	$8.31 \cdot 10^2$ GeV (79%)

Table 6.1: The effect of the IPBPM location on transmitted laser-wire signal. The N are the number of particles per bunch and the E are the sum of the particle energies per bunch.

greater than the distance between the laser-wire photon signal and the edge of the beam pipe. After QD6 the signal is almost as good. Furthermore, because the detector can be placed further from the beam pipe, it will see less background from synchrotron radiation and bremsstrahlung.

6.3 Simulations for ILC BDS laser-wires

In the current ILC baseline design, the laser-wire detectors and a machine protection system (MPS) collimator are located in the upstream polarimeter chicane. In terms of simultaneous laser-wire and polarimeter operation, this presents two main problems:

1. Is there interference in the polarimeter signal by the laser-wire and vice-versa?

2. Can the laser-wire signal be detected satisfactorily in this location?

The proposed detectors are Cerenkov detectors for reasons which will be explained. To detect the laser-wire Compton scattered photons, γ_C, they must first be converted to e^-e^+ pairs. These pairs will then propagate through the vacuum chamber depending on their energy and charge and will collide with the vacuum chamber walls producing showers. There are $\sim 10^4$ of γ_C and e_C^- with every bunch, and due to the nature of Compton scattering they are spread across a range of energies and trajectories.

Possible sources of background in the laser-wire detectors include synchrotron radiation (SR) from upstream magnets, beam gas bremsstrahlung and particles hitting the beam pipe. These problems are exacerbated by the fact that in the currently proposed location there is a direct line of sight along the linac, so more background photons from the linac and upstream in the BDS can propagate to the laser-wire detector than would be possible if the laser-wire were located downstream of a bend.

The BDS beam line was built according to the ILC2006e description [47]. A BDSIM visualisation of the BDS is shown in Fig. 6.9. The polarimeter chicane vacuum chamber was modelled according to design drawings [48] from solid boxes (G4Box in Geant 4) and trapezoids (G4Trap in Geant 4). A visualisation of a laser-wire event is shown in Fig. 6.10. In this figure is a closeup of the polarimeter chicane (also shown in Fig. 6.9). The chicane is viewed from above. The blue rectangles are dipoles. There are 12 dipoles arranged in sets of three. The red rectangles are quadrupoles. A laser wire Compton scattering event is shown. A Compton scattered electron (red track) and photon (green track) enter the chicane from the right. The electron trajectory is bent by the dipole fields. The photon hits a converter, which is a sheet of lead, located between the first and second dipoles in the the second triplet of dipoles, showers. The resulting particles (blue tracks are positrons) can be seen hitting various parts of the structure downstream and creating further showers. The polarimeter laser (not shown) is located near the centre of the chicane. There is a 2m $\times$ 1 cm 75 μm thick kapton window after the third dipole as a window to allow Compton scattered electrons to exit the vacuum chamber and enter the polarimeter detector. The chicane is a fixed field design with a 20 mm maximum dispersion at 250 GeV electron beam energy. The material of the vacuum chamber is steel and its vertical dimension is 20 mm. The chamber walls are 2 mm thick.

Included in the RDR design [26] is a machine protection system (MPS) collimator. Simulations of the laser-wire background on the polarimeter detector are done both with and without this collimator present. The collimator is a solid titanium alloy box (G4Box in Geant4 [46]) 3 m long by 1.2 m by 1.2 m with an aperture 2mm wide [49] at the horizontal position of the 250 GeV beam line (2mm). The concrete tunnel walls and surrounding earth are also included in the simulation, as particles could scatter off these walls into the beam pipe and detectors.

6.4 Initial Beam Conditions

A laser with wavelength 532 nm was simulated at the final laser-wire location in the manner described in [15]. For the 250 GeV ILC electron and the 532 nm laser-wire photons, the scattering angles in the electron rest frame are not well approximated using this Monte Carlo and the simulation could be made more accurate by using the full Compton differential cross section (see Sec. 2.3.4).

The fourth and final laser-wire is located 68.22 m from the start of the first dipole of the chicane (Fig. 6.8, from [26]). The Twiss parameters at the laser-wire interaction point are given in Tab. 6.2. This led to the γ_C distributions in Tab. 6.3. In a Compton scattering process $\sigma' \sim \frac{1}{\gamma}$, where γ is the relativistic coefficient. The σ' agree with this approximation.

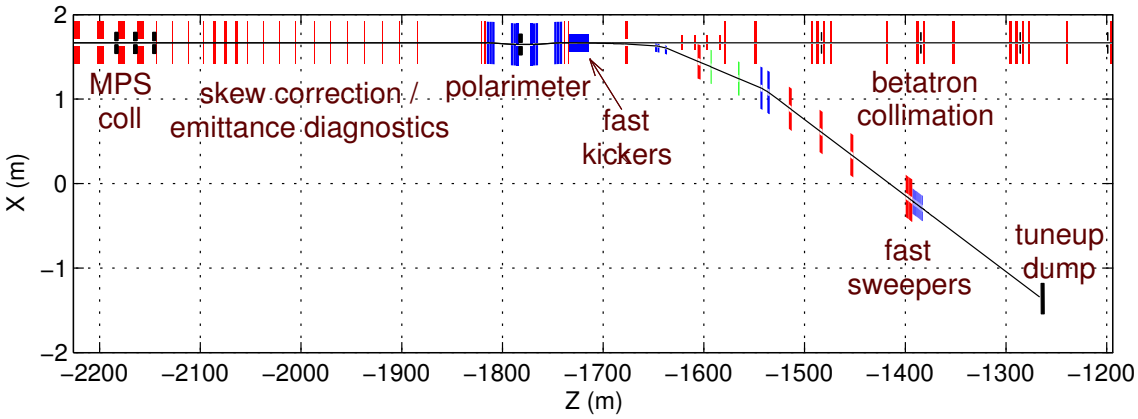

Figure 6.8: The first kilometre of the BDS layout showing functional subsystems, starting from the linac exit; X - horizontal position of elements, Z - distance measured from the e^+/e^- interaction point.

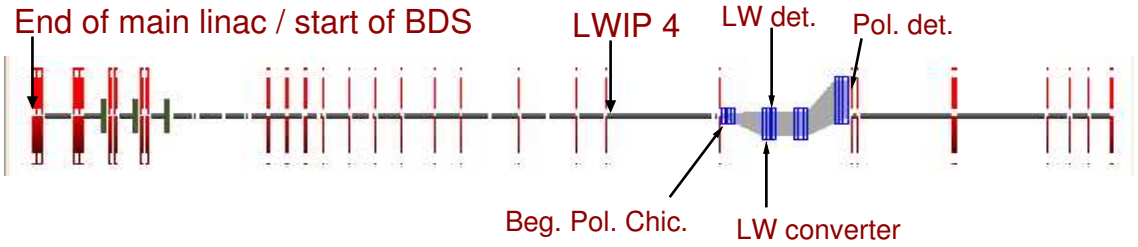

Figure 6.9: BDSIM screen shot of the first $\sim$ 600 m of the BDS layout, showing the locations of the fourth (final) laser-wire interaction point, the beginning of the polarimeter chicane a laser-wire γ_C converter and detector and the polarimeter detector.

	$\beta[m]$	α	$\sigma[\mu m]$	$\sigma'[rad]$
x	316.1	-3.813	76	$0.95 \cdot 10^{-6}$
y	72.78	-1.605	2.2	$0.58 \cdot 10^{-7}$

Table 6.2: Electron beam parameters at LWIP 4.

6.4.1 Detecting Laser-Wire Photons

The process of converting the laser-wire photons, along with the trajectory of the resulting electrons and positrons through the magnetic field, and into the Cerenkov detector was simulated

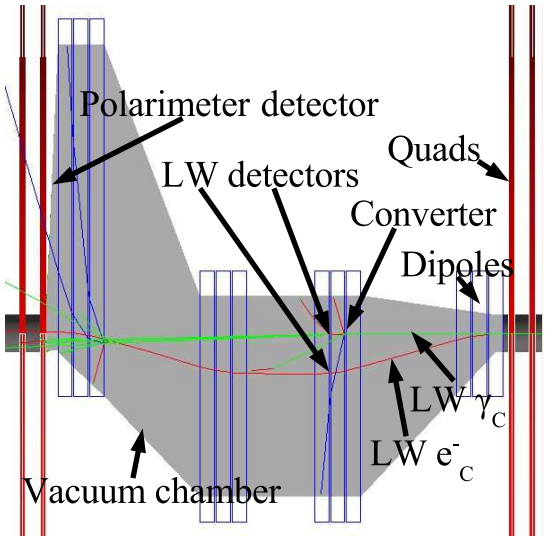

Figure 6.10: Visualisation of a laser-wire event. The Compton scattered photon (green) and electron (red) enter the image from the right (viewpoint reversed w.r.t. Figs. 6.8 and 6.9). The photon hits a lead converter and an electron and a positron (blue) appear by pair production. Further downstream, showering occurs in the vacuum chamber walls, beam pipe and magnets.

Location	s [m]	σ_x [μm]	σ'_x [rad]	σ_y [μm]	σ'_y [rad]
LWIP	0	76	$6.8.10^{-6}$	2.2	$6.9 \cdot 10^{-6}$
Beg. pol. chic.	68.22	380 $\pm$10		380 $\pm$10	
laser-wire converter	92.07	550 $\pm$10		550 $\pm$10	

Table 6.3: Simulated laser-wire γ_C parameters at various locations (see Fig. 6.8). s is the distance from LWIP 4. σ and σ' are the RMS position and RMS angle from the reference trajectory. σ_x and σ_y are each dominated by the $\sim 1/\gamma$ angular distribution of the Compton process, which explains why they have the same numerical values.

in BDSIM/GEANT4. The simulated electron and γ_C spectra are shown in Fig. 6.11. With increased thickness comes an increased probability of pair production. However, the probability of additional electromagnetic showering also increases. Some number N of electrons and positrons will be produced with every bunch. This number will vary from bunch to bunch by some standard deviation ΔN. $\Delta N/N$ is the relative bunch by bunch statistical fluctuation in N. Simulations were performed at different converter thicknesses (the material used was lead) with γ_C from a 250 GeV electron beam and $\Delta N/N$ was plotted as a function of lead thickness. An estimate of the optimum thickness, based on the results shown in Fig. 6.12, is 3.5 mm. A full simulation of the 3.5 mm conversion material in the vacuum chamber, with a magnetic field between the

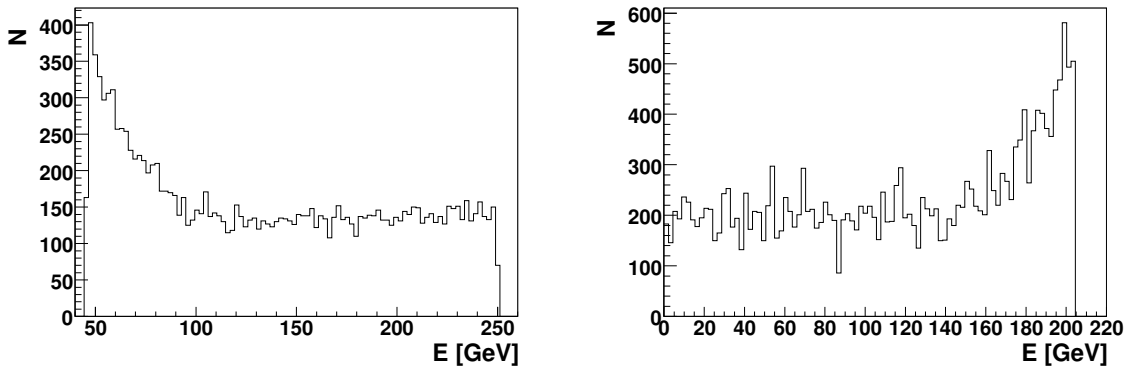

Figure 6.11: Shape of the energy spectrum with a 250 GeV e^- beam (the vertical axis is arbitrary). Left: e_C^-. Right: γ_C.

converter and the Cerenkov detector (for reasons explained in 6.7.1) was also performed and the results are shown in Tab. 6.4.

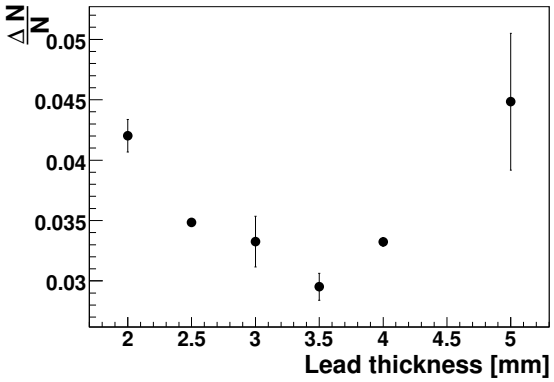

Figure 6.12: Statistical fluctuations in γ_C conversion vs. lead thickness. The error bars are larger where fewer data were collected.

6.5 Detecting Laser-Wire Compton Scattered Electrons

The Compton scattered electron (e_C^-) spectrum is shown in Fig. 6.11. The energies of these electrons are between 50 and 250 GeV. A suitable Cerenkov detector could be positioned for instance, between the first and second dipole magnets in the second set of dipoles. In this case, if 10 mm clearance from the main 250 GeV beam is allowed then the vertical dotted line in Fig. 6.13 shows the position of the innermost edge of the detector relative to the linac/BDS neutral

Location	$\bar{N}$	$\Delta N/\bar{N}$
After converter	$(31.2 \pm 0.6)\%$	0.011 ± 0.003
After converter and dipole	$(23.6 \pm 1.7)\%$	0.046 ± 0.005

Table 6.4: Bunch by bunch statistical uncertainty of photon detection. $\bar{N}$ is the number of electron positron *pairs* above the Cerenkov threshold (9 MeV) detected after conversion as a fraction of the original 1000 photons and ΔN is the corresponding bunch by bunch statistical fluctuation. Ten bunches were simulated; $\bar{N}$ average number and ΔN is the RMS.

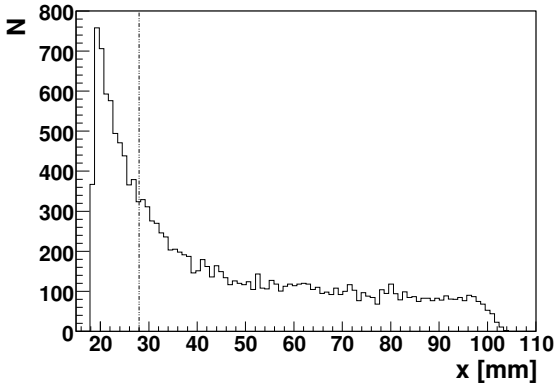

Figure 6.13: Positions with respect to the e^- beam reference trajectory of the ILC laser-wire e_C^- at proposed laser-wire electron detector for a 250 GeV e^- beam. The vertical dotted line shows the innermost edge of the detector.

beam line (i. e. the γ_C beam line). The peak of the energy spectrum cannot be sampled because of its proximity to the main beam but due to the long tail in the spectrum 68% of the electrons hit the detector. 15 bunches were simulated, assuming 1000 Compton events per bunch, to find out the statistical uncertainty in the number of particles hitting the detector. The results are shown in Tab. 6.5

6.6 Laser-Wire Background in Polarimeter Detector

The integration of the laser-wire and polarimeter within the same chicane raises the question of whether they can be operated at the same time. In order to check whether the laser-wire signal affects the polarimeter operation, laser-wire e_C^- and γ_C were simulated travelling through the entire length of the polarimeter vacuum chamber in the configuration described above. The number of electron and positron hits in the polarimeter detector due to laser-wire e_C^- and γ_C are shown in Tab. 6.6.

Clearance [mm]	$\bar{N}$	ΔN	$\Delta N/\bar{N}$
2.5 mm	948 ± 1	10 ± 3	0.011 ± 0.003
5 mm	840 ± 3	15 ± 4	0.017 ± 0.005
7.5 mm	755 ± 3	19 ± 1	0.025 ± 0.001
10 mm	684 ± 1	21 ± 6	0.030 ± 0.009
15 mm	578 ± 3	16.6 ± 0.7	0.029 ± 0.001
20 mm	495 ± 5	15 ± 2	0.030 ± 0.004
25 mm	432 ± 8	19 ± 3	0.044 ± 0.007
30 mm	380 ± 10	17.6 ± 0.7	0.046 ± 0.002

Table 6.5: Bunch by bunch statistical uncertainty of e_C^- detection. $\bar{N}$ is the mean number of e_C^- detected out of the 1000 initial Compton events and ΔN is the corresponding bunch by bunch statistical fluctuation. Clearance is the distance from the edge of the detector to the main 250 GeV beam line. The $\pm$ are the statistical uncertainties of the simulation.

$H_{e_C^-}$	H_{γ_C}	$H_{e_{C,pol}^-}$
(3.7 ± 0.6) %	(3.2 ± 0.3) %	(60 ± 0.3) %

Table 6.6: Hits from the laser-wire and polarimeter in the polarimeter detector as a fraction of Compton events for both laser-wire and polarimeter with no MPS collimator in the chicane. "Hits" are defined as electrons or positrons with energy greater than 9.25 MeV entering the detector plane. "H" means hits and the subscript denotes the origin of the hits. $e_{C,pol}^-$ means Compton scattered electrons from the polarimeter.

As the laser-wire and the polarimeter have approximately the same Compton rate, the laser-wire causes significant backgrounds both with and without the MPS collimator present; a few percent would affect the performance of the polarimeter and be deemed significant. With the MPS collimator present, the γ_C and converted particles from the laser-wire detector impact directly upon the collimator, producing electromagnetic showers which cause a high hit rate in the polarimeter detector (Tab. 6.7).

$H_{e_C^-}$	H_{γ_C}
(4.4 ± 0.3) %	(26 ± 3) %

Table 6.7: Hits from laser-wire in the polarimeter detector as a fraction of laser-wire Compton events with the MPS collimator present in the chicane. See Tab. 6.6 for definitions.

6.7 Dealing With SR Backgrounds

In [50], the background due to SR photons, γ_{SR}, in terms of energy, from the first dipole in the chicane in a laser-wire γ_C calorimeter detector is shown to be $\sim$10 times the signal. If the γ_C are counted using a Cerenkov detector, then the particles below the Cerenkov threshold (E_t) are not detected. It was shown in [50] that for this Cerenkov detector the background is at least 10 times the signal and therefore using a Cerenkov detector offers essentially no improvement in terms of background reduction (details of the relative numbers of γ_{SR} and γ_{LW} at the laser-wire detector are in Sec 6.7.2). Therefore additional steps need to be taken in order to detect the γ_C in the polarimeter chicane. Some possible solutions are now evaluated analytically and in BDSIM simulations.

6.7.1 Laser-Wire γ_C Detection

Possible ways of detecting the laser-wire Compton photons without being swamped by SR background were investigated. The following ways of increasing the signal to background ratio were considered.

1. There is a sharp edge of the distribution (Fig. 6.14) of the SR photons which coincides with the core of the laser-wire γ_C beam (Fig. 6.15) such that by carefully positioning the converter it is possible to reach an optimum position where the ratio $\frac{N_{\gamma,LW}}{N_{\gamma,SR}}$ is a maximum.

2. If there is an appropriate dipole field between a γ_C converter and the Cerenkov detector then most of the SR converted electrons and positrons, which are of a lower energy than the laser-wire conversions (Figs. 6.15, 6.18), are swept aside, and most of the laser-wire conversions go through to hit the detector, as shown in Sec. 6.7.2.

Inside the polarimeter chicane there exist dipole fields which could be used naturally to employ solution 2. The chicane's magnet layout consists of 3 sets of 3 dipoles with 30 cm of space between each of the dipoles in a set (see Fig. 6.10) and the converter and Cerenkov detector could be placed on either side of one of these fields. The best choice would be to place the converter and detector between the dipoles in the second set of dipoles in the positions shown in Fig. 6.10, so that both converter and Cerenkov counter would have large dipole fields both upstream and downstream, shielding them from stray low energy particles.

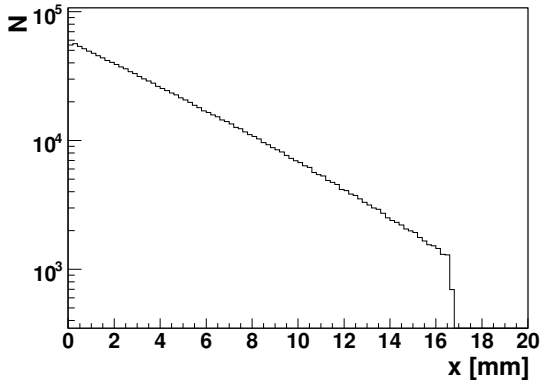

Figure 6.14: Shape of the distribution of γ_{SR} along the horizontal axis at the entrance to the second set of dipoles. $E_c = 4.1$MeV.

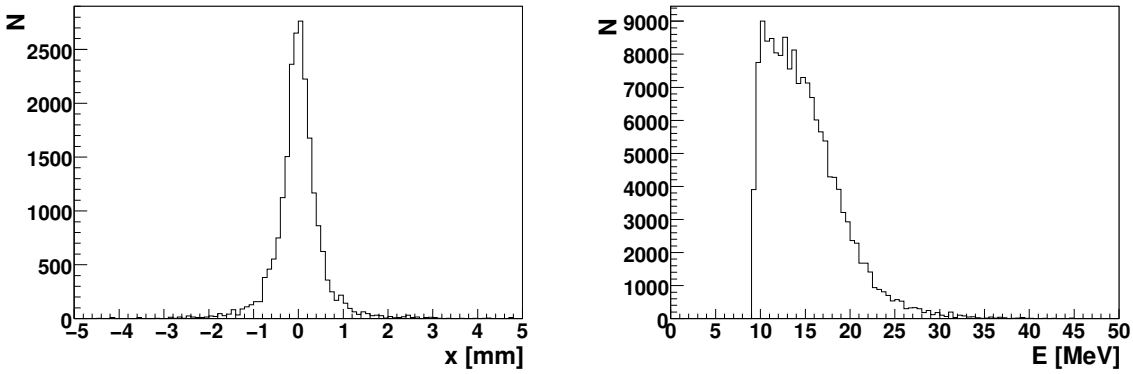

Figure 6.15: Left: shape of the distribution of laser-wire photons along the horizontal axis at the entrance to the second set of dipoles. x=0 is the neutral beam centre. Right: shape of the energy spectrum downstream of the converter of pair produced electrons and positrons from γ_{SR} from a 250 GeV e^- beam. $E_c = 4.1$MeV.

A charged particle coming from the converter will hit the Cerenkov detector if it has enough momentum to get through the dipole field without being deflected away from the detector. Only electrons or positrons which satisfy Eq. 6.1, derived from the familiar equation for the radius of curvature of an electron in a dipole field [5], will hit the detector plane, where p is the relativistic momentum of the electron or positron, l is the length of the dipole field in metres, d is the transverse size of the detector in metres and B is the magnetic field strength in Tesla, as illustrated in Fig. 6.16.

$$p > \frac{(d/4 + l^2/d)B}{3.3356} \text{ GeV/c} \tag{6.1}$$

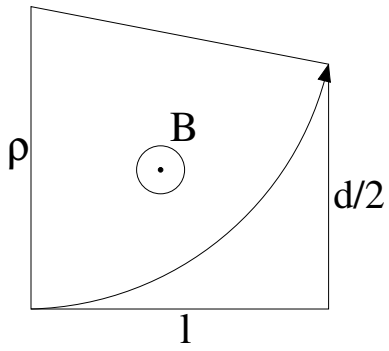

Figure 6.16: Trajectory of a negatively charged particle in a dipole field. ρ is the radius of curvature, B is the magnetic field and d is the detector transverse size.

If one of the dipoles in the second set of triplets in the polarimeter chicane is used, then $l = 2.4$ m, $B = 0.098$ T and $d/2 = 3$ cm. From Eq. 6.1, only particles with energy greater than 2.8 GeV $= 683E_c$ will be detected. This is in the extreme high energy tail. The highest tabulated result in Tab. 6.8, taken from [1], is for $k = 50$, where k is the low energy cutoff and is in units of E_c. SR photons with $k > 50$ make up only $0.6158.10^{-23}$ of the population. The direct background from the converted SR photons will therefore be negligible. However, in a more realistic model stray SR photons could hit material such as the vacuum chamber wall *after* the converter and dipole field. These are included in simulations of the proposed laser-wire detection region (Sec. 6.7.2).

for k above	photon spectrum
4.0	$0.2242 \cdot 10^{-2}$
5.0	$0.7372 \cdot 10^{-3}$
10.0	$0.3494 \cdot 10^{-5}$
15.0	$0.1915 \cdot 10^{-7}$
20.0	$0.1115 \cdot 10^{-9}$

Table 6.8: Fraction of photons above a certain photon energy. The photon energy cut is given in units (k) of the critical energy, E_c [1].

6.7.2 Simulation

In the simulation, the spectra of the pair produced electrons and positrons before and after the magnetic field show that essentially all of the particles below 4.5 GeV are removed, which is in agreement with the above calculation when you take into account the fact that the photons undergo pair production. As expected, some particles below this energy are seen. Presumably these are due to SR photons involved in pair production in the walls of the vacuum pipe and the

walls of the tunnel *after* the magnetic field.

SR Generator

A Monte Carlo generator was used to generate the SR, as detailed in [1]. In the first test, a low energy cut was put on the generated γ_{SR} at $E_{\text{lowcut}} = 18.5$ MeV, which is twice the Cerenkov threshold energy of the proposed Cerenkov detector. The SR critical energy, E_c is 4.1 MeV [50] and so $k_{\text{lowcut}} = \frac{E_{\text{low}}}{E_c} = 4.5$. $N_{\gamma,k\to x}$ is the number of SR photons with energies greater than x times the critical energy. We define ζ_x as $\frac{N_{\gamma,k\to x}}{N_\gamma}$. Fig. 2 in [1] shows that the $N_{\gamma,k\to x}$ spectrum falls exponentially between $x = 4.0$ and $x = 5.0$, and so $\zeta(4.5)$ is $\sqrt{\zeta(4.0)\zeta(5.0)}$. From Tab. 6.8, taken from [1], $\zeta(4.0) = 0.2242.10^{-2}$ and $\zeta(5.0) = 0.7372.10^{-3}$, so $\zeta(4.5) = 0.1286.10^{-2}$. The SR spectrum generated in the first set of dipoles at $k = 4.5$ is shown in Fig. 6.17. There are $1.43 \cdot 10^{10}$ γ_{SR} produced in the first dipole, so $1.84 \cdot 10^7$ of these are over twice the Cerenkov threshold, outnumbering the laser-wire γ_C by $\sim 10^2$.

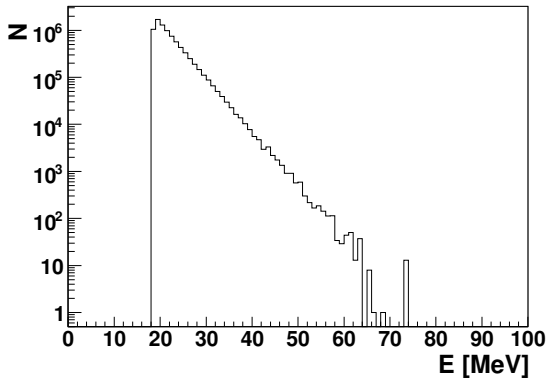

Figure 6.17: Shape of the energy spectrum of the generated SR for $k = 4.5$. k is defined in Tab. 6.8.

Positioning of the $\gamma \to e^- e^+$ Converter To Maximise the Signal to Background Ratio

The laser-wire detector was chosen to subtend $\sim \pm 5$ mm in order to capture essentially all γ_C (Fig. 6.15). The γ_{SR} and $\gamma_C$were both simulated. 5 cm before the second set of dipoles is a good location for a lead converter since the electron and photon beams are separated by 16.7 mm at this point (Fig. 6.14), where the maximum separation is 20 mm at 250 GeV. Here, the SR subtends a region in the horizontal plane from $\sim$16 mm outwards. Most of the γ_C subtend a region in the horizontal plane from 16.2 mm to 17.2 mm, clearing the γ_{SR} by 200 μm. Therefore by

positioning the lead converter carefully enough it might be possible to reduce the SR background significantly whilst keeping a large proportion of the laser-wire signal.

Employing A Dipole Field Between the Converter and the Cerenkov Detector

In the first dipole of the polarimeter chicane $E_c = 4.1$ MeV, but the γ_C energies are typically of order 10s of GeV, with a maximum energy of about 200 GeV (Fig. 6.18 shows the energies of the pair produced electrons from these γ_C), whose original spectrum before conversion is shown in Fig. 6.11. This difference can be exploited to separate the laser-wire photon signal from the SR background by using a thin converter together with one of the chicane dipoles to form effectively a high-pass filter; one of the dipoles in the second set of triplets in the polarimeter chicane can be used naturally for this purpose as described above in Sec. 6.7.1.

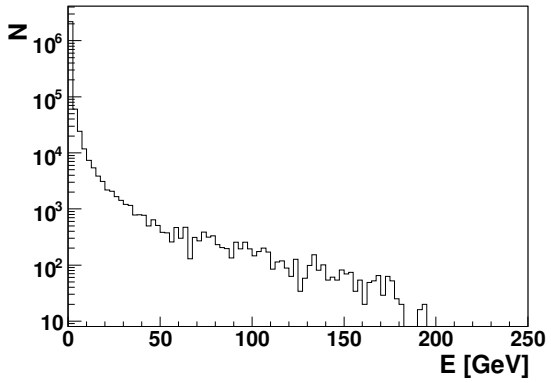

Figure 6.18: Shape of the energy spectrum downstream of the 3.5 mm converter of pair-produced electrons and positrons from γ_C from a 250 GeV e^- beam.

This configuration was simulated in BDSIM using an SR generator of the kind described in [1]. As the direct background from γ_{SR} below 2.8 GeV was expected to be negligible, only photons with energies greater than $k = 50$ were generated at first. The number of tracks seen was multiplied by the fraction of photons above $k = 50$ and normalised to the number of electrons in a bunch, assuming the ILC design value of $N_e = 2 \cdot 10^{10}$. However, more tracks were seen when the k value was lowered to 40. Finally, it was necessary to run simulations with k as low as 4.5 before the results converged.

The number of hits due to SR for $k = 20, 10, 4.5$ are shown in Tab. 6.9. The quantity of hits is constrained because there cannot be fewer than zero hits, so in calculating the 95% upper

confidence limit Bayesian statistics was used [51]. The SR spectrum is such that the number of particles increases exponentially with decreasing energy. We cannot simulate the whole spectrum so we choose a low energy cutoff for SR photon production which is proportional to k. The number of photons above $k = 20$ is small, so when we set the cutoff at $k = 20$ we see a small number of hits per bunch. At $k = 10$, more SR photons are produced, so the number of hits is greater. At $k = 4.5$, the number of SR photons produced is greater still, but they are at lower energies the electrons and positrons produced in the converter are swept aside by the dipole before they can hit the Cerenkov detector, and so the number of hits is the same, within the error.

The results between consecutive k values agreed within the errors at $k = 10$ and $k = 4.5$ so γ_{SR} with energies down to $10E_c$ contributed to the backgrounds, presumably due to interactions in the vacuum chamber walls and magnets. Therefore the number of SR hits with the Cerenkov detector placed after the dipole and the converter placed before the dipole is < 12 per bunch (from the 11.7 in Tab. 6.9, which is negligible.

Table 6.9: Simulation results for hits due to SR in γ_C detector. H_d is the number of detector hits due to SR with the Cerenkov detector placed just after the next dipole, where "hits" is defined as the number of electrons and positrons above the Cerenkov threshold energy (9.25 MeV) hitting the detector plane. σ_{H_d} is the statistical uncertainty in the simulation.

k	H_d/bunch	$\sigma_{H_d/\mathrm{bunch}}$	95% upper c.l.
20	$2.92 \cdot 10^{-5}$	$1.16 \cdot 10^{-5}$	$4.834 \cdot 10^{-5}$
10	6.35	3.17	11.7
4.5	3.23	3.23	8.82

The number of detector hits with the Cerenkov detector placed *before* the dipole and directly after the converter is $(5.2 \pm 0.3) \cdot 10^4$, or about 9 times the Compton signal. This is roughly in agreement with the estimates made in [50]. However, the dipole provides a reduction factor of better than $2.5 \cdot 10^{-4}$ to the SR and only 0.77 to the laser-wire signal, increasing the signal to background ratio to better than 370.

6.8 Linac-related Backgrounds

The ILC reference design [26] locates the laser-wire on a direct line of sight to the main linac, which means that backgrounds in this region are likely to be significant. If we assume a square converter of transverse size L, then any photon with energy greater than about 3 GeV impinging on that area would be a source of background for the γ_C detection. Any off-energy electrons

are likely to be removed from the linac by over-focusing in the linac quadrupoles and so are not considered further here; however photons from the resulting electromagnetic showers may be in issue. SR from the Linac quadrupole fields has $\sim 10^2$ times lower critical energy than that from the chicane dipoles and will be subject to the same enormous reduction factors of the converter/dipole/Cerenkov system discussed above; so this potential source of background is not considered further here. This leaves beam-gas bremsstrahlung as the most likely cause of backgrounds from the linac.

The distance D of the linac relevant for producing photon background is effectively reduced by the geometric factor of the earth's curvature R_E to $D \simeq \sqrt{R_E L}$. Assuming $L = 1$ cm, this gives $D \simeq 250$ m. Being conservative and to allow for a final straight section for the linac, we now estimate the background from beam gas bremsstrahlung for $D = 300$ m. The cross-section for bremsstrahlung off N_2 or CO gas is estimated [15] to be $\sigma_B \simeq 5.51$ barns when the scattering cut-off is set at 1% of the beam energy, or in our case 2.5 GeV, which is also (conservatively) the relevant cutoff for our detection system. Assuming pressure $P = 10$ nTorr, temperature $T = 2$ K, and $N_e = 2 \cdot 10^{10}$ electrons per bunch, the number of background events per bunch is $DPN_e\sigma_B/k_BT$ where k_B is Boltzmann's constant, which gives about 160 bremsstrahlung photons per bunch. This is a few % of a typical peak laser-wire signal for a vertical laser-wire scan (the signal is $\sim 10000\ \gamma_C$ for $\sigma_m \simeq 2\ \mu$m) and about 10% for a horizontal scan (with $\sigma_m \simeq 20\ \mu$m).

6.9 Conclusions

The laser-wire detector region has been simulated in BDSIM and detection efficiencies evaluated, including effects of material interactions and secondaries. The background from the laser-wire in the polarimeter detector, both with and without the MPS collimator present in the chicane and the SR background in the laser-wire detector has been estimated using BDSIM simulations.

A laser with wavelength 532 nm was simulated at the final laser-wire location in the ILC beam delivery system in the manner described in [15]. For the 250 GeV ILC electron and the 532 nm laser-wire photons, the scattering angles in the electron rest frame are not well approximated using this Monte Carlo and the simulation could be made more accurate by using the full Compton differential cross section (see Sec. 2.3.4).

The simulations show that the SR background in the laser-wire can be dealt with by locating

the conversion material and Cerenkov detector either side of one of the existing dipole magnets in the chicane, effectively using it as a high pass filter. However, a simple calculation shows that linac-related backgrounds will still adversely affect the performance of the laser-wire, even with this filter. There is also the possibility that additional backgrounds may contribute.

e_C^- detection is possible, but if the polarimeter chicane is to operate with a fixed field then this detector will have to be movable within the vacuum chamber for operation at different e^- beam energies. This could prove technically challenging.

The background from the laser-wire e_C^- and γ_C in the polarimeter detector has been shown to be considerable, both with and without the MPS collimator present in the chicane.

In conclusion, it would be preferable to locate the laser-wire after a large bend downstream of the linac in order to avoid linac related backgrounds, in a separate chicane from the polarimeter.

Chapter 7

Conclusions

7.1 Future Work

The laser-wire will be installed at ATF2 [2, 3]. The emittance is expected to become smaller and more stable than it was at the end of running at ATF. Careful measurement and control of the emittance needs to be carried out at ATF2 [2, 3] to verify the capability of the laser-wire to measure 1 μm electron beams.

The new electron beam optics will need to be carefully simulated and checked experimentally.

The backgrounds due to the SR and bremsstrahlung from the halo should be checked with these optics, using the halo measurements carried out in Chap. 5 as an input to the simulation.

Further laser beam measurements should be carried out, especially the effect of input beam size on lens M^2, careful input beam size measurements and laser propagation measurements and modelling.

The analysis of collision data could be improved by carrying out full overlap integrals. This requires measurements on the horizontal electron beam size as well as the vertical.

Once the system is up and running at ATF2 [2, 3], fast electro optical scanning could be tested.

The simulation of backgrounds in the ILC beam delivery system could be extended to include backgrounds coming out of the linac, and the Compton scattering Monte Carlo improved.

7.2 Summary and Main Conclusions

Measurements were made to account for contributions to σ_c, the size of the convolution between the electron beam and laser beam, as measured during an electron beam measurement using a laser-wire scan.

Contributions to the electron beam size are from the emittance, and from the dispersion.

Factors contributing to the laser beam size include the input beam size on the lens, and the M^2 laser quality factor. Simulations and measurements indicate that the lens introduces spherical aberrations above a certain input beam size (Sec. 4.3.1) and these affect the quality of the laser; a input laser beam with $M^2_{\text{in}} = 1$ may have a greater M^2 downstream of the lens. We define $\sqrt{(M^2_{\text{lens}})^2 + (M^2_{\text{in}})^2} = M^2_{\text{final}}$. The dominating error in the estimation of the final focus laser beam size, σ_{lw}, come from the error in the measurement of the input beam size. Simulations and measurements predict that $\sigma_{\text{lw}} < 1$ μm could be achieved by reducing the input beam size (Fig. 4.4).

The maximum contribution to beam size from a simple astigmatism is small (< 0.1 μm). The full effects of general astigmatism will be of a similar order, given the measured size of the imaginary part of the rotation angle. Therefore, the contribution to beam size from general astigmatism is neglected.

The smallest convoluted beam size, σ_c, was measured after skew quadrupole tuning, was measured as 3.65 ± 0.09 μm.

Using various measurements and models the laser beam size was estimated to be $\sigma_{\text{lw}} = 2.1 \pm 0.2$ μm. Therefore the minimum measured electron beam size was 2.91 ± 0.15 μm (Tab. 4.14).

After measuring the dispersion a contribution to the vertical electron beam size due to vertical dispersion was found to be 3.03 ± 0.66 μm.

Using all the above information the electron beam emittance in the ATF extraction line was measured as 248^{+92}_{-174} pm using the laser-wire. The design value of ε_y for ATF is 12 pm in the damping ring, and this increases in the extraction line to ~ 3 times this value, but a value of 207 pm was measured on the previous month using a wire scanner, confirming our laser-wire measurement.

These measurements should be done with an input laser beam size of $W_{\text{in}} = 6$ mm (Fig. 4.5), which will allow us to achieve an even smaller spot size. High power fibre lasers are being

developed [42] which should be able to produce high power, high quality beams. The dispersion should be removed before performing attempting an emittance measurement.

To verify that the remaining contribution to σ_c is due to a large emittance beam may require an independent emittance measurement simultaneously with the laser-wire emittance measurement, along with dispersion correction and measurements, during a single data taking shift. The emittance at ATF2 [2, 3] is expected to be smaller and more stable.

A source of background at ATF and at future linear colliders is beam halo. Measurements were made of the halo in the ATF extraction line and compared to a theory of halo production by beam-gas scattering in the tails of the distribution. Comparing the fit values, Tab. 5.4, to the calculated values, Tab. 5.2, we see that N_d is 7.5 times larger in the fit and σ_0' is about 5 times smaller in the fit, assuming 10 pm damping ring emittance. These do not seem like reasonable values. Also, the fit of Eq. 5.2 to the data is not very good. The calculated values are estimates. For a more precise comparison with the theory [44], more data is required, such as emittance measurements, Twiss parameter measurements, gas pressure measurements and gas composition in the damping ring. How the distribution is modified via the kicker between the damping ring and the extraction line also needs to be better understood.

The laser-wire detector region has been simulated in BDSIM and detection efficiencies evaluated, including effects of material interactions and secondaries. The background from the laser-wire in the polarimeter detector, both with and without the MPS collimator present in the chicane and the SR background in the laser-wire detector has been estimated using BDSIM simulations.

A laser with wavelength 532 nm was simulated at the final laser-wire location in the ILC beam delivery system in the manner described in [15]. For the 250 GeV ILC electron and the 532 nm laser-wire photons, the scattering angles in the electron rest frame are not well approximated using this Monte Carlo and the simulation could be made more accurate by using the full Compton differential cross section (see Sec. 2.3.4).

The simulations show that the SR background in the laser-wire can be dealt with by locating the conversion material and Cerenkov detector either side of one of the existing dipole magnets in the chicane, effectively using it as a high pass filter. However, a simple calculation shows that linac-related backgrounds will still adversely affect the performance of the laser-wire, even with this filter. There is also the possibility that additional backgrounds may contribute.

e_C^- detection is possible, but if the polarimeter chicane is to operate with a fixed field then this detector will have to be movable within the vacuum chamber for operation at different e^- beam energies. This could prove technically challenging.

The background from the laser-wire e_C^- and γ_C in the polarimeter detector has been shown to be considerable, both with and without the MPS collimator present in the chicane.

In conclusion, it would be preferable to locate the laser-wire after a large bend downstream of the linac in order to avoid linac related backgrounds, in a separate chicane from the polarimeter.

An outline of a future programme of work has been identified.

Bibliography

[1] H. Burkhardt, Monte Carlo generation of the energy spectrum of synchrotron radiationEUROTEV-REPORT-2007-018.

[2] B. I. Grishanov, et al., ATF2 proposal, SLAC-R-771.

[3] B. I. Grishanov, et al., ATF2 proposal. Vol. 2, arXiv:physics/0606194.

[4] H. Wiedemann, Particle Accelerator Physics, 2nd Edition, Vol. 1, Springer, 2003.

[5] E. Wilson, Introduction to Accelerator Physics, Oxford University Press, 2001.

[6] D. A. Edwards, An Introduction to the Physics of High Energy Accelerators, Wiley VCH, 1993.

[7] A. W. Chao, M. Tigner, Handbook of Accelerator Physics and Engineering, World Scientific, 2006.

[8] I. Agapov, G. A. Blair, M. Woodley, Beam emittance measurement with laser wire scanners in the International Linear Collider beam delivery system, Phys. Rev. ST Accel. Beams 10 (2007) 112801. doi:10.1103/PhysRevSTAB.10.112801.

[9] F. C. Iselin, The MAD programPresented at 12th Int. Conf. on High Energy Accelerators, Batavia, IL, Aug 11-16, 1983.

[10] F. C. Iselin, The MAD program (methodical accelerator design): reference manualCERN-LEP-TH/85-15.

[11] H. Grote, F. C. Iselin, Recent developments in MAD: version 8Presented at Int. Conf. on Accelerator and Large Experimental Physics Control Systems, Vancouver, Canada, Oct 30- Nov 3, 1989. doi:10.1016/0168-9002(90)91483-R.

[12] A. H. Compton, A Quantum Theory of the Scattering of X-rays by Light Elements, Phys. Rev. 21 (1923) 483–502. doi:10.1103/PhysRev.21.483.

[13] P. Tenenbaum, T. Shintake, Measurement of small electron-beam spots, Ann. Rev. Nucl. Part. Sci. 49 (1999) 125–162. doi:10.1146/annurev.nucl.49.1.125.

[14] A. E. Siegman, Defining, measuring, and optimizing laser beam quality, in: Proc. SPIE, 1993, 1868, 2.

[15] H. Burkhardt, Monte Carlo Simulation of Scattering of Beam Particles and Thermal Photons SL/Note 93-73 (OP).

[16] D. E. Knuth, The Art of Computer Programming, Vol. II, Addison-Wesley Publishing.

[17] M. Castellano, A new non-intercepting beam size diagnostics using diffraction radiation from a slit, Nucl. Instrum. Meth. A394 (1997) 275–280. doi:10.1016/S0168-9002(97)00570-6.

[18] P. Karataev, et al., Beam-size measurement with optical diffraction radiation at KEK accelerator test facility, Phys. Rev. Lett. 93 (2004) 244802. doi:10.1103/PhysRevLett.93.244802.

[19] P. Karataev, et al., Observation of optical diffraction radiation from a slit target at KEK accelerator test facility, Nucl. Instrum. Meth. B227 (2005) 158–169. doi:10.1016/j.nimb.2004.03.012.

[20] H. Wiedemann, Particle Accelerator Physics, 2nd Edition, Vol. 2, Springer, 2003.

[21] R. W. Assmann, LEP operation and performance with electron positron collisions at 209-GeV, in: 11th Workshop on LEP Performance, Chamonix, France, 2001.

[22] K. Kubo, et al., Extremely low vertical-emittance beam in the Accelerator Test Facility at KEK, Phys. Rev. Lett. 88 (2002) 194801. doi:10.1103/PhysRevLett.88.194801.

[23] Y. Honda, et al., Achievement of ultra-low emittance beam in the ATF damping ring, Phys. Rev. Lett. 92 (2004) 054802. doi:10.1103/PhysRevLett.92.054802.

[24] P. Karataev, private communication.

[25] T. Okugi, Hardware check of ATF extraction line, Minutes of ATF2 meeting (August 2007).

[26] N. Phinney, N. Toge, N. Walker (Eds.), International Linear Collider Reference Design Report 2007, Vol. 3 - Accelerator, ILC global design effort and world wide study, 2007.

[27] A. Aryshev, et al., Micron Size Laser-wire System at the ATF Extraction Line, EPAC'08, 11th European Particle Accelerator Conference, 23- 27 June 2008, Genoa, Italy.

[28] Y. Honda, et al., Upgraded laser wire beam profile monitor, Nucl. Instrum. Meth. A538 (2005) 100–115. doi:10.1016/j.nima.2004.08.122.

[29] A. Bosco, et al., A two-dimensional laser-wire scanner for electron accelerators, Nucl. Instrum. Meth. A592 (2008) 162–170. doi:10.1016/j.nmia.2008.04.012.

[30] S. T. Boogert, private communication.

[31] G. A. Blair, et al., A study of emittance measurement at the ILCPrepared for European Particle Accelerator Conference (EPAC 06), Edinburgh, Scotland, 26-30 Jun 2006.

[32] S. T. Boogert, L. C. Deacon, et al., A laser wire system at the ATF extraction line, in: EPAC, Edinburgh, Scotland, 2006, pp. 738–740, mOPLS080.

[33] L. C. Deacon, et al., ATF extraction line laser wire system, in: PAC, Albuquerque, New Mexico, USA, 2007, pp. 2636–2638, THOAC01.

[34] P. A. Franken, et al., Generation of optical harmonics, Phys. Rev. Lett. 7 (4) (1961) 118–119. doi:10.1103/PhysRevLett.7.118.

[35] W. M. Yao, et al., Review of particle physics, J. Phys. G 33 (1).

[36] T. M. Actuatuator, `http://www.thorlabs.com/thorProduct.cfm?partNumber=Z612`.

[37] I. Agapov, G. A. Blair, J. Carter, O. Dadoun, BDSIM: Beamline simulation toolkit based on GEANT4Prepared for European Particle Accelerator Conference (EPAC 06), Edinburgh, Scotland, 26-30 Jun 2006.

[38] M. Newman, private communication.

[39] D. Inc., `http://www.dataray.com`.

[40] J. A. Arnaud, H. Kogelnik, Gaussian light beams with general astigmatism, Applied Optics 8 (8) (1969) 1687–1693.

[41] P. Karataev, private communication.

[42] L. Corner, et al., Development of a High Power Fibre Laser for Laser Based Electron Beam DiagnosticsEPAC'08, 11th European Particle Accelerator Conference, 23- 27 June 2008, Genoa, Italy.

[43] T. Suehara, H. Yoda, M. Oroku, T. Yamanaka, S. Komamiya, T. Sanuki, T. Tauchi, Y. Honda, T. Kume, R&d status of atf2 ip beam size monitor (shintake monitor), ECONF C 0705302 (2007) 2007.
URL http://www.citebase.org/abstract?id=oai:arXiv.org:0709.%1333

[44] K. Hirata, K. Yokoya, Nongaussian distribution of electron beams due to incoherent stochastic processes, Part. Accel. 39 (1992) 147–158.

[45] F. Hinode, et al., ATF accelerator test facility sesign and study report, Tech. Rep. 4, ATF, KEK (1995).

[46] S. Agostinelli, et al., G4–a simulation toolkit, Nucl. Inst. Meth. A 506 (2003) 250 – 303. doi:10.1016/S0168-9002(03)01368-8.

[47] M. Woods, ILC MAD files, http://www.slac.stanford.edu/~mdw/ILC/2006e/ (2006).

[48] P. Schuler, http://ilcagenda.linearcollider.org/conferenceDisplay.py?confId=2399, talk at BDS Meeting (November 2007).

[49] E. Doyle, et al., New post-linac collimation system for the next linear colliderSLAC-TN-03-069.

[50] M. Woods, K. Moffeit, Synchrotron backgrounds for laserwire detector in upstream polarimeter chicanePBI TN-2008-2, ILC-NOTE-2008-041.

[51] R. J. Barlow, Statistics: A Guide to the Use of Statistical Methods in the Physical Sciences, Wiley, 1989.